

Intensity-dependent effects in the Accelerator Test Facility 2 and extrapolation to future electron-positron linear colliders



Pierre Korysko
Jesus College
University of Oxford

A thesis submitted for the degree of
Doctor of Philosophy

Trinity 2020

This thesis is dedicated to my parents.

Acknowledgements

Foremost, I would like to thank my Oxford supervisor Philip Burrows for giving me the opportunity to work on such an interesting project and for his guidance, his time, his help and his advice during this journey. I would also like to thank my CERN supervisor Andrea Latina for his time, advice and for many helpful and detailed discussions we had around coffees in his office, in the CERN cafeteria or at conferences and workshops. I would like to thank Angeles Faus-Golfe for her support and for all these insightful comments and suggestions about my work at ATF2.

I had the chance and the opportunity to work at ATF2, KEK, in Japan, and for this reason, I would like to thank the ATF2 and KEK staff for their hospitality. In particular, I would like to thank Terunuma-san for his dedication, Okugi-san and Kubo-san for their help on the intensity-dependent effects simulations and measurements and Tauchi-san for helping to measure the bunch length in ATF2. I would also like to thank people from CERN who helped me understanding the challenges of ATF2, in particular Renjun Yang and Rogelio Tomas. Last but not least, I would like to thank the MSCA-RISE E-JADE project, funded by the European Commission under grant number 645479, for sponsoring the experiments in Japan.

It was a pleasure to share many experiences with my friends and colleagues from the University of Oxford Chetan Gohil, Jan Paszkiewicz, Douglas Bett. During my stay at CERN, I also shared some great experiences with outstanding colleagues and friends, in particular Malek Haj Tahar, Fabien Plassard and Jim Ogren.

Above all, I would like to thank my parents and siblings for always believing in me and supporting me with an unlimited enthusiasm at every step of this journey. Finally, I would like to thank this special person who supported me, inspired me and motivated me in particular during the thesis writing.

Abstract

The high energy physics community considers electron-positron linear colliders in order to complement the results obtained at the Large Hadron Collider. In order to achieve the design luminosity above $10^{34} \text{ cm}^{-2}\text{s}^{-1}$, these linear colliders require a nanometer beam size at the Interaction Point (IP). The electron and positron beams are transported inside the Beam Delivery Systems (BDS) from the linear accelerators (LINACS) to the IP. The beam is focused by two strong quadrupoles in the Final Focus System (FFS) where chromatic effects and aberrations are corrected thanks to a local chromaticity correction scheme. Two projects are being studied now, the International Linear Collider (ILC) and the Compact Linear Collider (CLIC). Their FFS and the local chromaticity correction are being tested at the Accelerator Test Facility 2 (ATF2) at KEK in Japan. This test facility has been studying this matter for more than 20 years, achieving two of its main goals, obtaining a stable beam size around 37 nm at the IP and an orbit stabilisation with a nanometer precision at the IP. However, these goals were achieved at 10% of the nominal beam intensity. Indeed, when increasing the beam intensity, the beam becomes more unstable and its size grows. This is mainly due to wakefields in the ATF2 extraction line. Ultra-relativistic electrons going through the beam pipe interact with the surrounding structure and create an electromagnetic field, the wakefield. This field interacts with electrons inside the same bunch (short-range wakefield) but also with electrons in the following bunches (long-range wakefield). In ATF2, one considers that bellows, flanges and cavity BPMs are the main sources of wakefield. This effect results in increasing significantly the beam size at the IP. This thesis will show the impact of these intensity-dependent effects inside ATF2 and how to mitigate them. It will also show the impact of the same intensity-dependent effects in future electron-positron linear colliders, the ILC and CLIC.

Contents

1	Introduction	1
1.1	Circular and linear accelerators	2
1.2	Circular and linear colliders	3
1.3	Linear electron-positron colliders	4
1.3.1	The International Linear Collider (ILC)	4
1.3.2	The Compact Linear Collider (CLIC)	5
1.4	Introduction to beam dynamics	8
2	The Accelerator Test Facility (ATF2)	11
2.1	ATF2 setup and goals	11
2.1.1	The ATF2 beamline	11
2.1.2	Goals of ATF2	14
2.1.3	The final focus system and local chromaticity correction	14
2.1.4	ATF2 phase advance	15
2.2	ATF2 beamline diagnostics	16
2.2.1	The IP Beam Size Monitor (IP-BSM)	16
2.2.2	Beam Position Monitor (BPM) system	17
2.2.2.1	Stripline BPMs	17
2.2.2.2	Cavity BPMs (C-BPMs)	19
2.2.3	Upstream FONT BPMs	20
2.2.4	FONT IP-BPMs	20
3	Intensity dependent effects in ATF2: simulations	22
3.1	Introduction to wakefields	22
3.1.1	Two-particle model	24
3.1.2	Effects of wakefields on the beam	25
3.1.2.1	Single-bunch beam breakup	25
3.1.2.2	Orbit deflection and beam size at the IP	25

3.2	Simulations of corrections and intensity-dependent effects	26
3.2.1	Wakefield sources in ATF2	26
3.2.1.1	Cavity BPMs (C-BPMs)	26
3.2.1.2	Bellows	28
3.2.1.3	Flanges	30
3.2.1.4	Summary	31
3.2.2	Orbit, dispersion and wakefield corrections	32
3.2.2.1	One-to-one correction	32
3.2.2.2	Dispersion Free Steering (DFS)	33
3.2.2.3	Wakefield Free Steering (WFS)	33
3.2.2.4	IP tuning knobs	34
3.2.2.5	Impact of One-to-one, Dispersion Free Steering, Wake- field Free Steering corrections and IP tuning knobs .	35
3.3	Impact of static errors: misalignments, spurious multipoles, rolls . . .	36
3.4	Impact of dynamic errors: incoming position and angle jitters	38
3.5	Wakefield knobs	45
3.6	Bunch length impact on the beam intensity.	49
3.7	Conclusion	51
4	Intensity-dependent effects in ATF2, measurements	52
4.1	Impact of the intensity on the bunch length	52
4.2	Machine and beam instabilities	55
4.2.1	Slow Beam orbit drift	55
4.2.2	Beam intensity drift	56
4.2.3	Dispersion drift	57
4.3	Measurement of the incoming position and angle jitters	57
4.4	Impact of the intensity on the BPM resolution	59
4.5	Impact of the intensity on the beam orbit	62
4.5.1	Correlation between beam orbit and beam intensity using the Singular Value Decomposition (SVD)	62
4.6	Impact of the beam intensity on the beam size	68
4.7	Mitigation strategies	69
4.7.1	Dispersion Free Steering	69
4.7.2	Wakefield Free Steering	71
4.7.3	Impact of DFS and WFS on the vertical IP beam size	71
4.7.4	Wakefield knobs	72

4.8	Comparison between simulations and measurements	74
5	Intensity dependent effects in the ILC BDS	77
5.1	ILC BDS 250 GeV	77
5.1.1	Beam and machine parameters	77
5.1.2	Single-bunch simulations	79
5.1.2.1	Efficiency of Beam-Based Alignment corrections . . .	79
5.1.2.2	Impact of static errors	81
5.1.3	Multi-bunch simulations	82
5.1.3.1	Long range wakefield	82
5.1.3.2	Impact of long-range wakefields for a train with a constant incoming offset	84
5.1.3.3	Impact of long-range wakefields for a train with random incoming offset	87
5.1.3.4	Impact of long-range wakefields on the luminosity . .	88
5.2	ILC BDS 500 GeV	90
5.2.1	Beam and machine parameters	90
5.2.2	Single-bunch simulations	92
5.2.2.1	Efficiency of Beam-Based Alignment corrections . . .	92
5.2.2.2	Impact of static errors	93
5.2.3	Multi-bunch simulations	94
5.2.3.1	Impact of long-range wakefields for a train with a constant incoming offset	94
5.2.3.2	Impact of long-range wakefields for a train with random incoming offset	98
5.2.3.3	Impact of long-range wakefields on the luminosity . .	98
6	Intensity-dependent effects in the CLIC BDS	101
6.1	CLIC 380 GeV BDS	101
6.1.1	Single-bunch simulations	102
6.1.1.1	Efficiency of base based alignment corrections	102
6.1.1.2	Impact of static errors	105
6.1.2	Multi-bunch simulations	107
6.1.2.1	Impact of long-range wakefields for a train with a constant incoming offset	107
6.1.2.2	Impact of long-range wakefields for a train with random incoming offset	111

6.1.2.3	Impact of long-range wakefields on the luminosity . .	111
Conclusions		114
A	Wakefield sources in ATF2	117
B	Wakefield sources in the ILC	119
C	Wakefield sources in CLIC	120
Bibliography		121

List of Figures

1.1	Feynman diagrams for production of Higgs bosons via Higgs-strahlung (left) and WW fusion (right).	4
1.2	ILC 500 GeV layout with dimensions (not to scale) [1]	6
1.3	CLIC 380 GeV layout with dimensions (not to scale) [2]	7
1.4	Schematics of the reference particle trajectory, the transverse and longitudinal coordinate system.	8
1.5	Schematics of the ellipse with selected parameters.	10
1.6	Evolution of the shape of the ellipse when going through the classical FODO lattice. F in this case means focusing in the vertical plane. . .	10
2.1	ATF2 Twiss parameters.	12
2.2	The layout of ATF2 [3]	13
2.3	The ATF2 vertical IP beam size measurement history.	14
2.4	Optical layout of the final focus system based on local chromaticity correction.	15
2.5	The phase advance between the IP and positions upstream in the beamline.	15
2.6	Schematic of the ATF2 IP Beam Size Monitor.	17
2.7	Dynamic ranges of the ATF2 IPBSM [4]	17
2.8	Picture of an ATF2 stripline (top) and schematic of a stripline BPM (bottom).	18
2.9	Picture of an ATF2 C-BPM (top) and schematic of a C-BPM (bottom).	19
2.10	Schematic of the ATF2 beamline showing the positions of the upstream FONT BPMs.	20
2.11	Schematic of the ATF2 beamline showing the positions of the IP-BPMs.	21
3.1	Scheme of the two-particle model.	24
3.2	Resonant buildup of the displacement of the tail relative to the head of the bunch.	25

3.3	Positions of Cavity BPMS in ATF2.	27
3.4	The geometry of the ATF2 C-band dipole cavity inputted in GdfidL.	27
3.5	Transverse wakepotential of the ATF2 cavity BPM in V/pC/mm calculated with GdfidL for a Gaussian bunch of 7 mm RMS length and a 1 pC charge with a vertical offset of 1 mm and the Gaussian profile of the bunch (in red). For reference, the distribution of the electrons in one bunch is shown (in blue).	28
3.6	Positions of unmasked bellows in ATF2.	28
3.7	The geometry of the ATF2 bellows, inputted in GdfidL.	29
3.8	Transverse wakepotential of the ATF2 bellows in V/pC/mm calculated with GdfidL for a Gaussian bunch of 7 mm RMS length and a 1 pC charge with a vertical offset of 1 mm and the Gaussian profile of the bunch (in red). For reference, the distribution of the electrons in one bunch is shown (in blue).	29
3.9	Positions of flanges in ATF2.	30
3.10	The geometry of the ATF2 flange, inputted in GdfidL.	30
3.11	Transverse wakepotential of the ATF2 flange in V/pC/mm calculated with GdfidL for a Gaussian bunch of 7 mm and a 1 pC charge with a vertical offset of 1 mm and the Gaussian profile of the bunch (in red). For reference, the distribution of the electrons in one bunch is shown (in blue).	31
3.12	Schematic of the One-to-one correction. The beam orbit (in red) is deflected by correctors (triangles) in order to pass through the center of the BPM, which is inside a quadrupole in this case.	33
3.13	Schematic of the Dispersion Free Steering correction.	33
3.14	Schematic of the Wakefields Free Steering corrections.	34
3.15	Average vertical beam size at the IP (σ_y^*) vs. correction step: One-to-one, DFS, WFS corrections and IP tuning knobs. The red dashed line show the vertical beam size at the IP for a perfect machine, 37 nm.	36
3.16	Effect of the misalignments on the vertical beam size at the IP (σ_y^*) vs. the beam intensity with wakefields calculated with PLACET.	37
3.17	Effect of quadrupoles and sextupoles strength error of 10^{-4} RMS at $1.0 \times 10^{10} e^-$ on the vertical IP beam size (σ_y^*), in presence of wakefields calculated with PLACET.	38

3.18	Effect of 200 μ rad RMS rolls of BPMs, quadrupoles and sextupoles on the vertical IP beam size (σ_y^*) vs. the beam intensity, in presence of wakefields calculated with PLACET.	38
3.19	(Top) Effect of an incoming $0.1\sigma_{y'}$ beam angle jitter on the vertical beam size at the IP (σ_y^*) vs. the beam intensity; (Bottom) distributions of the vertical beam size at the IP (σ_y^*) for low and high beam intensities, calculated with PLACET in the presence of wakefields. . .	40
3.20	(Top) Effect of an incoming $0.1\sigma_y$ beam position jitter on the vertical beam size at the IP (σ_y^*) vs. the beam intensity; (Bottom) distributions of the vertical beam size at the IP (σ_y^*) for low and high beam intensities, calculated with PLACET in the presence of wakefields. . .	41
3.21	Effect of incoming 0.1, 0.3 and 0.5 σ_y beam position jitter on the vertical beam size at the IP (σ_y^*) vs. the beam intensity, calculated with PLACET in the presence of wakefields.	42
3.22	Effect of incoming 0.1, 0.3 and 0.5 $\sigma_{y'}$ beam angle jitter on the vertical beam size at the IP (σ_y^*) vs. the beam intensity, calculated with PLACET in the presence of wakefields.	42
3.23	Effect of both incoming 0.1, 0.3, 0.5 and 1.0 σ_y beam position and 0.1, 0.3, 0.5 and 1.0 $\sigma_{y'}$ beam angle jitters on the vertical beam size at the IP (σ_y^*) vs. the beam intensity, calculated with PLACET in the presence of wakefields.	43
3.24	Effect of incoming horizontal position and angle jitters of respectively $0.3\sigma_x$ and $0.3\sigma_{x'}$ and incoming vertical position and angle jitters of respectively $0.3\sigma_y$ and $0.3\sigma_{y'}$ on the vertical beam size at the IP (σ_y^*) vs. the beam intensity, calculated with PLACET in the presence of wakefields.	43
3.25	Schematic of the ATF2 wakefield knobs system.	47
3.26	Vertical beam size at the IP σ_y^* vs. the position of the bellows, for one machine, calculated with PLACET in the presence of wakefields. . . .	47
3.27	Vertical beam size at the IP σ_y^* vs. the position of the bellows, for one machine, calculated with PLACET in the presence of wakefields. . . .	47
3.28	Contour plot of the simulation of the impact of the position of the C-BPMs and the bellows on the vertical beam size at the IP σ_y^* , for one machine, calculated with PLACET in the presence of wakefields.	48

3.29	Vertical beam size at the IP σ_y^* vs. the beam intensity, for 100 machines with ATF2 wakefield knobs, calculated with PLACET in the presence of wakefields.	48
3.30	Histogram of the vertical beam size at the IP with and without wakefield knobs, calculated with PLACET in the presence of wakefields.	49
3.31	Simulations of the impact of the ATF2 bunch length (σ_z) on the vertical IP beam size (σ_y^*) vs. the beam intensity, calculated with PLACET in the presence of wakefields.	50
3.32	Difference between the vertical IP beam size (σ_y^*) considering the bunch length (σ_z) is correlated and the vertical IP beam size (σ_y^*) considering the bunch length (σ_z) is not correlated with the beam intensity, calculated with PLACET in the presence of wakefields.	50
4.1	Schematic of the bunch length measurement setup (top), picture of the bunch length measurement system (bottom).	53
4.2	Screenshot of the software used for the ATF2 bunch length measurement. The gain, shutter time and area parameters are shown for the measurement. The longitudinal profile of consecutive bunches is shown at the bottom of the figure. The bunch length, sigma is in ps.	54
4.3	Bunch length measurement vs. beam intensity measured on two separate days.	54
4.4	Vertical orbit at 2 selected BPMs: QD10AFF and QF9AFF. 50000 pulses travel in ATF2 in 4h27.	55
4.5	ATF2 beam intensity drift, measured by the Integrated Current Transformer located near the IP.	56
4.6	ATF2 beam intensity (left-hand side), measured by the Integrated Current Transformer located near the IP and the air temperature in the damping ring (right-hand side).	56
4.7	Vertical dispersion (η_y) vs s (m) measured at four different times.	57
4.8	Vertical position beam jitters at upstream BPMs P1, P2 and P3 vs. beam intensity.	58
4.9	Vertical position beam position at upstream stripline BPM MQF3X.	59
4.10	Vertical resolution vs. beam intensity for BPM MQD4AFF, a cavity BPM.	61
4.11	BPM vertical resolutions along the beamline.	61
4.12	Beam intensity vs. pulse number, used for the Singular Value Decomposition studies.	63

4.13	Amplitude of the singular values S_n vs. singular value number.	64
4.14	Amplitude of the second column of the spatial matrix V and measured vertical dispersion vs. s	65
4.15	Last row of the spatial matrix V.	65
4.16	Amplitude of the sixth column of the spatial matrix V, representing correlation amplitude between the vertical beam orbit and the beam intensity vs. s	66
4.17	Amplitude of the sixth column of the temporal matrix U and the beam intensity vs. s	66
4.18	Contour plot of the reconstructed matrix D_q using only the sixth singular value. The arrows show the BPMs having a strong correlation between the measured vertical orbit and the beam intensity.	67
4.19	Measured vertical IP beam size (σ_y^*) vs. the beam intensity without applying DFS and WFS corrections and wakefield knobs.	68
4.20	Difference between the measured horizontal dispersion (D_x) and the target dispersion ($D_{x,target}$) in the ATF2 beamline before and after applying DFS correction vs. BPM number.	70
4.21	Difference between the measured vertical dispersion (D_y) and the target dispersion ($D_{y,target}$) in the ATF2 beam line before and after DFS correction vs. BPM number.	70
4.22	Norm of the difference between the vertical orbit at high intensity, 6.0×10^9 electrons (y_{HQ}) and at low intensity, 2.0×10^9 electrons, (y_{LQ}) vs. the number of iterations of the WFS correction.	71
4.23	Measured vertical IP beam size (σ_y^*) vs. the beam intensity without correction and with DFS and WFS corrections.	72
4.24	Impact of ATF2 wakefield knobs iterations measurements: 4 consecutive steps of the vertical IP beam size (σ_y^*) vs. the wakefield knobs movers' positions.	73
4.25	Measured vertical IP beam size (σ_y^*) vs. the beam intensity before and after applying wakefield knobs.	74
4.26	Comparison between measurements and simulations of the vertical beam size at the IP (σ_y^*) vs. the beam intensity and the intensity-dependent parameter w	75
5.1	The ILC BDS 250 GeV phase advance (top) and the ILC BDS 250 GeV Twiss parameters calculated with PLACET (bottom).	78

5.2	Transverse wakepotential in V/pC/mm of the ILC C-BPM, calculated with GdfidL for a vertical offset of 1 mm, Gaussian bunch length of 0.3 mm and 1 pC charge (in red). For reference, the distribution of the electrons in one bunch is shown (in blue).	79
5.3	Centered vertical phase space at the 250 GeV ILC BDS IP, $Y' - \bar{Y}'$ vs. $Y - \bar{Y}$, for 3 cases: no correction, One-to-one steering, DFS, WFS and One-to-one steering, DFS, WFS and knobs, calculated with PLACET with wakefields.	80
5.4	Average vertical beam size at the 250 GeV ILC IP (σ_y^*) vs. correction step: One-to-one, DFS, WFS corrections and IP tuning knobs. The red dashed line show the vertical beam size at the IP for a perfect machine, 7.7 nm.	80
5.5	Vertical IP beam size σ_y^* vs. beam intensity in the 250 GeV BDS, calculated with PLACET with wakefields.	82
5.6	The ILC BDS beam aperture profile vs. s	83
5.7	The ILC resistive walls wakepotential for a copper beam pipe with a constant radius of 10 mm for the length of a train (~ 218 km). The zoom shows the wakepotential for the length of the ILC BDS (~ 2254 m).	83
5.8	Vertical orbit deflection at the IP between the first and last bunch of a train Δy^* vs. bunch number for a train with a constant incoming position offset of $0.1\sigma_y$ of the train of bunches in the 250 GeV ILC BDS for 5 beam intensities, calculated with PLACET with resistive wall effects included.	85
5.9	Vertical orbit deflection at the IP between the first and last bunch of a train Δy^* vs. bunch number for a train with a constant incoming angle offset of $0.1\sigma_{y'}$ of the train of bunches in the 250 GeV ILC BDS for 5 beam intensities, calculated with PLACET with resistive wall effects included.	85
5.10	Vertical orbit deflection at the IP between the first and last bunch of a train Δy^* vs. beam intensity for three incoming constant position offsets of the train of bunches in the 250 GeV ILC BDS: $0.01\sigma_y$, $0.05\sigma_y$ and $0.1\sigma_y$, calculated with PLACET with resistive wall effects included.	86

5.11	Vertical orbit deflection at the IP between the first and last bunch of a train normalised by the IP vertical beam size ($\Delta y^*/\sigma_y^*$) vs. beam intensity for a train with incoming constant position and angle offsets of respectively $0.01\sigma_y$ and $0.01\sigma_{y'}$ in the 250 GeV ILC BDS, calculated with PLACET with resistive wall effects included.	86
5.12	Vertical orbit deflection at the IP between the first and last bunch of a train normalised by the IP vertical beam size ($\Delta y^*/\sigma_y^*$) vs. beam intensity for a train with incoming constant horizontal position and angle offsets of respectively $0.01\sigma_x$ and $0.01\sigma_{x'}$ and vertical incoming position and angle offsets of respectively $0.01\sigma_y$ and $0.01\sigma_{y'}$ in the 250 GeV ILC BDS, calculated with PLACET with resistive wall effects included.	87
5.13	Distribution of incoming position and angle offsets from $-0.05\sigma_{x,y}$ to $0.05\sigma_{x,y}$	88
5.14	Vertical orbit deflection at the IP between the first and last bunch of a train normalised by the IP vertical beam size ($\Delta y^*/\sigma_y^*$) vs. beam intensity for a train with a random and around zero incoming vertical and horizontal position and angle offsets of between -0.05 and 0.05σ in the 250 GeV ILC BDS, calculated with PLACET with resistive wall effects included.	88
5.15	250 GeV ILC luminosity degradation vs. relative vertical offset of the colliding beams.	89
5.16	The ILC BDS 500 GeV phase advance (top) and the ILC BDS 500 GeV Twiss parameters calculated with PLACET (bottom).	91
5.17	Centered vertical phase space at the 500 GeV ILC BDS IP, $Y' - \overline{Y'}$ vs. $Y - \overline{Y}$, for 3 cases: no correction, One-to-one steering, DFS, WFS and One-to-one steering, DFS, WFS and knobs, calculated with PLACET with wakefields.	92
5.18	Average vertical beam size at the 500 GeV ILC IP (σ_y^*) vs. correction step: One-to-one, DFS, WFS corrections and IP tuning knobs. The red dashed line show the vertical beam size at the IP for a perfect machine, 5.9 nm.	93
5.19	Vertical IP beam size σ_y^* vs. beam intensity in the 500 GeV BDS, calculated with PLACET with wakefields.	94

5.20	Vertical orbit deflection at the IP between the first and last bunch of a train Δy^* vs. bunch number for a train with a constant incoming position offset of $0.1\sigma_y$ of the train of bunches in the 500 GeV ILC BDS for 5 beam intensities, calculated with PLACET with resistive wall effects included.	95
5.21	Vertical orbit deflection at the IP between the first and last bunch of a train Δy^* vs. bunch number for a train with a constant incoming angle offset of $0.1\sigma_{y'}$ of the train of bunches in the 500 GeV ILC BDS for 5 beam intensities, calculated with PLACET with resistive wall effects included.	95
5.22	Vertical orbit deflection at the IP between the first and last bunch of a train Δy^* vs. beam intensity for three incoming constant position offsets of the train of bunches in the 500 GeV ILC BDS: $0.01\sigma_y$, $0.05\sigma_y$ and $0.1\sigma_y$, calculated with PLACET with resistive wall effects included.	96
5.23	Vertical orbit deflection at the IP between the first and last bunch of a train normalised by the IP vertical beam size ($\Delta y^*/\sigma_y^*$) vs. beam intensity for a train with incoming constant position and angle offsets of respectively $0.01\sigma_y$ and $0.01\sigma_{y'}$ in the 500 GeV ILC BDS, calculated with PLACET with resistive wall effects included.	96
5.24	Vertical orbit deflection at the IP between the first and last bunch of a train normalised by the IP vertical beam size ($\Delta y^*/\sigma_y^*$) vs. beam intensity for a train with incoming constant horizontal position and angle offsets of respectively $0.01\sigma_x$ and $0.01\sigma_{x'}$ and vertical incoming position and angle offsets of respectively $0.01\sigma_y$ and $0.01\sigma_{y'}$ in the 500 GeV ILC BDS, calculated with PLACET with resistive wall effects included.	97
5.25	Vertical orbit deflection at the IP between the first and last bunch of a train normalised by the IP vertical beam size ($\Delta y^*/\sigma_y^*$) vs. beam intensity for a train with a random and around zero incoming vertical and horizontal position and angle offsets of between -0.05 and 0.05σ in the 500 GeV ILC BDS, calculated with PLACET with resistive wall effects included.	98
5.26	500 GeV ILC BDS luminosity degradation vs. relative vertical offset of the colliding beams.	99
6.1	CLIC BDS 380 GeV Twiss parameters calculated with PLACET. . .	101

6.2	CLIC BDS 380 GeV phase advance.	102
6.3	Geometry of the CLIC C-BPM, generated with GdfidL.	103
6.4	Transverse wakepotential in V/pC/mm of the CLIC C-BPM, calculated with GdfidL for a vertical offset of 1 mm, Gaussian bunch length of 70 μm and 1 pC charge (in red). For reference, the distribution of the electrons in one bunch is shown (in blue).	104
6.5	Centered vertical phase space at the 380 GeV CLIC BDS IP, $Y' - \overline{Y'}$ vs. $Y - \overline{Y}$, for 3 cases: no correction, One-to-one steering, DFS, WFS and One-to-one steering, DFS, WFS and knobs, calculated with PLACET with wakefields.	104
6.6	Average vertical beam size at the 380 GeV CLIC IP (σ_y^*) vs. correction step: One-to-one, DFS, WFS corrections and IP tuning knobs. The red dashed line show the vertical beam size at the IP for a perfect machine, 2.9 nm, calculated with PLACET with wakefields.	105
6.7	Vertical IP beam size σ_y^* vs. beam intensity in the 380 GeV BDS, calculated with PLACET with wakefields.	106
6.8	The CLIC BDS beam aperture profile.	107
6.9	The CLIC resistive walls wakepotential for a copper beam pipe with a constant radius of 15 mm for the length of the CLIC BDS (~ 1949 m). The zoom shows the wakepotential for the length of a train (~ 52.8 m).	107
6.10	Vertical orbit deflection at the IP between the first and last bunch of a train Δy^* vs. bunch number for a train with a constant incoming position offset of $0.1\sigma_y$ of the train of bunches in the 380 GeV CLIC BDS, calculated with PLACET with resistive walls.	108
6.11	Vertical orbit deflection at the IP between the first and last bunch of a train Δy^* vs. bunch number for a train with a constant incoming angle offset of $0.1\sigma_{y'}$ of the train of bunches in the 380 GeV CLIC BDS, calculated with PLACET with resistive walls.	109
6.12	Vertical orbit deflection at the IP between the first and last bunch of a train Δy^* vs. beam intensity for three incoming constant position offsets of the train of bunches in the 380 GeV CLIC BDS: $0.01\sigma_y$, $0.05\sigma_y$ and $0.1\sigma_y$, calculated with PLACET with resistive walls.	109

6.13	Vertical orbit deflection at the IP between the first and last bunch of a train normalised by the IP vertical beam size ($\Delta y^*/\sigma_y^*$) vs. beam intensity for a train with incoming constant horizontal position and angle offsets of respectively $0.01\sigma_x$ and $0.01\sigma_{x'}$ and vertical incoming position and angle offsets of respectively $0.01\sigma_y$ and $0.01\sigma_{y'}$ in the 380 GeV BDS, calculated with PLACET with resistive walls.	110
6.14	Vertical orbit deflection at the IP between the first and last bunch of a train normalised by the IP vertical beam size ($\Delta y^*/\sigma_y^*$) vs. beam intensity for a train with incoming constant horizontal position and angle offsets of respectively $0.01\sigma_x$ and $0.01\sigma_{x'}$ and vertical incoming position and angle offsets of respectively $0.01\sigma_y$ and $0.01\sigma_{y'}$ in the 380 GeV CLIC BDS, calculated with PLACET with resistive walls.	110
6.15	Vertical orbit deflection at the IP between the first and last bunch of a train normalised by the IP vertical beam size ($\Delta y^*/\sigma_y^*$) vs. beam intensity for a train with a random and around zero incoming vertical and horizontal position and angle offsets of between -0.05 and 0.05σ in the 380 GeV CLIC BDS, calculated with PLACET with resistive walls.	111
6.16	CLIC 380 GeV BDS luminosity degradation vs. relative vertical offset of the colliding beams.	112

Chapter 1

Introduction

Particle physics is the study of the fundamental constituents of matter. The fundamental structure of matter is summarized by the Standard Model [5]. Everything in the universe is made of building blocks called fundamental particles: the fermions, the particles that make up all matter, and the bosons, the particles that carry forces [6]. Fermions are either leptons or quarks.

There are three charged leptons, the electron, the muon and the tau, which all have a charge of $-1e$ (with e the elementary electric charge) and their respective corresponding neutrinos with zero charge ($0e$) [7].

There are six different quarks, Up, Charm, Top which have a charge of $+\frac{2}{3}e$ and Down, Strange, Bottom which have a charge of $-\frac{1}{3}e$. Quarks combine in pairs to make mesons or in triplets to make baryons. Protons and neutrons are baryons. Protons are made of two up quarks and one down quark, and neutrons of one up quark and two down quarks.

Three fundamental forces govern the interactions between those particles: the electromagnetic force that has an infinite range and is mediated by a massless particle, the photon (γ), the strong force that confines quarks into hadrons and is mediated by another massless particle, the gluon (g), and the weak force, responsible for the radioactive decay of atoms mediated by W^\pm and Z^0 bosons [8]. The list of leptons quarks and bosons with their respective charges is shown in Table 1.1.

A sixth boson, the Higgs boson which was predicted in 1964 by six physicists including P. W. Higgs [9]. It was finally observed in 2012 with the Large Hadron Collider (LHC) at the European Organization for Nuclear Research (CERN) with two detectors, the Compact Muon Solenoid (CMS) and A Toroidal LHC ApparatuS (ATLAS) [10][11]. In order to increase the production rate of Higgs bosons and thus to study the Higgs boson more precisely, new colliders are being designed.

Table 1.1: Fundamental leptons, quarks and bosons of the Standard Model.

Type		Symbol	Electric charge
Leptons	Electron	e	$-1e$
	Muon	μ	$-1e$
	Tau	τ	$-1e$
	Electron neutrino	ν_e	0
	Muon neutrino	ν_μ	0
	Tau neutrino	ν_τ	0
Quarks	Up	u	$+\frac{2}{3}e$
	Charm	c	$+\frac{2}{3}e$
	Top	t	$+\frac{2}{3}e$
	Down	d	$-\frac{1}{3}e$
	Strange	s	$-\frac{1}{3}e$
	Bottom	b	$-\frac{1}{3}e$
Bosons	Photon	γ	0
	W^+		$+1e$
	W^-		$-1e$
	Z^0		0
	Gluon	g	0
	Higgs	H^0	0

1.1 Circular and linear accelerators

From the Cockcroft-Walton generator in 1932 [12] to the first proton-proton collisions in the LHC in 2009 [13], particle accelerators have been used to study the particles of the Standard Model. The beam energy is one of the key parameters for those studies. Since, as the energy increases, the number of possible reactions also increases, there is a quest for higher and higher energies. A beam energy of 6.5 TeV was achieved in the LHC in 2015, the highest energy ever obtained in an accelerator [14].

In order to increase the energy of the particles, these particles go through accelerating cavities where an electromagnetic field is generated. This field accelerates the particles longitudinally. In the case of circular accelerators, the accelerating cavities can be used multiple times in order to accelerate the beam turn after turn. To keep the beam within a circular orbit, bending magnets are used. However, when a charged particle is being accelerated radially, electromagnetic radiation is emitted called synchrotron radiation. The radiated power, which causes undesired energy loss

in such accelerators, is defined as [15]:

$$P_\gamma = \frac{e^2 c}{6\pi\epsilon_0(m_0c^2)^4} \frac{E^4}{\rho^2} \quad (1.1)$$

where c is the velocity of light, ϵ_0 is the dielectric constant of vacuum, m_0 is the rest mass of the particle, E is the energy of the particle and ρ is the bending radius.

1.2 Circular and linear colliders

The accelerated particles are gathered into bunches and collided at an IP where new particles are generated from those collisions. The nature of the emitted particles and the interactions that can take place, depend on the center-of-mass energy of the collision. The rate R at which a given interaction X occurs when the beams collide is defined by:

$$R(X) = L\sigma(X) \quad (1.2)$$

with $\sigma(X)$ the cross-section of the interaction and L the luminosity. The luminosity is a key parameter in the study of colliding beams. The basic expression for the luminosity is [16]:

$$L = f_{coll} \frac{n_1 n_2}{4\pi\sigma_x^* \sigma_y^*} F \quad (1.3)$$

where f_{coll} is the average collision frequency, n_1 and n_2 are the number of particles in the colliding head-on bunches, σ_x^* and σ_y^* are respectively the horizontal and vertical Root Mean Square (RMS) beam sizes, and F is a factor of order 1 that takes into account geometric effects such as a crossing angle and finite bunch length and dynamic effects such as the mutual focusing of the two beam during the collision. In order to increase the number of events at the IP, one has to maximize the collision frequency, maximize the beam intensities (n_1 and n_2) and minimize the transverse beam sizes at the IP.

Higgs bosons were produced from proton-proton collisions in the LHC. Protons are not fundamental particles, they are made of quarks and gluons. Thus, the interactions that took place in the LHC are between quarks and gluons and not the protons themselves. Since the energy of each gluon and quark is not precisely known, uncertainties exist in the analysis of the products of the collisions. Furthermore, particle identification at the LHC detectors is hard due to the background in the collision events which comes from strong interaction between quarks and gluons. The collisions of leptons, which are point-like fundamental particles, leads to a lower background.

Using muons or taus would be challenging due to their really short lifetime, $2.2 \mu\text{s}$ and 290 fs respectively. Electrons and positrons are stable. Moreover, as seen in Eq. 1.1, $P_\gamma \propto \frac{E^4}{\rho^2}$, then circular electron colliders are more sensitive to synchrotron radiation than linear colliders. Thus, it seems that the next ideal large machine for studying the Higgs, so called Higgs factory, would be a linear electron-positron collider. The Higgs bosons would mainly be produced by Higgs-strahlung ($ee \rightarrow ZH$) and WW fusion ($ee \rightarrow \nu\nu H$) as shown in Fig. 1.1 [17].

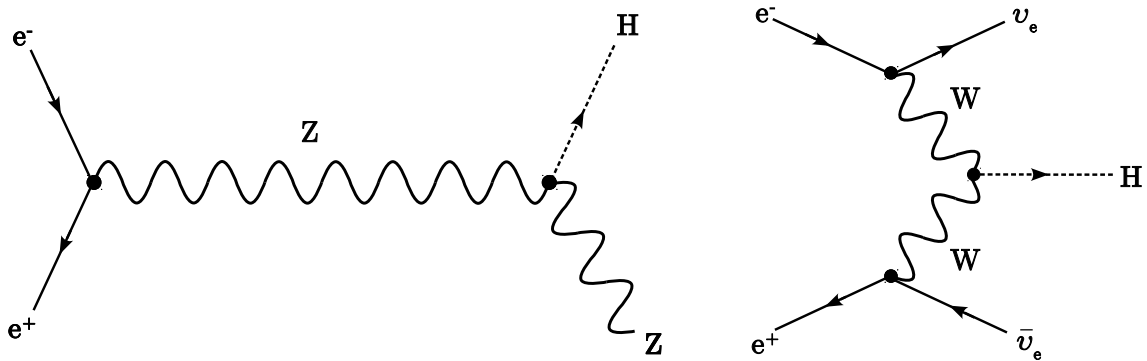


Figure 1.1: Feynman diagrams for production of Higgs bosons via Higgs-strahlung (left) and WW fusion (right).

1.3 Linear electron-positron colliders

There are two main future linear electron-positron collider designs, the International Linear Collider (ILC) and the Compact Linear Collider (CLIC).

1.3.1 The International Linear Collider (ILC)

The ILC is a linear electron-positron collider being considered for the post-LHC era. A centre of mass energy of 250 GeV would be achieved using the superconducting radio-frequency accelerating technology [18]. A schematic of ILC is shown in Fig. 1.2. Electrons are created by a photocathode DC gun. They then travel through a 5 GeV , 3.2 km long damping ring. They go through a two-stage bunch compressor system before being injected into the main LINAC. This high-energy electron beam then passes through an undulator producing high-energy photons which convert into electron-positrons pairs. Both electron and positron beams are injected into two 11 km long main LINACs using 1 GHz superconducting radio-frequency cavities. Those cavities operate with an average gradient of 31.5 MV/m . Finally, each beam travels through two BDS to the IP where a detector will study the collisions. In the BDS,

detailed in Sec. 5, the beam is focused to the nanometer scale after going through collimators, beam diagnostic systems, strong magnets, etc. A nanometer-level beam size is obtained at the IP thanks to a FFS scheme called local chromaticity correction [19]. This FFS is described in Sec. 2.1.3. Effects such as wakefields due to resistive-walls and Beam Position Monitors (BPMs) make the system very sensitive to the beam intensity.

1.3.2 The Compact Linear Collider (CLIC)

The Compact Linear Collider aims to collide e^+e^- beams with a center-of-mass energy up to 3 TeV. To obtain the high beam energy, an innovative two-beam acceleration design, using accelerating cavities made of copper is used, delivering an accelerating gradient of 100 MV/m [20]. The CLIC accelerating scheme plans to increase the beam energy from 9 GeV, coming from the Damping Rings, to 1.5 TeV in a single pass for the third energy stage. The high energy main beam is accelerated using RF power extracted from a secondary, high intensity but low energy, drive beam, using special RF devices called Power Extraction and Transfer Structures (PETS). The high current drive beam is obtained by recombining the bunches coming from the drive beam accelerator. This recombination is done in the delay loop and the combiner rings CR1 and CR2 [21, 22]. The beam travels then in the BDS, detailed in Sec. 6 where its size is squeezed to the nanometer level. The latest CLIC parameters, studies and results are summarized in the recent Project Implementation Plan [23].

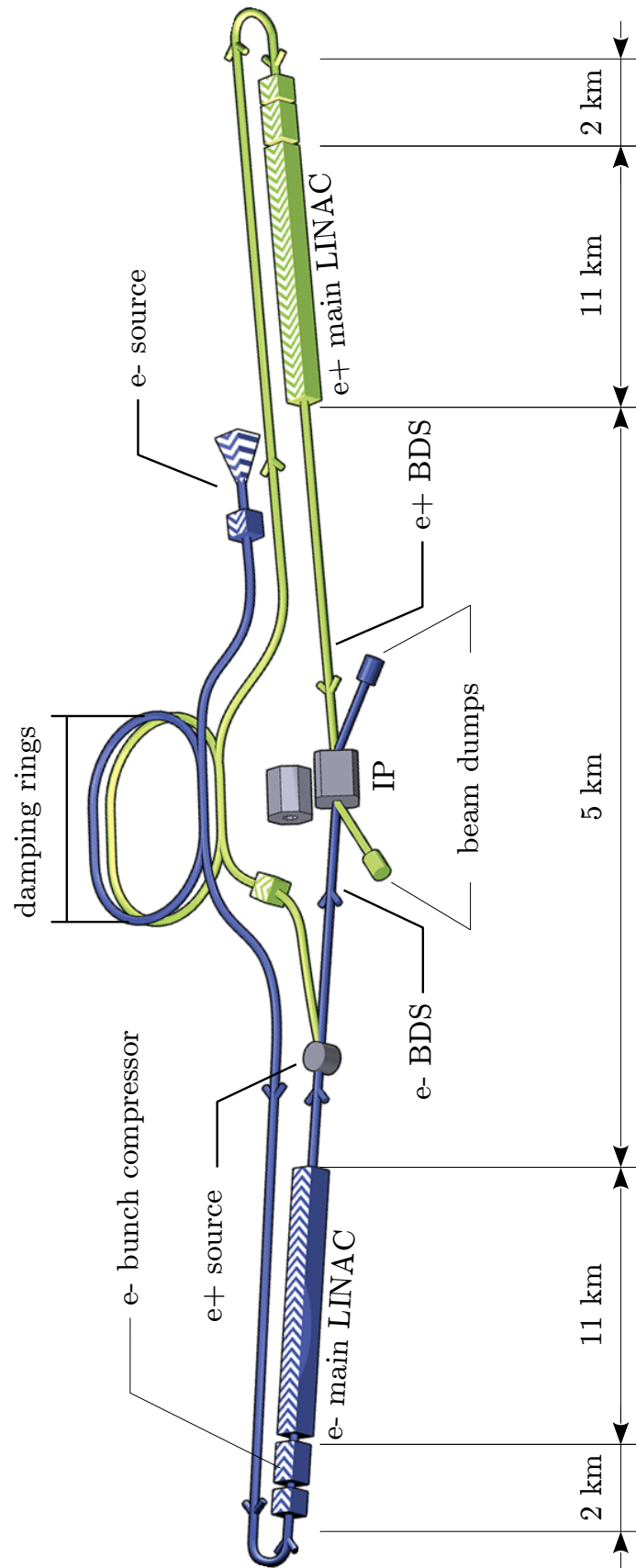


Figure 1.2: ILC 500 GeV layout with dimensions (not to scale) [1]

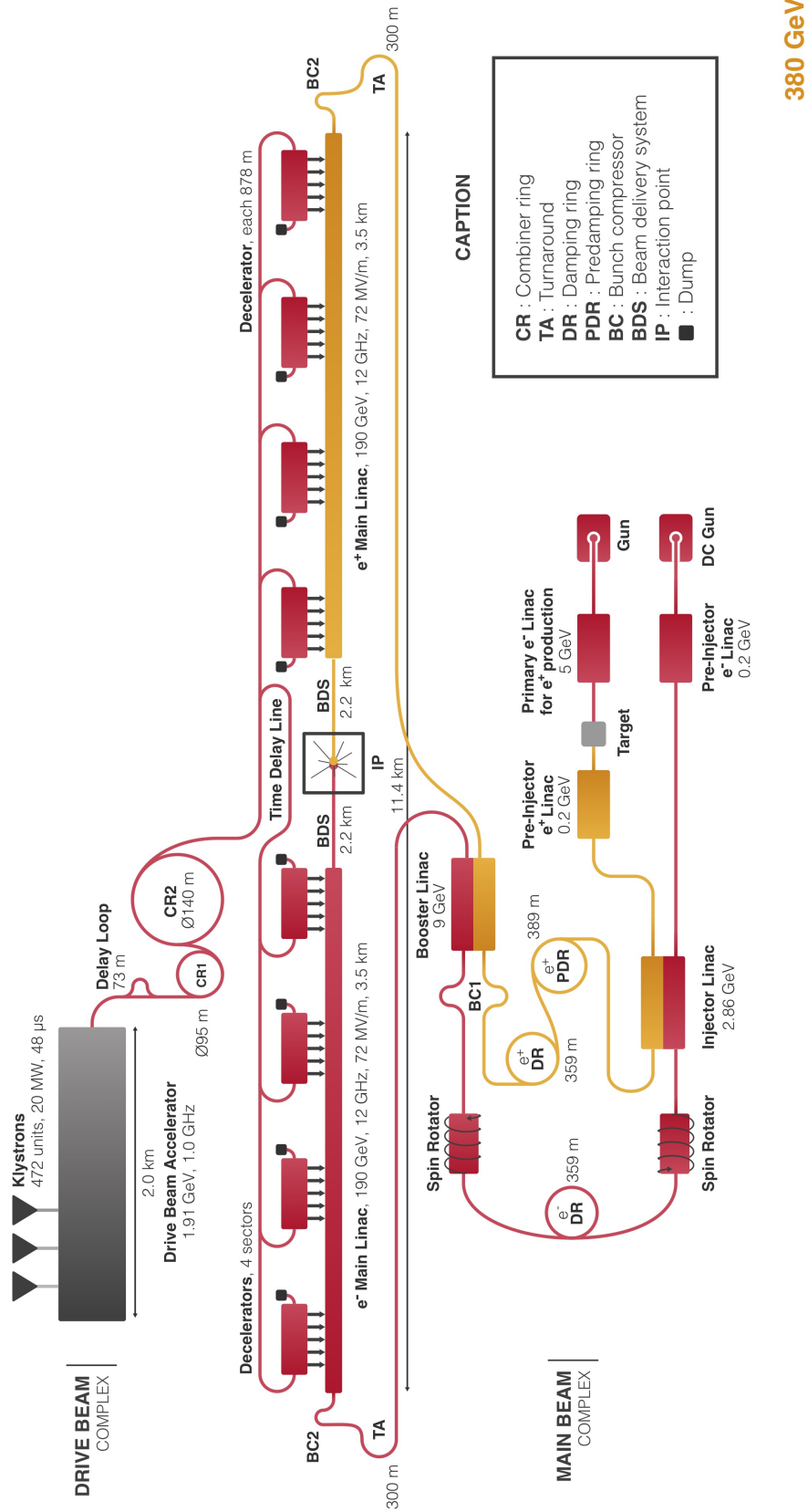


Figure 1.3: CLIC 380 GeV layout with dimensions (not to scale) [2]

1.4 Introduction to beam dynamics

In order to study the beam dynamics, a local 3-dimensional coordinate system (x, y, s) is defined as shown in Fig. 1.4, with x the radial outward direction, y the vertical upward direction, s the curved longitudinal particle trajectory and z the local tangent to s . The coordinate s gives the position along the beam line, the particles coordinates x and y measure the transverse distance from an ideal reference and z measures the longitudinal distance to the ideal reference. A bunch is made of particles. If $z < 0$ the particle is moving behind the bunch centre and arrives later in time than the bunch centre at an arbitrary reference position.

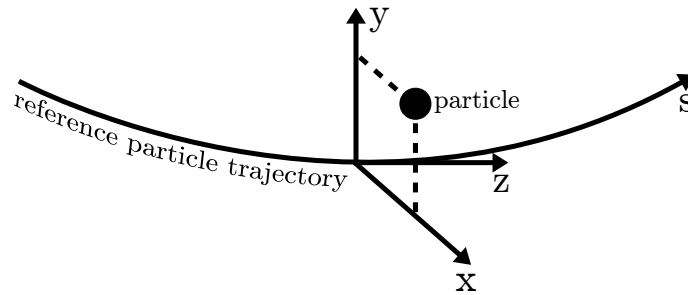


Figure 1.4: Schematics of the reference particle trajectory, the transverse and longitudinal coordinate system.

Considering a linear approximation, the vertical transverse motion of a particle is defined as:

$$y(s) = y_{r.t.}(s) + y_{\beta}(s) + D_y(s)\delta \quad (1.4)$$

with $y(s)$ the vertical coordinate at the location s , $y_{r.t.}$ the reference trajectory, y_{β} the vertical orbit variation due to the betatron motion (transverse oscillations) and $D_y\delta$ the orbit change due to an energy offset where D_y is the vertical dispersion function and $\delta = \Delta p/p$ is the relative deviation from the design momentum. Note that the horizontal transverse motion would follow Eq. 1.4 replacing y by x .

In order to focus the beam transversely, quadrupole magnets are used. The equation of vertical motion in one quadrupole follows:

$$\frac{d^2y}{ds^2} = -k(s)y \quad \text{with} \quad k = \frac{B_T}{(B\rho)a} \quad (1.5)$$

with $k(s)$ the normalised focusing strength, B_T the quadrupole pole-tip field, a the pole-tip radius and $(B\rho)$ the magnetic rigidity of the beam. In classical optics,

rays with different wavelengths will observe a different refractive index in a lens and therefore experience a different focal length. In accelerator physics, one can observe some similarities. Particles with different momenta feel a different focusing strength while traversing the same quadrupole and thus have a different betatron oscillation frequency. In order to correct the variation of the quadrupole focusing strength with the particle momentum, the so-called chromaticity, sextupole magnets are used. These are a non-linear elements which have to be installed at locations with nonzero dispersion to correct chromatic effects. The sextupole field is defined as:

$$m = \frac{2B_{T_s}}{(B\rho)a_s^2} \quad (1.6)$$

with B_{T_s} the sextupole pole-tip field, a_s the pole-tip radius and $(B\rho)$ the magnetic rigidity.

If one considers only the effects of linear elements, for a constant beam energy, the vertical betatron motion, solution of 1.5 follows [24]:

$$y(s) = \sqrt{\beta_y(s)}\epsilon \cos(\phi_y(s) + \phi_0) \quad (1.7)$$

with β_y the vertical beta function, ϵ the emittance and $\phi_y(s)$ the betatron phase. The beta function modulates the amplitude of the beam's betatron oscillations along the beamline, the emittance is a measure of the average spread of particle coordinates in a position-momentum phase space and the betatron phase represents the phase of the sinusoidal oscillation between two s positions in the machine. ϕ_0 is the initial phase of any given particle at $s = 0$. A phase advance of 2π means that a full period of oscillation is done between those two points.

In addition to the beta function, two functions are used to characterize the betatron motion, they are as follows:

$$\alpha(s) = -\frac{1}{2} \frac{d\beta(s)}{ds} \quad , \quad \gamma(s) = \frac{1 + \alpha^2(s)}{\beta(s)} \quad (1.8)$$

It is customary to describe the envelope of all particles of a beam in phase space by an ellipse, here in the vertical plane, described by:

$$\gamma y^2 + 2\alpha y y' + \beta y'^2 = \epsilon \quad (1.9)$$

where $y' = \frac{dy}{ds}$, α , β , γ are the already defined Twiss parameters and ϵ is the emittance. The area of the ellipse is equal to $\pi\epsilon$. The ellipse and some of its parameters are shown in Fig. 1.5. α , β and γ determine the shape and the orientation of the ellipse. Two

important parameters are defined: the vertical beam size $\sigma_y = \sqrt{\epsilon_y \beta_y}$ and the beam divergence $\sigma_{y'} = \sqrt{\epsilon_y \gamma}$.

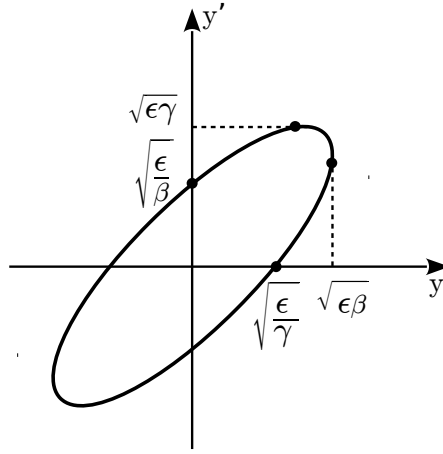


Figure 1.5: Schematics of the ellipse with selected parameters.

During a transformation along a beam transport line, the ellipse will continuously change its shape and orientation but will keep a constant area. A classic example is the “Focusing quadrupole-Drift-Defocusing quadrupole-Drift” (FODO) lattice. A schematic of this lattice is shown in Fig. 1.6. The first focusing quadrupole will focus the beam and, after a drift space, will reduce its beam size. It translates into a rotation of the ellipse of 90 degrees. Once the beam is focused, it is defocused by a defocusing quadrupole which, after a drift space, translates into another rotation of the ellipse of 90 degrees which brings the ellipse back to the initial position. Alternating focusing and defocusing quadrupoles are often used that way in order to keep the beam orbit stable.

These concepts will be used in the following chapters

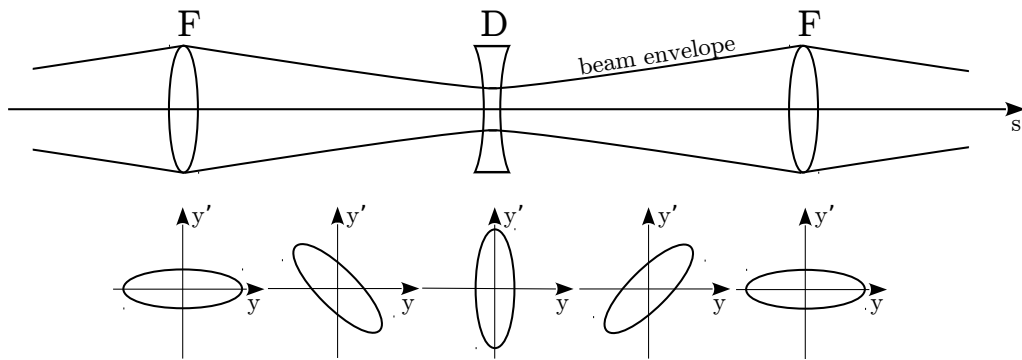


Figure 1.6: Evolution of the shape of the ellipse when going through the classical FODO lattice. F in this case means focusing in the vertical plane.

Chapter 2

The Accelerator Test Facility (ATF2)

2.1 ATF2 setup and goals

2.1.1 The ATF2 beamline

The Accelerator Test Facility 2 (ATF2) is a linear electron accelerator designed to study the feasibility of beam dynamics and technologies required for the next generations of linear colliders [25]. It was built at the Japanese High Energy Accelerator Research Organization (KEK). Beam operations began in 1997 with the ATF which had an initial goal of achieving small emittance beams which meet the requirements for future linear colliders such as the ILC. The goals were achieved in 2001 [26, 27]. In 2008, in order to study the challenges of obtaining and measuring nanometer beam sizes, ATF was upgraded to ATF2 [28]. ATF is made of an injector, a LINAC, a Damping Ring (DR), and the ATF2 beamline. The layout of ATF2 is shown in Fig. 2.2 [29]. As of January 2019, the ATF2 beamline consists of 49 quadrupoles, 5 sextupoles, 7 dipoles, 4 skew quadrupoles, 22 correctors (12 in the vertical plane and 10 in the horizontal one), 38 Beam Position Monitors (BPMs) (13 Stripline BPMs and 25 Cavity-BPMs (C-BPMs)). The beamline is made of a 52 m long extraction line (EXT) and a 38 m long Final Focus (FF) and matching section. A Radio Frequency (RF) gun generates bunches with a large range ($0.01 \times 10^{10} e^-$ per bunch to $1.0 \times 10^{10} e^-$ per bunch) at a frequency of 3.12 Hz. These bunches are accelerated to 1.28 GeV in an 88 m LINAC. They are then injected into a 139 m circumference damping ring where they are stored for between 100 and 450 ms. The beam emittance is reduced due to synchrotron radiation. This damping ring provides a vertical emittance of less than 10 pm which is comparable to the requirement of the ILC BDS [30, 31]. The electron bunches are extracted from the damping ring with a kicker [32]. They then

go through an emittance diagnostic section including Optical Transition Radiation monitors, which measure the transverse beam size and permit emittance reconstruction [33]. The beam is then transported, focused and tuned in order to obtain a nanometer beam size at the IP.

The relevant ATF2 design beam parameters are listed in Table 2.1. The Twiss parameters of the beamline are shown in Fig. 2.1. The chromaticity of the ATF2 beamline is designed to be comparable to the ILC final focus system with a resulting design IP vertical beam size of 37 nm. Recently, the ATF2 beamline has been operated with a 10 times larger horizontal IP beta-function, β_x , than originally designed so as to make the effect of multipole field errors comparable with the tolerances of the ILC final focus design. This optics is referred to as the 10×1 optics because of the 10 times larger β_x and the same β_y compared with the original design, while the nominal configuration is labeled 1×1 optics.

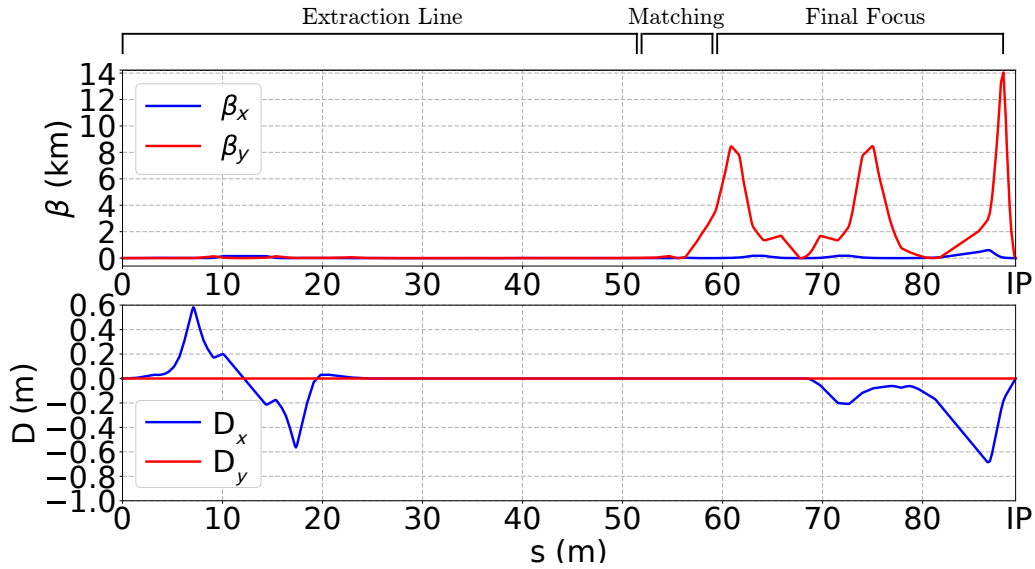


Figure 2.1: ATF2 Twiss parameters.

Table 2.1: Beam and optics design parameters for ATF2 beamline.

Parameter	Symbol	Value
Length of ATF2	L	90 m
Beam energy	E	1.28 GeV
Bunch population	N_e	1.0×10^{10}
Beta functions at IP	β_x^*/β_y^*	40 mm/0.10 mm
Beam sizes at IP	σ_x^*/σ_y^*	8.9 μm /37 nm
Bunch length	σ_z	7 mm

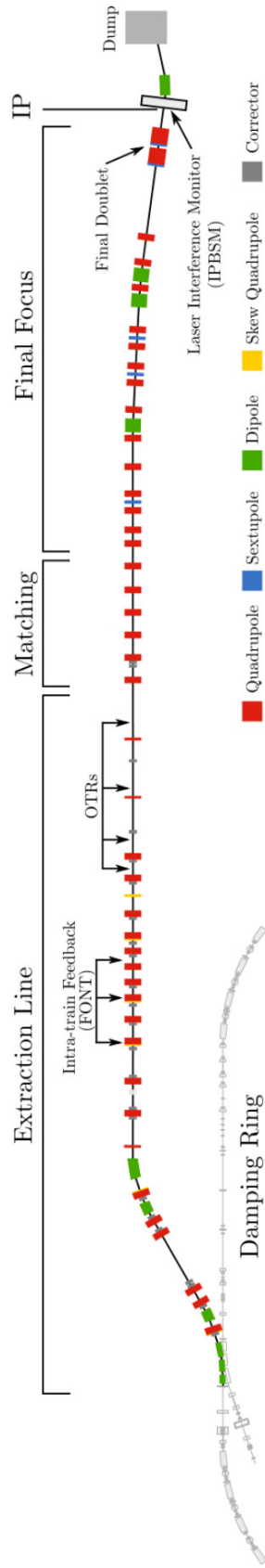


Figure 2.2: The layout of ATF2 [3]

2.1.2 Goals of ATF2

The ATF2 beamline was designed and built in order to fulfill two main goals:

- Goal 1: Achieve a small vertical beam size at the IP (37 nm) and demonstrate the efficiency of the Final Focus System based on local chromaticity correction;
- Goal 2: Control the beam position and demonstrate the efficiency of the beam orbit's stabilisation to the nanometer level at the IP.

Significant resources and work have been put in during these last few years in order to achieve goal 1. A minimum vertical beam size of 42 nm was measured in 2016 as shown in Fig. 2.3 [34]. However, due to several machine imperfections, which are defined in section 4.2, such a small beam size was hardly achieved since then. Furthermore, these measurements were obtained with a beam intensity of 1×10^9 electrons per bunch, 10% of the nominal intensity.

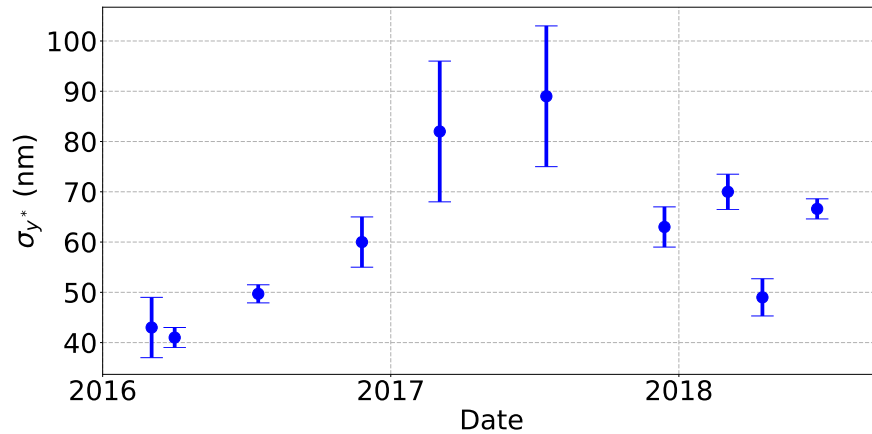


Figure 2.3: The ATF2 vertical IP beam size measurement history.

2.1.3 The final focus system and local chromaticity correction

The ATF2 beamline was built to study the ILC FFS based on the local chromaticity correction technique [19]. The optical layout of the system is shown in Fig. 2.4. In order to obtain nanometer-scale beams at the IP, the beam is focused by Final Doublet (FD) magnets: QF1 and QD0. However, the strong focusing magnets of the FD generate chromaticity. This chromaticity is corrected locally by two sextupoles (SF1 and SD0) adjacent to the FD quadrupoles and by dipoles upstream that generate dispersion across the FD (B2FF and B1FF). The sextupoles generate geometric

aberrations, so two more sextupoles in phase with them are placed upstream of the dipole magnets (SF5 and SD4) in order to correct those aberrations.

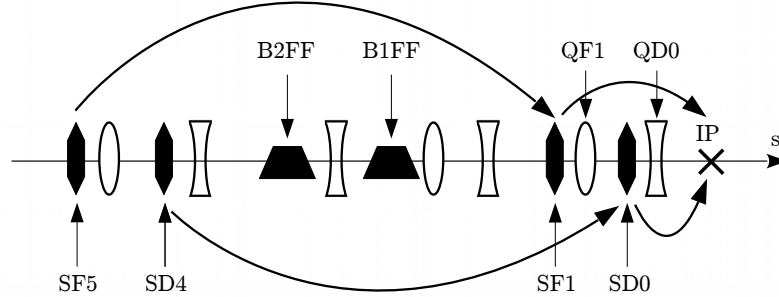


Figure 2.4: Optical layout of the final focus system based on local chromaticity correction.

2.1.4 ATF2 phase advance

The phase advance is one of the key parameters for the intensity-dependent effects studies. Indeed, depending on the phase advance, the impact of a kick will be different. Between the extraction of the DR and IP, the phase advance was designed to be 8π , which means that a kick at the extraction will lead to an angle offset at the IP and a position offset will lead to a position offset. The phase advance between the IP and positions upstream in the beamline is shown in Fig. 2.5.

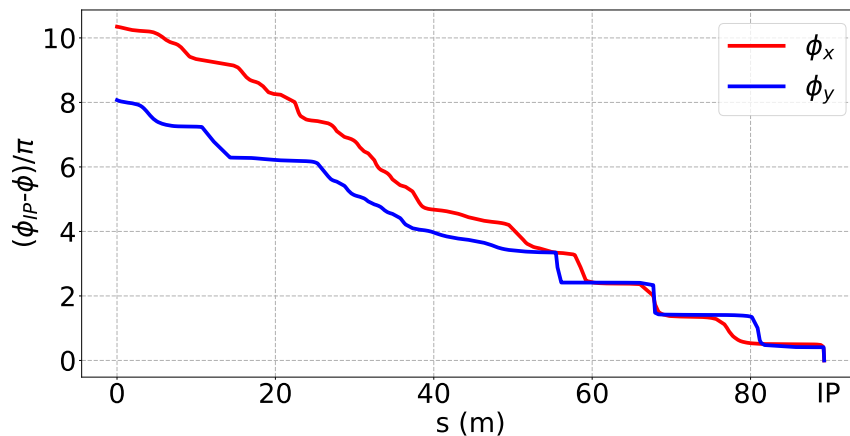


Figure 2.5: The phase advance between the IP and positions upstream in the beamline.

2.2 ATF2 beamline diagnostics

2.2.1 The IP Beam Size Monitor (IP-BSM)

A beam size monitor [35] was installed at SLAC FFTB during the 1990s, measuring a beam size of approximately 70 nm [36]. In order to measure beam sizes down to 37 nm, this IP Beam Size Monitor (IPBSM) was modified and installed at the ATF2 IP. A schematic of the system is shown in Fig. 2.6. It consists of an optical system for the lasers and a gamma detector. A laser beam with a wavelength $\lambda = 532$ nm is generated and sent to a vertical optical table located at the ATF2 IP where it is separated into two beams. These two beams create interference fringe patterns which are then intersecting with the electron beam. The laser fringe pitch is defined by the wavelength (λ) and crossing angle of the two laser paths (θ): $d = \lambda/2 \sin(\theta/2)$. The overlap of the laser fringe pattern and the electron beam creates Compton scattered photons. Those photons are detected downstream of the IP by the photon detector and the measured modulation depth of the laser interferometer (M) is written as a function of the IP vertical beam size (σ_y):

$$M = C |\cos \theta| \exp(-2k_y^2 \sigma_y^2) \quad (2.1)$$

$$M = \frac{N_+ - N_-}{N_+ + N_-} \quad (2.2)$$

with C the modulation reduction factor, which includes systematic effects such as the alignment accuracy, the polarization, the temporal coherence, the phase jitter, the tilt of the fringe pattern, etc. [37], θ the crossing angle of the two laser paths, $k_y = \pi/d$, $d = \lambda/2 \sin(\theta/2)$ and N_+ and N_- the maximum and minimum signal intensity, respectively. From Eq. (2.1), the beam size is expressed as a function of the modulation depth:

$$\sigma_y = \frac{1}{C} \sqrt{\frac{1}{2} \ln \left(\frac{C |\cos \theta|}{M} \right)}. \quad (2.3)$$

For ATF2, 3 laser crossing modes (2-8-degree mode, 30-degree mode, 174-degree mode) are used to increase the range of possible beam size measurements [38]; their dynamic ranges are shown in Fig. 2.7 [4].

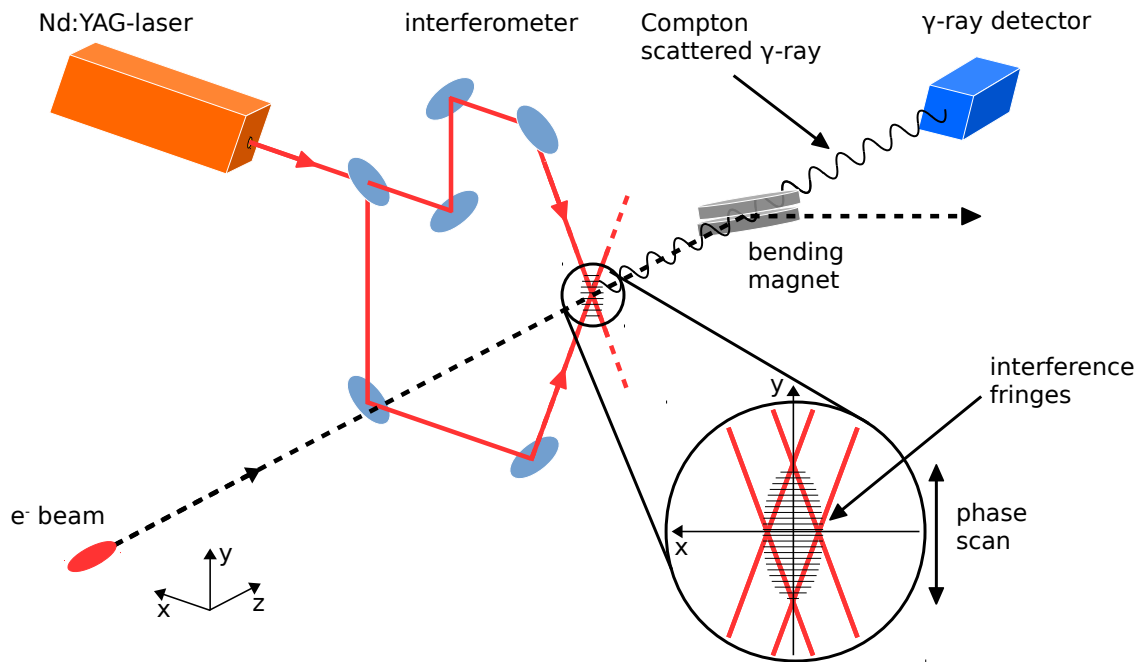


Figure 2.6: Schematic of the ATF2 IP Beam Size Monitor.

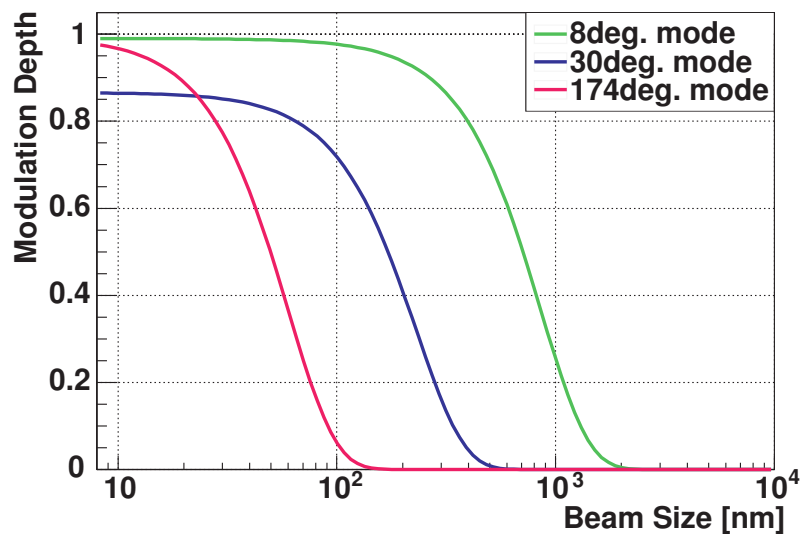


Figure 2.7: Dynamic ranges of the ATF2 IPBSM [4]

2.2.2 Beam Position Monitor (BPM) system

2.2.2.1 Stripline BPMs

In order to measure the beam position in the ATF2 beam line, a set of 38 BPMs are used: 13 stripline-BPMs and 25 Cavity-BPMs (C-BPMs). A picture and a schematic

of a FONT stripline-BPM, of the same type of the other stripline-BPMs used in the beamline, are shown in Fig. 2.8. Stripline-BPMs are made of four strips, or electrodes, and are connected via feedthroughs to the readout. The beam offset compared to the center of the BPM is determined by measuring the potential difference between the electrodes [39]. 13 stripline-BPMs are localised in the first half of the ATF2 extraction line. The first one is 3.09 m downstream of the extraction kicker and the last one is 32.72 m. They are able to measure the beam orbit in both planes with a resolution between $5\ \mu\text{m}$ and $20\ \mu\text{m}$ as shown in Fig. 4.11.

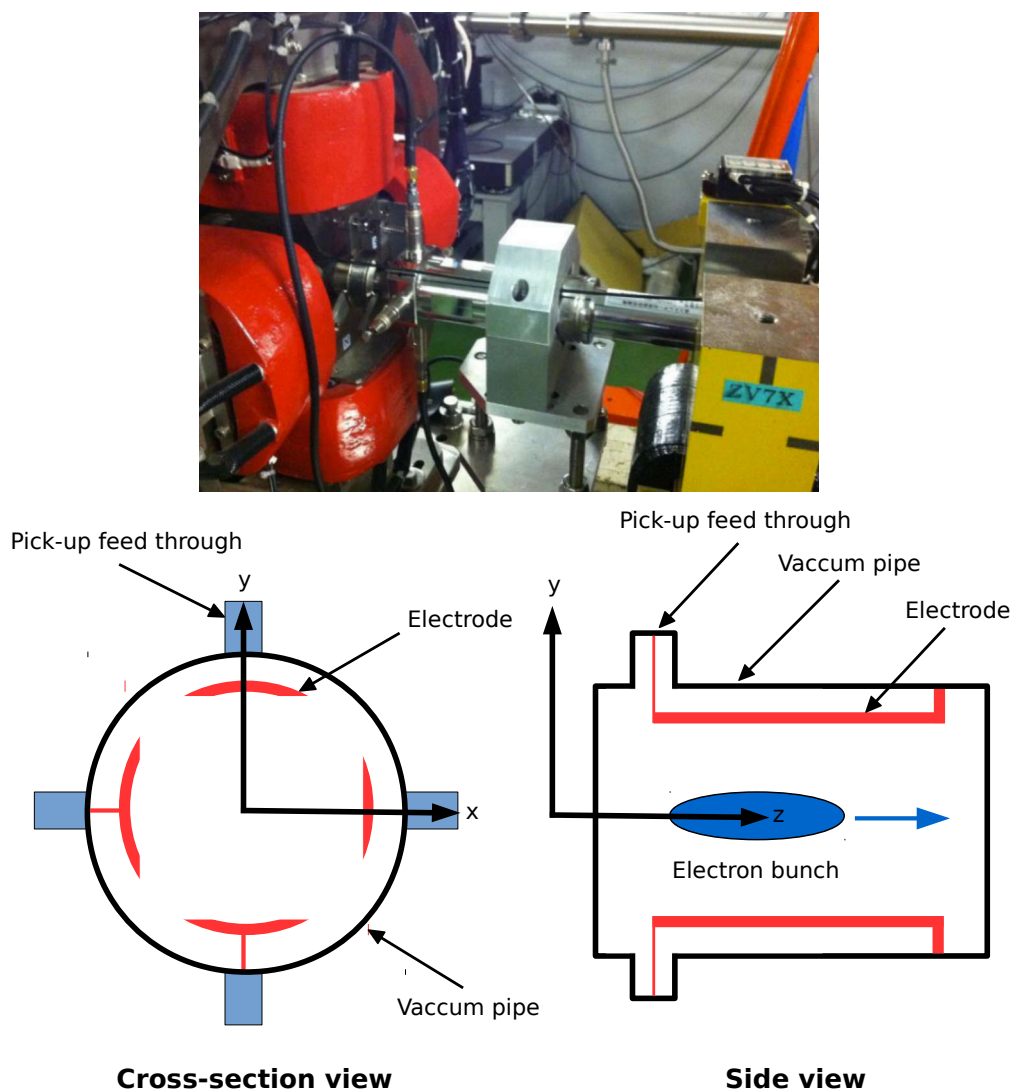


Figure 2.8: Picture of an ATF2 stripline (top) and schematic of a stripline BPM (bottom).

2.2.2.2 Cavity BPMs (C-BPMs)

The ATF2 C-BPMs are designed to operate using the dipole mode (TM₁₁₀) with a frequency of 6.422 GHz. This means that the dipole mode field strength depends linearly on the transverse beam offset from the cavity center, and it is zero for a beam centered within the cavity [39]. A picture and a schematic of the device are shown in Fig. 2.9. They have an aperture with a radius of 10 mm. This aperture is one of the smallest apertures in the beamline and thus, these C-BPMs create significant wakefield kicks that will be an important point in the rest of these studies. These C-BPMs have a resolution smaller than 1 μm as shown in Fig. 4.11.

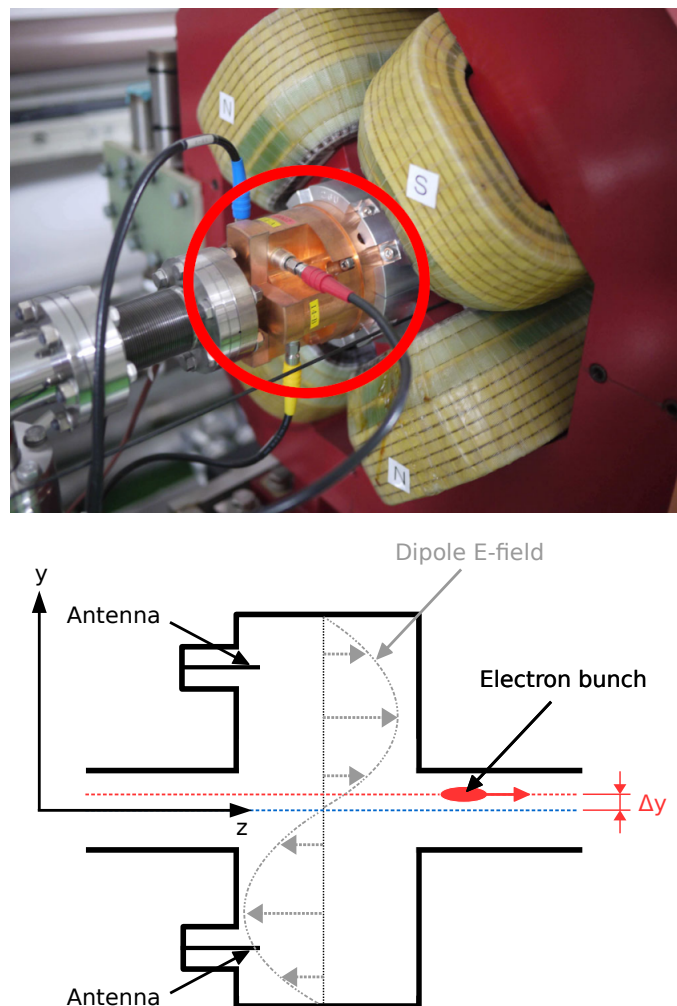


Figure 2.9: Picture of an ATF2 C-BPM (top) and schematic of a C-BPM (bottom).

2.2.3 Upstream FONT BPMs

A set of 3 stripline BPMs are located in the ATF2 extraction line between the BPMs MQF9X and MQD19X: P1, P2 and P3. They are part of the Feedback On Nano-Second Timescales 5 (FONT5) system used for stabilizing the vertical beam position in the upstream ATF2 beamline [40]. The positions on P1, P2 and P3 are shown in Fig. 2.10. The design goal for the FONT5 system is to stabilize the vertical beam position to the 1 μm level at the entrance to the final-focus system. These three stripline BPMs measured the beam orbit with a resolution of around 291 ± 10 nm at $0.5 \times 10^{10} e^-$ [41, 42, 43].

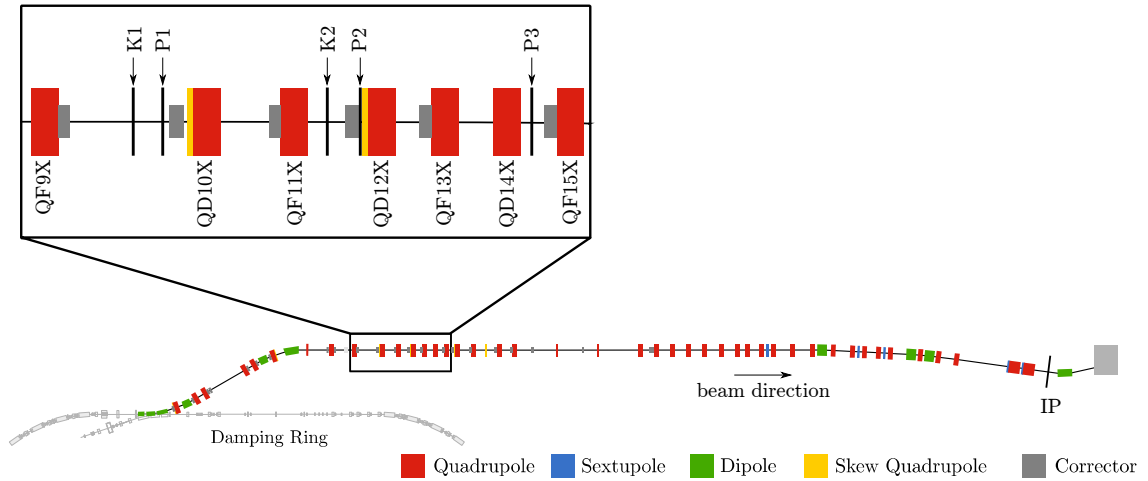


Figure 2.10: Schematic of the ATF2 beamline showing the positions of the upstream FONT BPMs.

2.2.4 FONT IP-BPMs

Three C-BPMs were installed in the interaction point region of ATF2. Two are located before the IP, IPA and IPB and the third one after the IP, IPC. The position of IPA, IPB and IPC are shown in Fig. 2.11. They were developed and optimized to measure the beam position with a nanometer-level resolution [44]. The BPMs are used to provide an input to a low-latency, intra-train beam position feedback system deployed in single-pass, multi-bunch mode with the aim of demonstrating intra-train beam stabilisation on electron bunches.

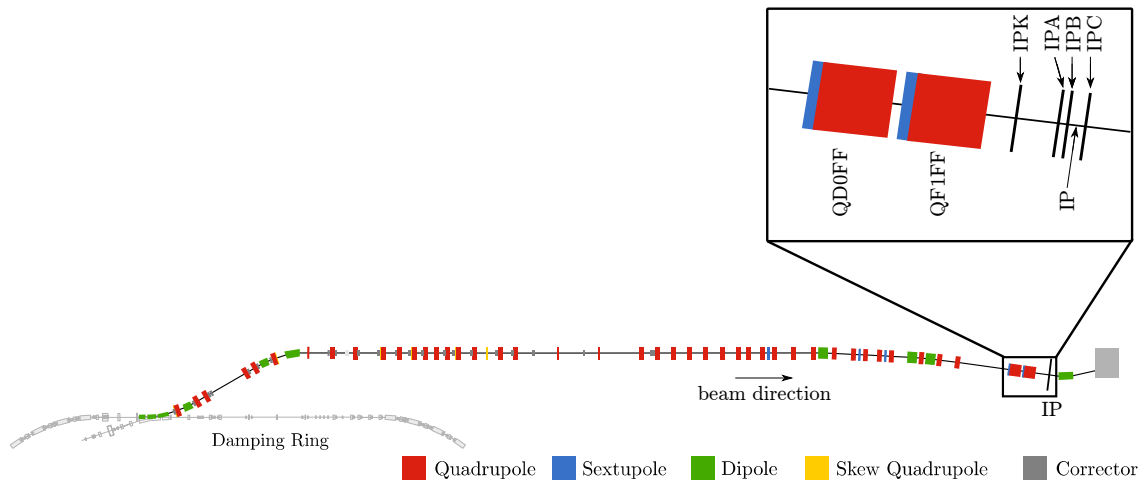


Figure 2.11: Schematic of the ATF2 beamline showing the positions of the IP-BPMs.

Chapter 3

Intensity dependent effects in ATF2: simulations

3.1 Introduction to wakefields

In order to understand the intensity-dependent effects in ATF2, one has to look at the impact of wakefields. The integrated fields seen by a test particle traveling on the same, or on a parallel path, at a constant distance s behind a point charge Q are called the integrated longitudinal (z direction) and transverse (x and y directions) wakepotentials [45]. They are respectively defined as:

$$\begin{aligned}\tilde{W}_\perp(\Delta r, s) &= \frac{1}{Q} \int_0^L [E_\perp(\Delta r, z, s) + c\hat{z} \times B(\Delta r, z, s)] dz \\ \tilde{W}_\parallel(s) &= -\frac{1}{Q} \int_0^L [E_z(z, s)] dz\end{aligned}$$

The wakepotentials are excited by a charged particle with charge Q located at $s = 0$ when it travels through a beamline component of length L with transverse offset with respect to the centre of the beam pipe Δr . The longitudinal wakepotential is a function of s ; whereas the transverse potential is also a function of Δr . The integrated wakepotentials \tilde{W}_\perp and \tilde{W}_\parallel are normally obtained using 3D electromagnetic solvers (e.g. GdfidL [46]) or using analytic models. Notice that the integrated wakepotential is normalized to the charge of the exciting particle, such that its units are V/C.

It is customary that the wakepotentials are normalized to the length of the element, L :

$$\begin{aligned}W_\perp(\Delta r, s) &= \tilde{W}_\perp(\Delta r, s) / L \\ W_\parallel(\Delta r, s) &= \tilde{W}_\parallel(\Delta r, s) / L\end{aligned}$$

such that the wakepotentials have units V/C/m. In the following, the symbol $\tilde{}$ is dropped and one indicates with W_{\perp} and W_{\parallel} the normalized wakepotentials, expressed in units of V/C/m.

The longitudinal and transverse transferred momenta experienced by a particle with charge q because of the wakepotentials W_{\perp} and W_{\parallel} while traveling through an element of length L , are then:

$$\begin{aligned}\Delta P_{\perp} &= \frac{qQL}{c} W_{\perp} && [\text{eV}/c] \\ \Delta P_{\parallel} &= -\frac{qQL}{c} W_{\parallel} && [\text{eV}/c]\end{aligned}$$

The transverse and longitudinal kicks felt by a particle, at position z along the bunch, due to all leading particles ($\forall z' : z' > z$):

$$\begin{aligned}\Delta r' &= \frac{\Delta P_{\perp}}{P} = \frac{qQL}{Pc} \int_{-\infty}^z W_{\perp}(\Delta r(z'), z - z') \rho(z') dz' \\ \Delta P_{\parallel} &= \frac{qQL}{c} \int_{-\infty}^z W_{\parallel}(z - z') \rho(z') dz'\end{aligned}$$

with:

- $\rho(z')$ normalized line charge density of the bunch, such that $\int_{-\infty}^{\infty} \rho(z') dz' = 1$
- $\Delta r(z')$ transverse radial position of the leading particles as a function of their position z' along the bunch [mm]
- Q total charge of the bunch [C]
- P particle's momentum [eV/c]

The wakefield functions are often approximated with their Taylor expansions with respect to Δr (normally, just zeroth and first orders are considered)

$$\begin{aligned}W_{\parallel}(s) &\Rightarrow W_{\parallel}(s) && \text{longitudinal monopole mode (0}^{\text{th}}\text{ order)} \\ W_{\perp}(\Delta r, s) &\Rightarrow \Delta r W_{1,\perp}(s) && \text{transverse dipole mode (1}^{\text{st}}\text{ order)}\end{aligned}$$

such that:

$$\begin{aligned}\Delta r'(z) &= \frac{qQL}{Pc} \int_{-\infty}^z W_{\perp}(\Delta r(z'), z - z') \rho(z') dz' \\ &\Rightarrow \frac{qQ}{Pc} \boxed{\text{L} \int_{-\infty}^z \Delta r(z') W_{1,\perp}(z - z') \rho(z') dz'} \\ \Delta P(z) &\Rightarrow qQ \boxed{\text{L} \int_{-\infty}^z W_{\parallel}(z - z') \rho(z') dz'}\end{aligned}$$

Such that the kick reads:

$$\Delta r' (z) = \frac{qQ}{Pc} \underbrace{\langle \Delta r \rangle}_{[\text{mm}]} \underbrace{\left[L \int_{-\infty}^z W_{1,\perp} (z - z') \rho (z') dz' \right]}_{\text{Tracking code input [V/C/mm]}} \quad (3.1)$$

$$\Delta P (z) = \frac{qQ}{c} \underbrace{\left[L \int_{-\infty}^z W_{\parallel} (z - z') \rho (z') dz' \right]}_{\text{Tracking code input [V/C]}} \quad (3.2)$$

where $\langle \Delta r \rangle$ is the average bunch transverse position in mm.

3.1.1 Two-particle model

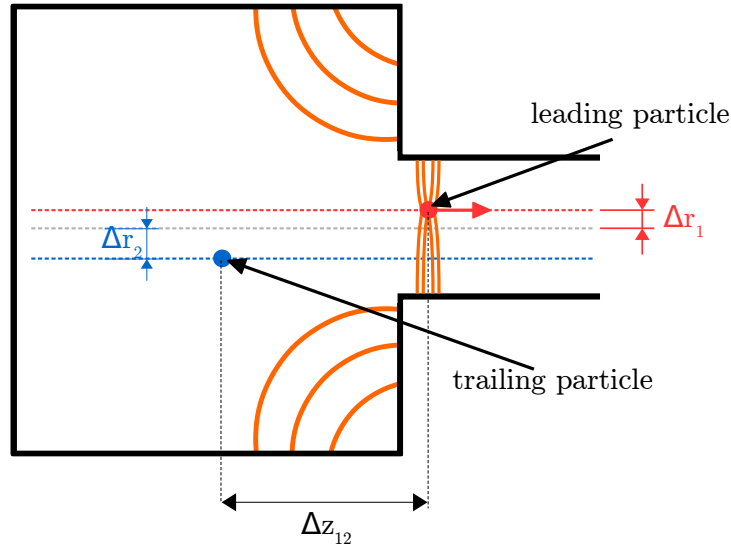


Figure 3.1: Scheme of the two-particle model.

A scheme of the two-particle model is shown in Fig. 3.1. In the two-particle beam model (1: leading, 2: trailing), the integrals become very simple:

$$\int_{-\infty}^z W_{1,\perp} (z - z') \rho (z') dz' \Rightarrow \boxed{W_{1,\perp} (\Delta z_{12})} \quad [\text{V/C/m/mm}]$$

$$\int_{-\infty}^z W_{\parallel} (z - z') \rho (z') dz' \Rightarrow \boxed{W_{\parallel} (\Delta z_{12})} \quad [\text{V/C/m}]$$

where Δz_{12} is the distance between the two particles (normally one takes $\Delta z_{12} \simeq 2\sigma_z$), and $W_{1,\perp}$ and W_{\parallel} are the single-particle normalized wake functions. Such that the kick on the trailing particle reads:

$$\Delta r'_2 = \frac{qQ/2}{Pc} L \Delta r_1 \boxed{W_{\perp} (\Delta z_{12})} \quad [\text{rad}]$$

$$\Delta P_2 = \frac{qQ/2}{c} L \boxed{W_{\parallel} (\Delta z_{12})} \quad [\text{eV}]$$

where Δr_1 is the offset of the leading particle.

3.1.2 Effects of wakefields on the beam

3.1.2.1 Single-bunch beam breakup

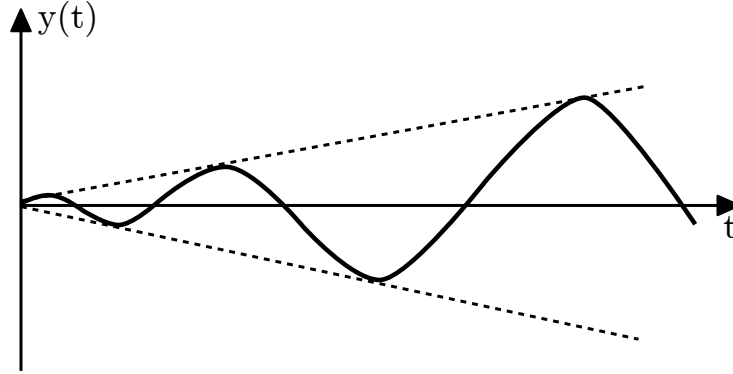


Figure 3.2: Resonant buildup of the displacement of the tail relative to the head of the bunch.

An important effect in high-intensity electron LINACs is single-bunch beam breakup, which is caused by the transverse dipole mode. As a result of the external focusing forces, an off-axis particle at the head of the bunch will execute transverse betatron oscillations about the beam axis. The tail particles would do the same as the head, if it were not for the transverse wakefields induced at the head that affect the tail. The effect of such wakefield is a resonant buildup of the displacement of the tail relative to the head of the bunch. See Fig. 3.2. The bunch shape, during beam breakup by the action of the dipole wakepotential, is heavily distorted and assumes a known “banana” shape. This induces an apparent transverse beam size growth.

3.1.2.2 Orbit deflection and beam size at the IP

In order to estimate the impact of the induced wakefields at a certain location, the wakefield kick given in Eq. (3.1) can be transported to the location of interest using the first order transport matrix formalism. Using this formalism, the horizontal and vertical position difference at the IP with and without a wakefield source, i , can be estimated as:

$$\Delta r(x, y)^* = \sqrt{\beta_{x,y}^i \beta_{x,y}^*} \sin \Delta \phi_{x,y}^{*i} \Delta r(x', y')^i \quad (3.3)$$

where $\beta_{x,y}^i$ is the betatron function at the wakefield source location, $\beta_{x,y}^*$ is the betatron function at the IP, $\Delta \phi_{x,y}^{*i}$ is the betatron phase advance difference between the wakefield source and the IP and $\Delta(x', y')^i$ is defined in Eq. (3.1).

The wakefields induced by the source i also induce a change on the transverse beam size at the IP. The transverse beam size at the IP, $\sigma_{x,y}^*$, taking into account the wakefields induced by the wakefield source i , can be estimated as [47]:

$$\sigma_{x,y}^{*2} = \sigma_{0x,0y}^{*2} + w^2 Q^2 \quad (3.4)$$

where $\sigma_{0x,0y}^*$ is the beam size at the IP without taking into account the wakefield, Q total charge of the bunch and w the intensity dependence parameter.

3.2 Simulations of corrections and intensity-dependent effects

3.2.1 Wakefield sources in ATF2

As previously explained, charged particles that travel across the vacuum chamber of an accelerator induce electromagnetic fields. They are enhanced by discontinuities in the beamline geometry. Devices such as C-BPMs or bellows in the beamline lead to a wakefield kick that alters the beam quality. In order to calculate the impact of wakefields in ATF2, simulations were done with PLACET [48], a code that simulates the dynamics of a beam in the main accelerating or decelerating part of a linac in the presence of wakefields, misalignments and other imperfections. It allows one to investigate single and multi-bunch effects, and to simulate different types of corrections [48]. In order to simulate with PLACET the impact of wakefields in ATF2, rigid-bunch simulations were considered. These simulations consist in computing the wakefield kick assuming that the longitudinal profile of the bunch is Gaussian and doesn't change along the beam trajectory. As stated earlier, the wakefield kick was calculated with GdfidL, an electromagnetic field simulator [46], assuming a 7 mm Gaussian beam with a charge of 1 pC traveling through the element with an initial transverse offset of 1 mm. There are three main wakefield sources in ATF2: C-BPMs, bellows and flanges.

3.2.1.1 Cavity BPMs (C-BPMs)

The main wakefield sources in the ATF2 beam line are the 25 C-BPMs [49]. The position of the C-BPMs is shown in Fig. 3.3. They are used to measure the horizontal and vertical beam orbit from the extraction of the damping ring all the way to the IP. The geometry of the ATF2 Cavity BPM, inputted in GdfidL, is shown in Fig. 3.4 with a beam aperture $a = 20$ mm, the resonator diameter $D_r = 53.7$ mm, the

resonator length $L_r = 12$ mm, the wave-guide height $h_w = 7.5$ mm and the wave-guide width $W_w = 28$ mm. The resulting calculated transverse wakepotential for a Gaussian bunch of 7 mm and a 1 pC charge with a vertical offset of 1 mm is shown in Fig. 3.5. The wakepotential is computed for a test bunch, and then normalized to the reference units in order to be scaled to any charge or any offsets one needs.

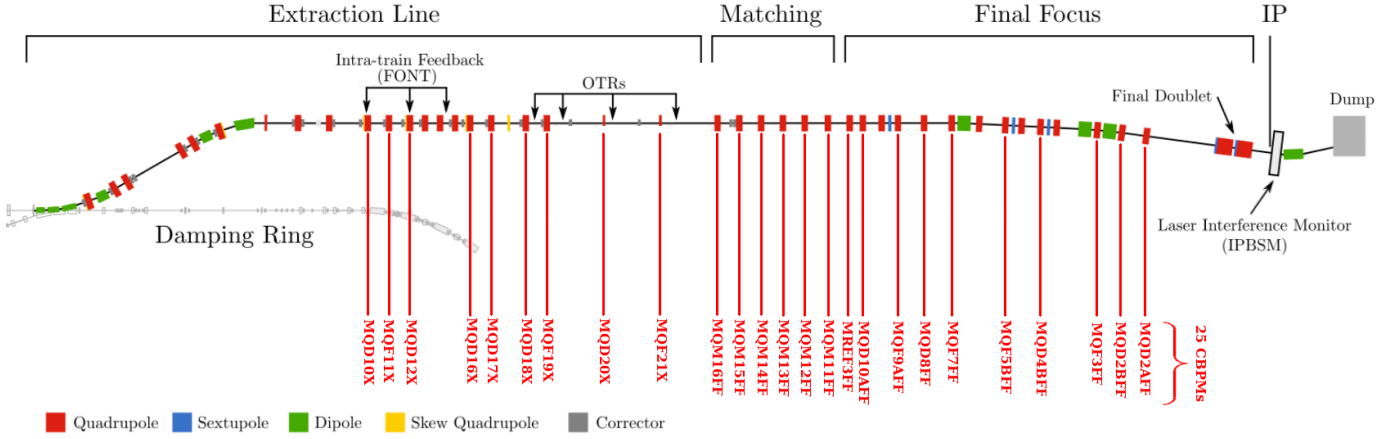


Figure 3.3: Positions of Cavity BPMS in ATF2.

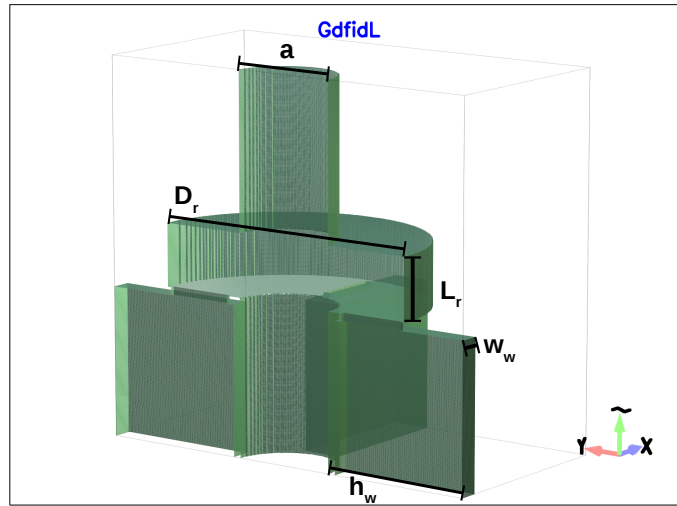


Figure 3.4: The geometry of the ATF2 C-band dipole cavity inputted in GdfidL.

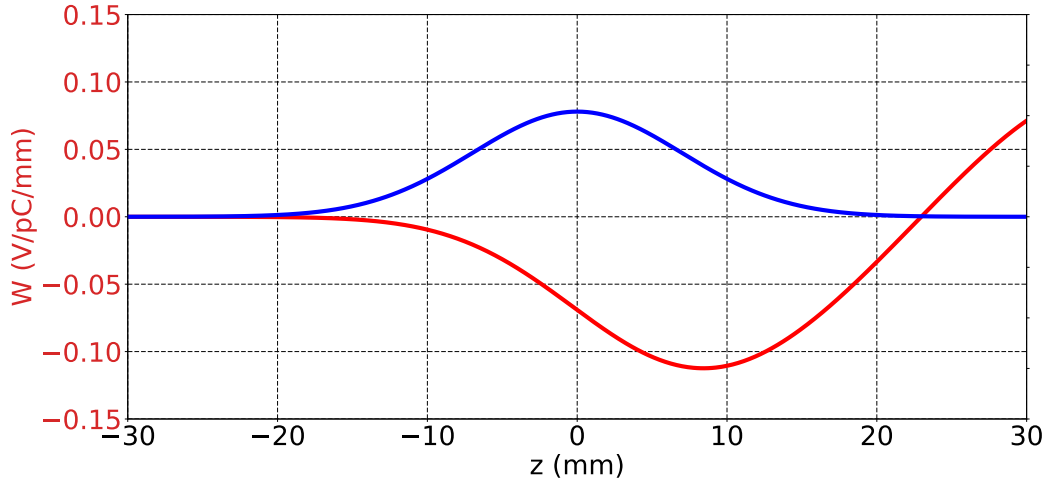


Figure 3.5: Transverse wakepotential of the ATF2 cavity BPM in V/pC/mm calculated with GdfidL for a Gaussian bunch of 7 mm RMS length and a 1 pC charge with a vertical offset of 1 mm and the Gaussian profile of the bunch (in red). For reference, the distribution of the electrons in one bunch is shown (in blue).

3.2.1.2 Bellows

ATF2 contains around 100 bellows. Most of them are masked and thus do not generate any wakefields. However, the unmasked bellows are strong wakefield sources. Their position is shown in Fig. 3.6. The geometry of the bellows used in the beamline is shown in Fig. 3.7 and the wakepotential is shown in Fig. 3.8. Bellows are the second strongest wakefield source in ATF2.

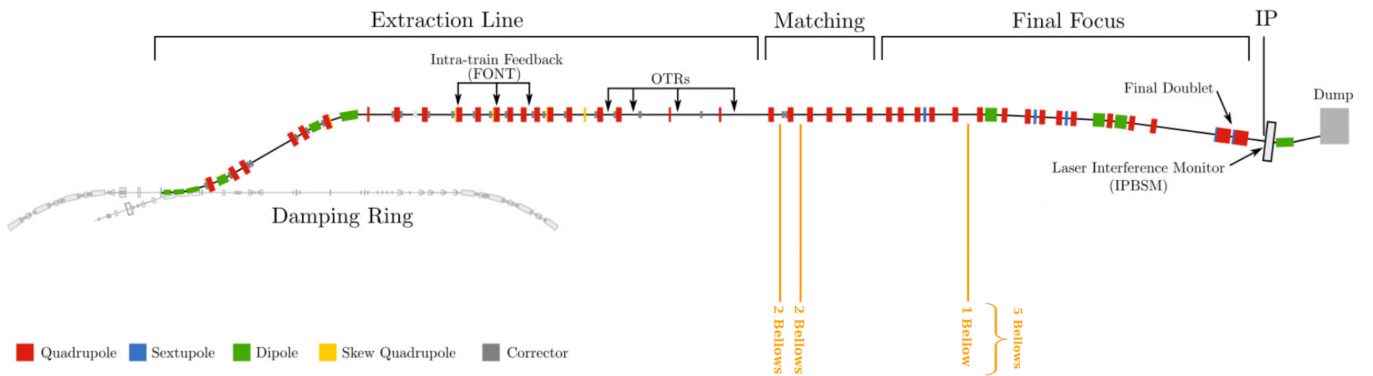


Figure 3.6: Positions of unmasked bellows in ATF2.

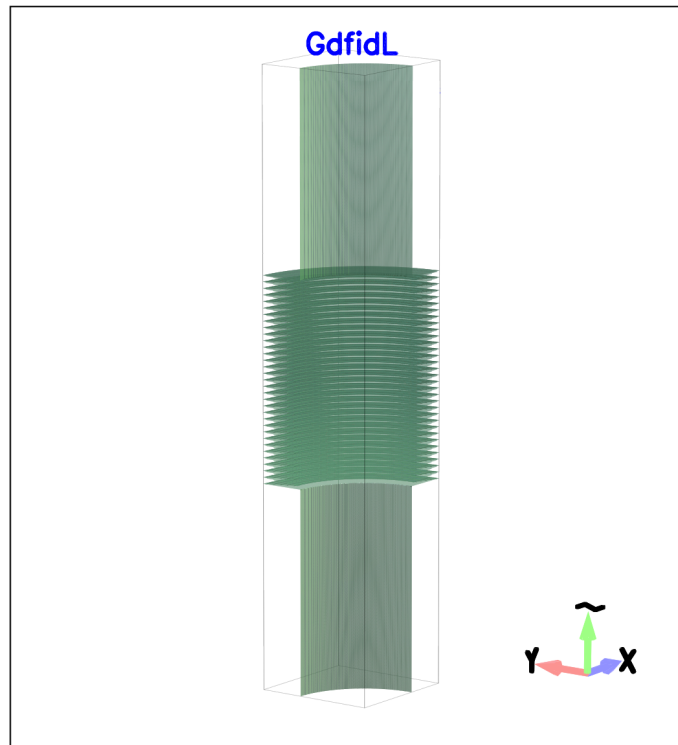


Figure 3.7: The geometry of the ATF2 bellows, inputted in GdfidL.

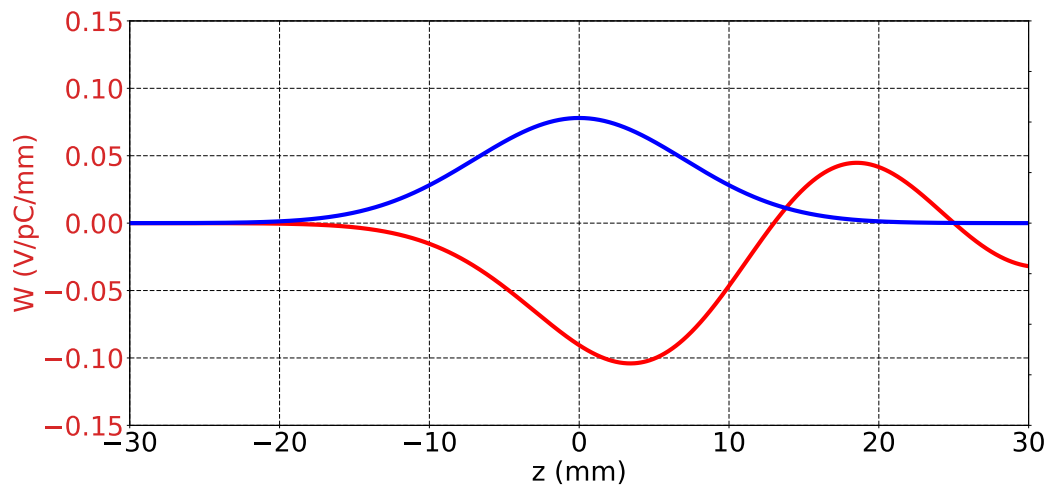


Figure 3.8: Transverse wakepotential of the ATF2 bellows in V/pC/mm calculated with GdfidL for a Gaussian bunch of 7 mm RMS length and a 1 pC charge with a vertical offset of 1 mm and the Gaussian profile of the bunch (in red). For reference, the distribution of the electrons in one bunch is shown (in blue).

3.2.1.3 Flanges

Finally, flanges, connecting the beam pipe and the elements, are also generating significant wakefields. Their position is shown in Fig. 3.9. The geometry of the flanges used in the beamline is shown in Fig. 3.10 and the wakepotential is shown in Fig. 3.11. Flanges are the third strongest wakefield sources in ATF2.

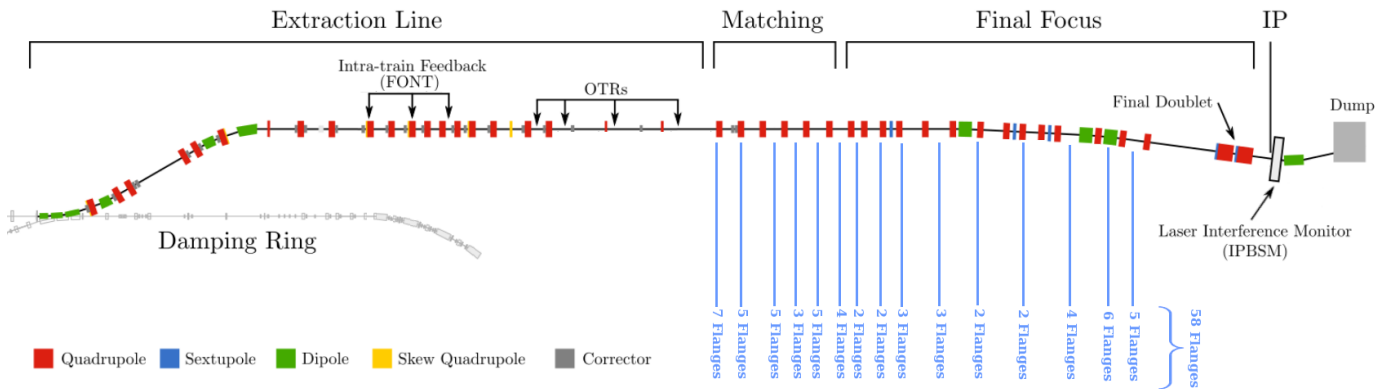


Figure 3.9: Positions of flanges in ATF2.

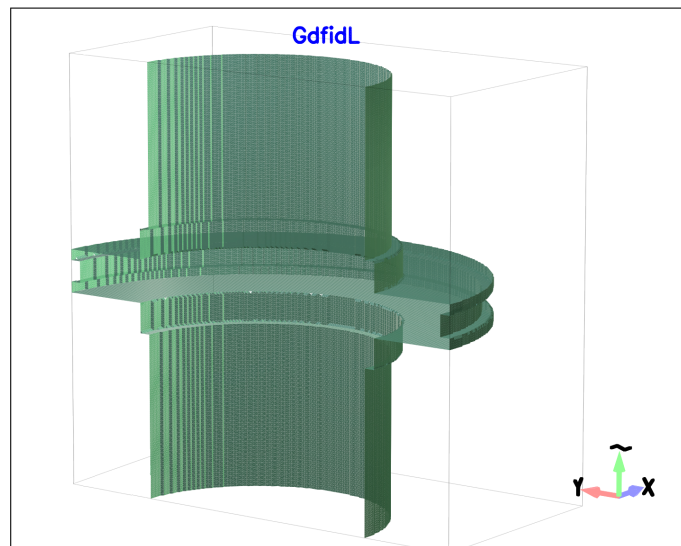


Figure 3.10: The geometry of the ATF2 flange, inputted in GdfidL.

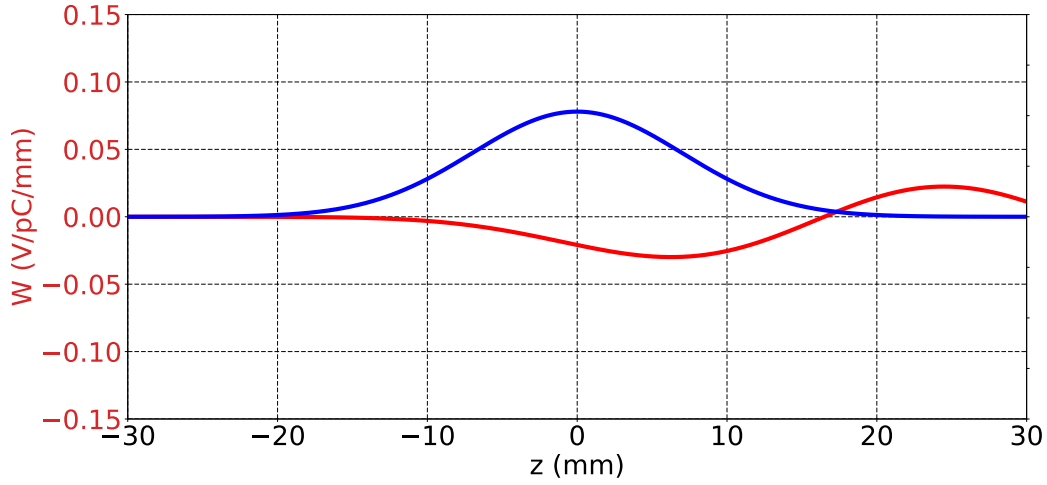


Figure 3.11: Transverse wakepotential of the ATF2 flange in V/pC/mm calculated with GdfidL for a Gaussian bunch of 7 mm and a 1 pC charge with a vertical offset of 1 mm and the Gaussian profile of the bunch (in red). For reference, the distribution of the electrons in one bunch is shown (in blue).

3.2.1.4 Summary

A summary of the wakefield sources with the mean wakepotentials, $|W_{mean}|$, in V/pC/mm, the peak wakepotentials, $|W_{peak}|$, and the number of sources is shown in Table 3.1. The precise positions of all wakefield sources in the ATF2 beamline are shown in App. A.

Table 3.1: Summary of wakefield sources in ATF2: number of sources, mean and peak wakepotentials in V/pC/mm.

Wakefield source element	Quantity	$ W_{mean} $ (V/pC/mm)	$ W_{peak} $ (V/pC/mm)
Cavity BPM	24	0.06	0.11
Masked bellows	~ 100	0	0
Unmasked bellows	5	0.06	0.1
Vacuum flange	58	0.02	0.03

3.2.2 Orbit, dispersion and wakefield corrections

In current and future particle accelerators, where a nanometer-scale emittance is achieved, high precision alignment of magnets and elements is required. Typical residual misalignments are in the range of 50-100 μm and in extreme cases, the alignment tolerances can be as small as 10 μm . In order to meet this goal and to maintain it, beam-based alignment techniques are used.

3.2.2.1 One-to-one correction

The One-to-one correction consists of minimizing the transverse position of the beam, with respect to the beam pipe centre, measured at BPMs. In ATF2, BPMs are located inside quadrupoles and steering magnets are used in order to kick the beam and make it pass through the center of the BPM. A schematic of the correction is shown in Fig. 3.12. In the beamline, the transverse centroid position of the beam measured downstream at the location $s = j$ is:

$$y_j = \sum_{i=0}^j \sqrt{\beta_i \beta_j} \theta_i \sin(\theta_j - \theta_i) \quad (3.5)$$

where θ_i is the dipole kick, i is the location of the initial disturbance and j the location of the observation. In matrix form:

$$\underbrace{\begin{pmatrix} y_1 \\ y_2 \\ \vdots \\ y_m \end{pmatrix}}_{\mathbf{x}} = \underbrace{\begin{pmatrix} \sqrt{\beta_1 \beta_1} \sin(\theta_1 - \theta_1) & \cdots & \sqrt{\beta_1 \beta_n} \sin(\theta_n - \theta_1) \\ \vdots & \vdots & \vdots \\ \vdots & \vdots & \ddots \\ \sqrt{\beta_m \beta_1} \sin(\theta_1 - \theta_m) & \cdots & \sqrt{\beta_m \beta_n} \sin(\theta_n - \theta_m) \end{pmatrix}}_M \cdot \underbrace{\begin{pmatrix} \theta_1 \\ \theta_2 \\ \vdots \\ \theta_m \end{pmatrix}}_{\boldsymbol{\theta}} \quad (3.6)$$

where y is the measured vertical orbit at m BPMs, θ is the angle kick applied at n correctors and M contains the transfer matrix elements between the correctors and the BPMs [50]. In ATF2, there are more BPMs than correctors. Thus, in order to minimize the orbit at BPMs, one has to calculate θ from Eq. 3.6 as:

$$\begin{aligned} M^t y &= M^t M \theta \\ \theta &= (M^t M)^{-1} M^t y \end{aligned} \quad (3.7)$$

where $(M^t M)^{-1} M^t$ is the so-called pseudo-inverse of M .

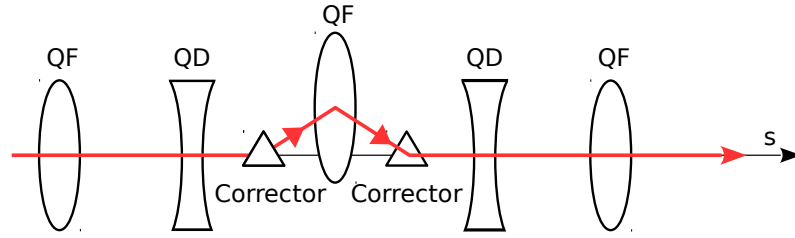


Figure 3.12: Schematic of the One-to-one correction. The beam orbit (in red) is deflected by correctors (triangles) in order to pass through the center of the BPM, which is inside a quadrupole in this case.

However, One-to-one correction does not address the effects of spurious transverse kicks due to magnet misalignments and steering magnets, which indeed generate unwanted dispersion. Thus a second correction is used, the Dispersion Free Steering.

3.2.2.2 Dispersion Free Steering (DFS)

The Dispersion Free Steering (DFS) is an algorithm which corrects the effects of unwanted dispersion, which leads to emittance growth [51]. In practice, two beams are tracked with two different energies, E_1 and E_2 . Steering magnets are then used to correct the orbit and reduce the orbit difference due to dispersion between the two beams $\Delta_{y,E}$. A schematic of the DFS is shown in Fig. 3.13.

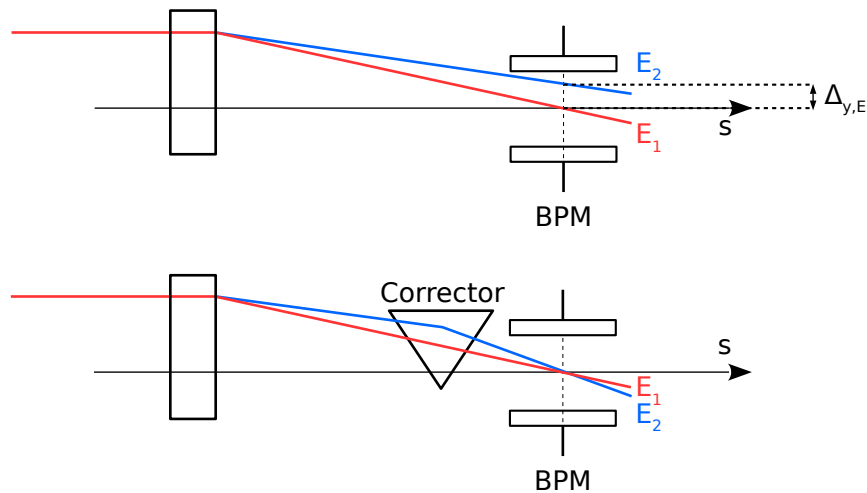


Figure 3.13: Schematic of the Dispersion Free Steering correction.

3.2.2.3 Wakefield Free Steering (WFS)

The Wakefield Free Steering (WFS) is an algorithm which corrects the difference in the orbit introduced by wakefields [52]. In practice, two beams are tracked with

different charges Q_1 and Q_2 . Steering magnets are then used to correct the orbit and reduce the orbit difference between the two beams $\Delta_{y,Q}$. A schematic of the WFS is shown in Fig. 3.14.

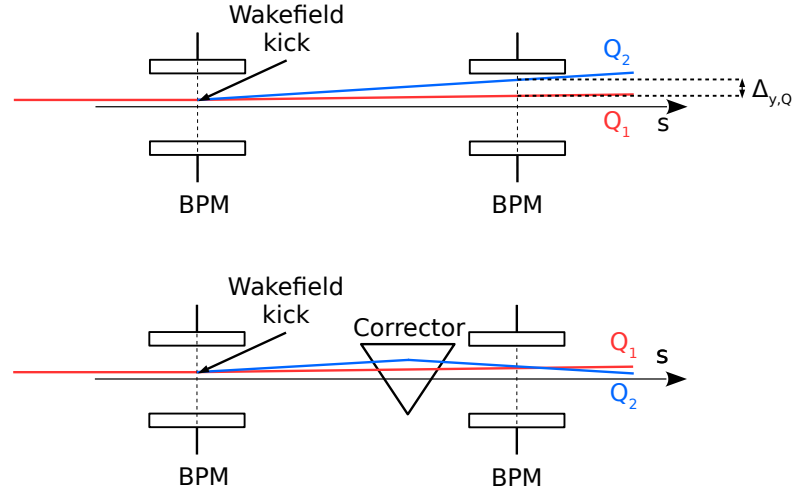


Figure 3.14: Schematic of the Wakefields Free Steering corrections.

3.2.2.4 IP tuning knobs

In ATF2, there are five sextupole magnets (SF6,SF5,SD4,SF1 and SD0). In order to correct the linear aberrations in the ATF2 FFS, sextupole magnets are displaced [53]. These sextupole knobs are orthogonal, meaning that the conditions between the sextupoles shifts are established to correct independently the chosen set of beam aberrations at the IP independently of the others. The transverse positions of all the sextupole magnets are set using movers. Each sextupole is displaced individually in the horizontal and vertical planes to build the corresponding aberration response matrices. When a sextupole magnet is moved horizontally, a quadrupole field is generated. The strength of the generated quadrupole field is proportional to the horizontal offset and changes the horizontal and vertical beam waists. In ATF2, three main linear aberration contributions, impacting the vertical beam size, are corrected during the tuning process. These aberrations are the vertical beam waist shift α_y^* , vertical dispersion η_y^* and x'/y coupling at the IP [54].

Nonlinear knobs are also constructed in order to correct the residual 2nd order aberrations at the IP. These knobs use the strength variations of the 5 sextupoles. They mainly reduce the correlations between y and x'^2 , between y and $x' \times y'$ and between y and $x' \times \eta_y$ [55].

3.2.2.5 Impact of One-to-one, Dispersion Free Steering, Wakefield Free Steering corrections and IP tuning knobs

The efficiency of the corrections was studied with PLACET. The ATF2 beam line with the wakefield sources listed in 3.2.1 was considered. A Gaussian bunch with 30,000 macro particles was tracked through 100 machines in order to sample the space of possible configurations. Each machine had a different random misalignment seed. Those machines have the following static errors: 100 μm RMS misalignment for quadrupoles, sextupoles and BPMs, 200 μrad RMS roll error for quadrupoles and sextupoles and a strength error of 0.01% RMS for quadrupoles and sextupoles. For this study, the beam intensity was $1.0 \times 10^{10} e^-$. As shown in Fig. 3.15 and summarized in Table 3.2, the average vertical beam size at the IP for 100 machines, $\overline{\sigma_y^*}$, is reduced from more than $13.8 \pm 86.2 \mu\text{m}$ with no correction to less than $1220 \pm 337 \text{ nm}$ after applying the One-to-one correction. Then, reducing the impact of dispersion and wakefields on the orbit, thanks to DFS and WFS corrections, reduced the average vertical beam size at the IP for 100 machines to $904 \pm 145 \text{ nm}$. Finally, the IP tuning knobs corrected the linear and second order aberrations and thus reduced the average vertical beam size at the IP for 100 machines to $58.4 \pm 4.7 \text{ nm}$, close to the design value of 37 nm for a perfect machine.

The implemented corrections, which are reproducing what was done in the real machine, permitted to obtain an average vertical beam size at the IP for 100 machines of $58.4 \pm 4.7 \text{ nm}$ which is in the same order of magnitude as the measured vertical beam size in the last four years as shown in Fig. 2.3.

Table 3.2: Summary of the impact of One-to-one, DFS, WFS corrections and IP tuning knobs on the vertical beam size at the IP (σ_y^*).

Correction	$\overline{\sigma_y^*}$
No correction	$13.8 \pm 86.2 \mu\text{m}$
One-to-one	$1220 \pm 337 \text{ nm}$
One-to-one + DFS + WFS	$904 \pm 145 \text{ nm}$
One-to-one + DFS + WFS + knobs	$58.4 \pm 4.7 \text{ nm}$

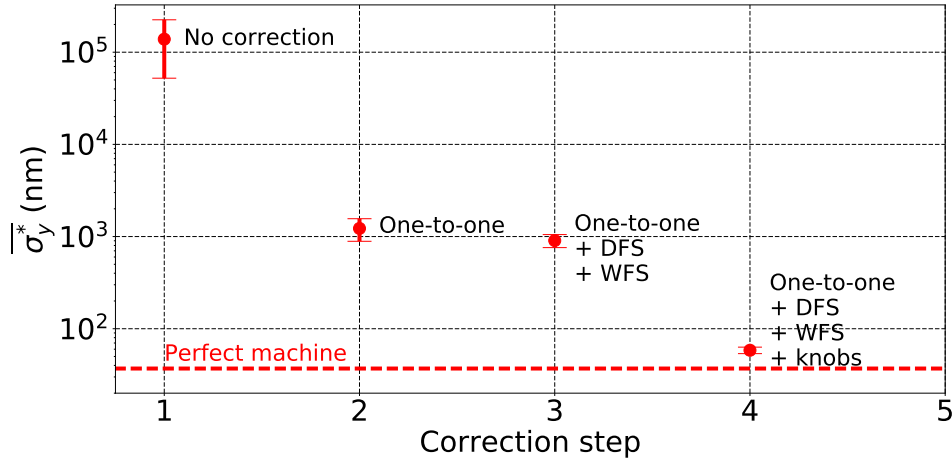


Figure 3.15: Average vertical beam size at the IP (σ_y^*) vs. correction step: One-to-one, DFS, WFS corrections and IP tuning knobs. The red dashed line show the vertical beam size at the IP for a perfect machine, 37 nm.

3.3 Impact of static errors: misalignments, spurious multipoles, rolls

In order to study the impact of static errors, a Gaussian bunch with 30,000 macro particles was tracked through 100 machines. In this first scenario, only misalignments of quadrupoles, C-BPMs and sextupoles were considered. Five different amplitudes of RMS misalignment were studied here: 0 μm (perfectly aligned machine), 25, 50, 75 and 100 μm . The impact of those misalignments on the average vertical IP beam size (σ_y^*) is shown in Fig. 3.16 as a function of the intensity. The dots correspond to the average of 100 machines and the error bars to the standard error, i.e. the standard deviation divided by the square root of the number of machines. The larger the misalignment amplitude, the larger is σ_y^* and this effect scales with the beam intensity. Indeed, the slope of each case shows that for a perfectly aligned machine, σ_y^* is the same at low and high beam intensity, but the larger the misalignment amplitude, the larger is the correlation between σ_y^* and the beam intensity. This is due to the fact that a larger misalignment amplitude leads to a larger orbit distortion at wakefield sources, thus a higher wakefield kick and a larger beam size at the IP.

In a similar way as for the misalignments, the impact of the multipole strength errors was studied. 100 machines with multipole strength errors of 10^{-4} RMS in both quadrupoles and sextupoles were considered. This means that each machine had a

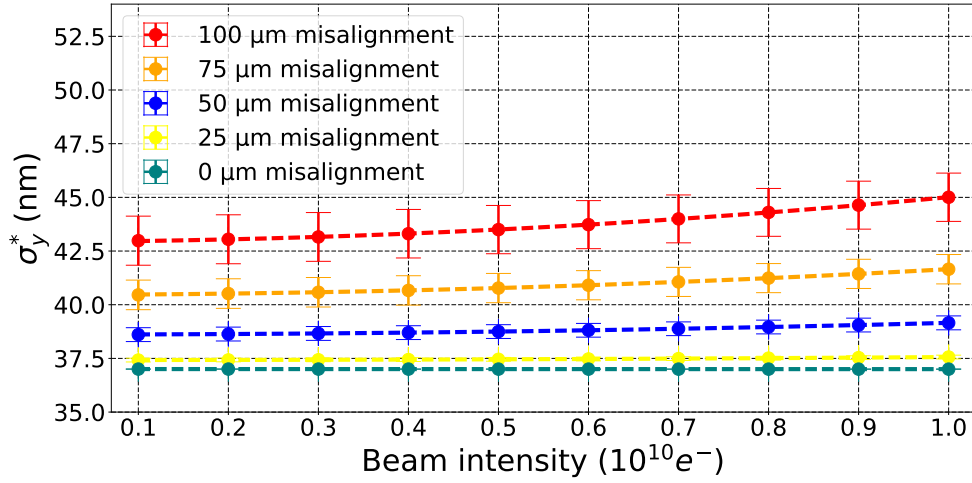


Figure 3.16: Effect of the misalignments on the vertical beam size at the IP (σ_y^*) vs. the beam intensity with wakefields calculated with PLACET.

different random strength error seed. Quadrupoles, sextupoles and C-BPMs are also misaligned by 100 μm RMS. The results are shown in Fig. 3.17. These strength errors increase the vertical IP beam size. Indeed, 38 perfect machines provided a vertical beam size of at most 38 nm, against 15 machines for the random multipole case.

Finally, the impact of roll errors (rotation around the magnet axis) of 200 μrad RMS was studied in BPMs, quadrupoles and sextupoles. The impact on the vertical beam size as function of the intensity can be seen in Figure 3.18 for the above simulation conditions. The error bars represent the standard error for 100 machines. The beam size growth due to such roll errors is around 2.2 nm at $0.2 \times 10^{10} e^-$ and around 4.4 nm at $1.0 \times 10^{10} e^-$. The impacts of static errors are summarized in Table 3.3.

Table 3.3: Summary of the impact of the static and dynamic errors on the vertical IP beam size at low/high intensity in presence of wakefields calculated with PLACET.

Static error	Misalignment	Strength error	Roll error
Error amplitude	100 [μm]	1×10^{-4}	200 [μrad]
Average σ_y^* at $10^9 e^-$ [nm]	43 ± 1.1	39 ± 0.09	39 ± 0.16
Average σ_y^* at $10^{10} e^-$ [nm]	45 ± 1.1	42 ± 0.29	41 ± 0.49

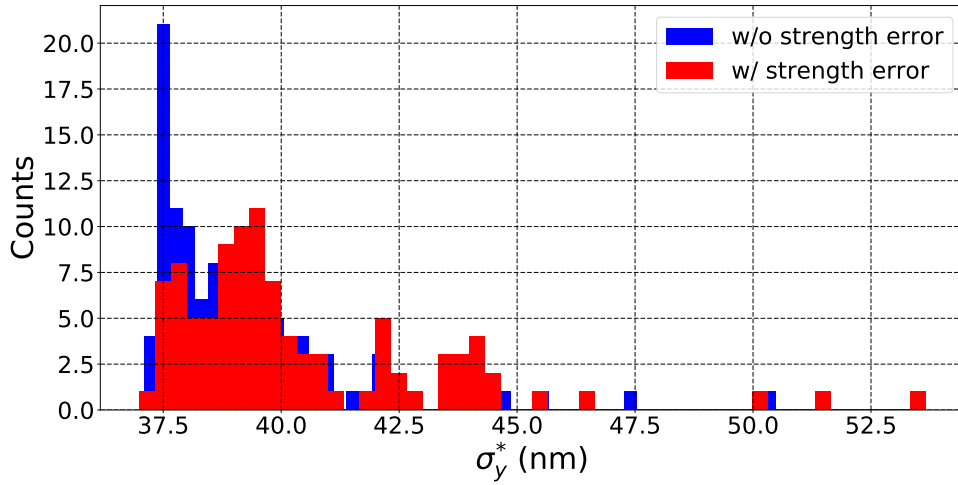


Figure 3.17: Effect of quadrupoles and sextupoles strength error of 10^{-4} RMS at $1.0 \times 10^{10} e^-$ on the vertical IP beam size (σ_y^*), in presence of wakefields calculated with PLACET.

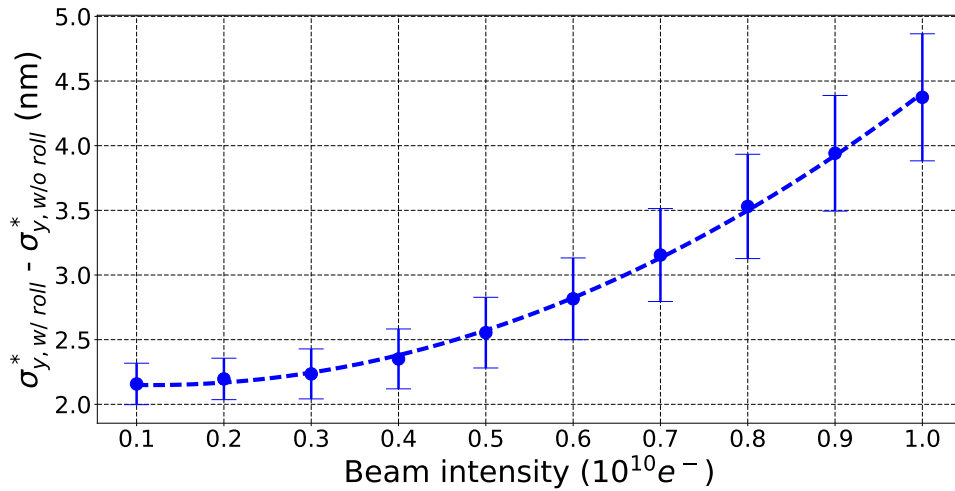


Figure 3.18: Effect of 200 μ rad RMS rolls of BPMs, quadrupoles and sextupoles on the vertical IP beam size (σ_y^*) vs. the beam intensity, in presence of wakefields calculated with PLACET.

3.4 Impact of dynamic errors: incoming position and angle jitters

Static errors are not the only errors which have a significant impact of the vertical beam size. One also has to study the impact of dynamic errors. Indeed, the incom-

ing jitter is one of the key parameters to quantify and to understand the intensity-dependent effects in ATF2. The ATF2 beam is injected in the extraction line with both angle and position jitters [56]. In order to study their impact, the following simulation conditions were considered: quadrupoles, C-BPMs and sextupoles have a misalignment of 100 μm RMS and a roll error of 200 μrad RMS and the strength error of quadrupoles and sextupoles is 10^{-4} RMS. In this case again, One-to-one, DFS, WFS corrections, as well as IP knobs were applied on each machine. This was done for 100 machines and 200 pulses per machine.

In order to quantify the amplitude of the incoming jitter, measurements were performed in ATF2 using the FONT upstream BPMs. An incoming position jitter of $1.0\sigma_y$ and an angle jitter of $1.0\sigma_{y'}$ were measured, with $\sigma_{y'}$, the beam divergence ($\sigma_{y'} = \sqrt{\gamma\epsilon}$). The detailed studies can be found in section 4.3.

In the simulations, four amplitudes of jitter: $0.1\sigma_y$, $0.3\sigma_y$, $0.5\sigma_y$ and $1.0\sigma_y$ for the position jitter and $0.1\sigma_{y'}$, $0.3\sigma_{y'}$, $0.5\sigma_{y'}$ and $1.0\sigma_{y'}$ for the angle jitter were considered. These different position and angle jitters induced a larger average bunch transverse position at wakefields sources, $\langle\Delta r\rangle$, and thus larger wakefield kicks $\Delta r'$, as seen in Eq. 3.1. The impact of an incoming angle jitter of $0.1\sigma_{y'}$ was first studied. The vertical IP beam size dependence on the beam intensity and the IP beam size distributions for $0.1 \times 10^{10} e^-$ and $1.0 \times 10^{10} e^-$ are shown in Fig. 3.19. The dashed line is the intensity-dependent parameter fit defined in Eq. 3.8. The results for an incoming $0.1\sigma_y$ beam position jitter are shown in Fig. 3.20. For each machine 200 consecutive pulses were tracked, reproducing the number of pulses the IPBSM needs to compute the beam size in ATF2. The error bars represent the standard error for 100 machines and 200 pulses per machine. As noted earlier, the wakefield kicks are linear with the beam intensity and the beam size at the IP has a quadratic dependence with the intensity of the deflecting kicks, thus, the beam size at the IP has a quadratic dependence with the beam intensity as seen in Fig. 3.19. A second order fit was introduced to compare the different cases and an intensity-dependent parameter w was defined as:

$$w = \sqrt{\frac{\sigma_y^{*2} - \sigma_{0y}^{*2}}{Q^2}} \quad (3.8)$$

with σ_y^* the vertical beam size at the IP, Q the beam intensity, and σ_{0y}^* the vertical beam size at the IP at zero beam intensity (i.e. considering no wakefield sources).

The ATF2 incoming beam position and angle jitter amplitudes are uncertain. In order to study the full spectrum of possibilities, the effects of amplitudes between

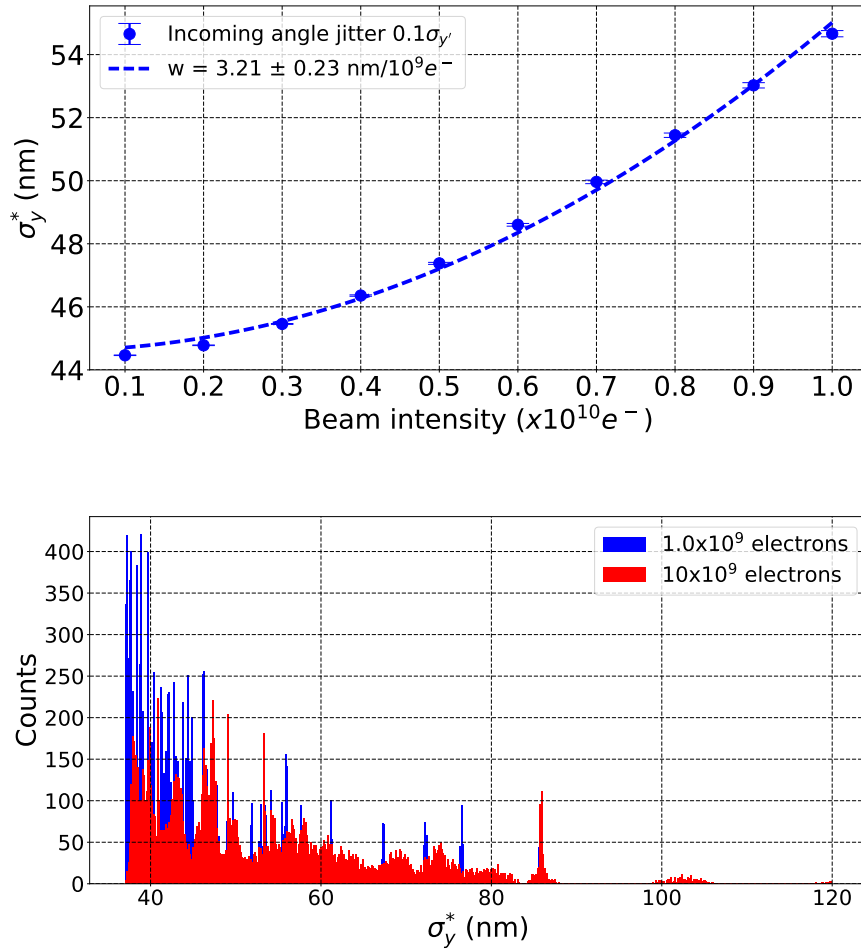


Figure 3.19: (Top) Effect of an incoming $0.1\sigma_{y'}$ beam angle jitter on the vertical beam size at the IP (σ_y^*) vs. the beam intensity; (Bottom) distributions of the vertical beam size at the IP (σ_y^*) for low and high beam intensities, calculated with PLACET in the presence of wakefields.

0.1 and $0.5\sigma_y$ for the position jitter and between 0.1 and $0.5\sigma_{y'}$ for the angle one were simulated. Figures 3.21 and 3.22 show, respectively, the impact of the position jitters and the angle jitters on the vertical beam size at the IP (σ_y^*). The error bars represent the standard error for 100 machines and 200 pulses per machine. One can conclude that the position jitter has a higher impact not just on the average beam sizes at each beam intensity, but also on the intensity-dependent parameter. Indeed, for an incoming position jitter of $0.5\sigma_y$, the intensity-dependent parameter is equal to $5.91 \pm 0.99 \text{ nm}/10^9 e^-$ compared to $3.33 \pm 0.25 \text{ nm}/10^9 e^-$ for an incoming angle jitter of $0.5\sigma_{y'}$.

In reality, the beam is injected with both position and angle jitters at the same

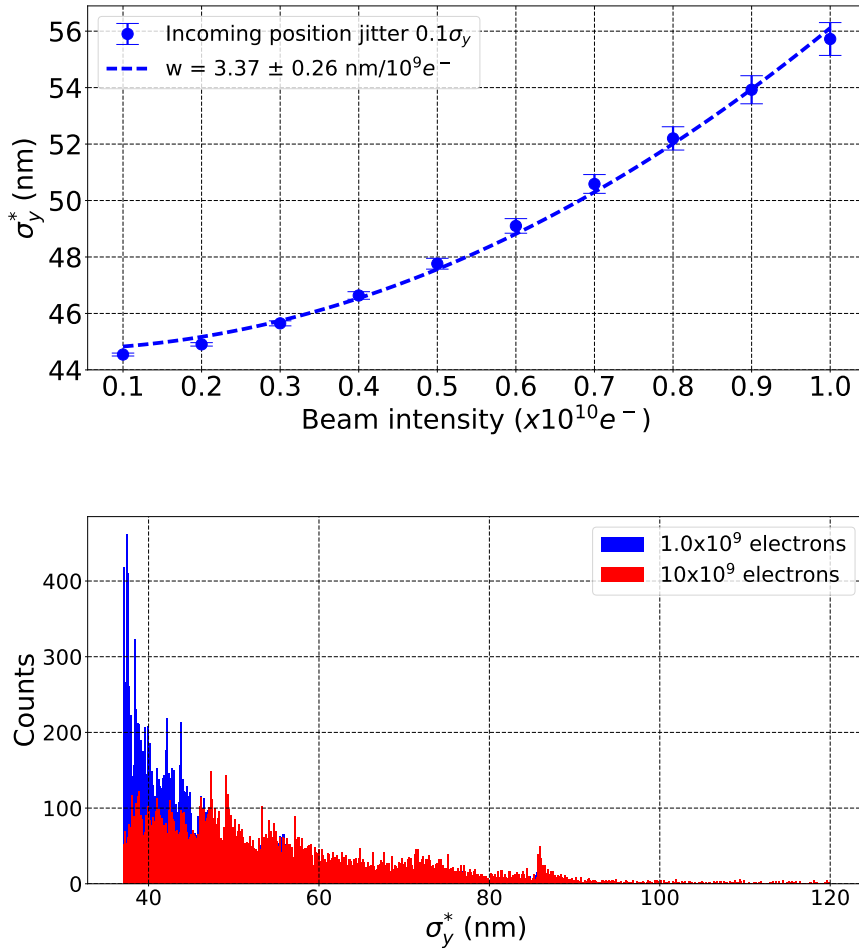


Figure 3.20: (Top) Effect of an incoming $0.1\sigma_y$ beam position jitter on the vertical beam size at the IP (σ_y^*) vs. the beam intensity; (Bottom) distributions of the vertical beam size at the IP (σ_y^*) for low and high beam intensities, calculated with PLACET in the presence of wakefields.

time. The effect of both jitters was studied considering the previous static imperfections and corrections but this time with position and angle jitter amplitudes from 0.1 to $1.0 \sigma_y$ and 0.1 to $1.0 \sigma_{y'}$ respectively. The impacts of such jitters on the vertical beam size at the IP are shown in Fig. 3.23. The error bars represent the standard error for 100 machines and 200 pulses per machine.

Only the impact of incoming vertical jitters was considered so far. In the real machine, the beam arrives with position and angle jitters in both the vertical and horizontal planes. The previous static imperfections and corrections were taken into account for these simulations. The beam was injected in the ATF2 extraction line with incoming horizontal position and angle jitters of respectively $0.3\sigma_x$ and $0.3\sigma_{x'}$

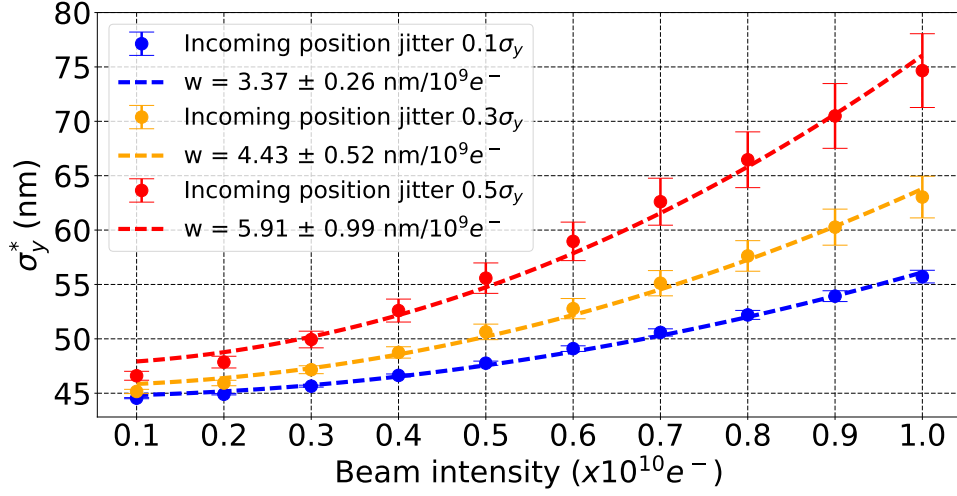


Figure 3.21: Effect of incoming 0.1, 0.3 and 0.5 σ_y beam position jitter on the vertical beam size at the IP (σ_y^*) vs. the beam intensity, calculated with PLACET in the presence of wakefields.

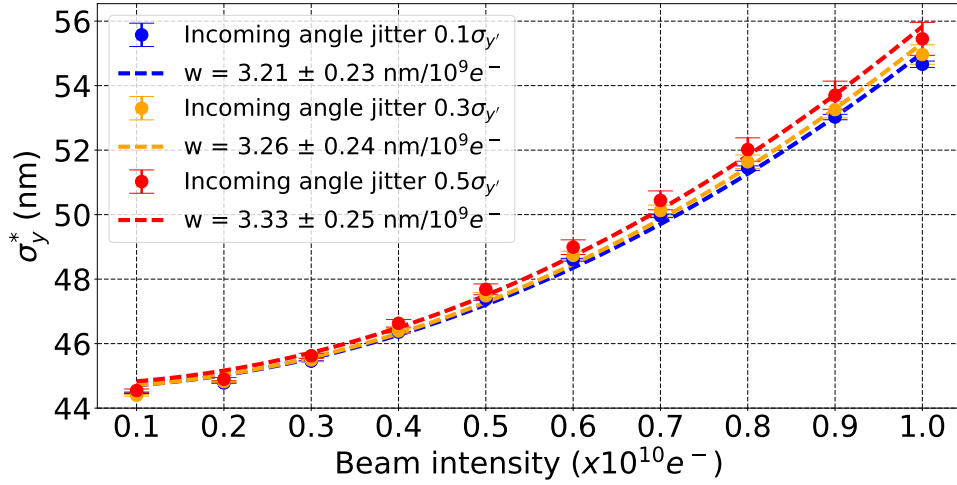


Figure 3.22: Effect of incoming 0.1, 0.3 and 0.5 $\sigma_{y'}$ beam angle jitter on the vertical beam size at the IP (σ_y^*) vs. the beam intensity, calculated with PLACET in the presence of wakefields.

and with incoming vertical position and angle jitters of respectively $0.3\sigma_y$ and $0.3\sigma_{y'}$. The resulting average vertical beam size at the IP (σ_y^*) vs. the beam intensity is shown in Fig. 3.24. The difference between the two cases is small, $w = 4.47 \pm 0.53 \text{ nm}/10^9$ for the case with jitters only in the vertical plane against $w = 4.60 \pm 0.57 \text{ nm}/10^9$ for the case with jitters in both planes. Thus, the impact of incoming horizontal jitters

on the vertical beam size at the IP is small in ATF2.

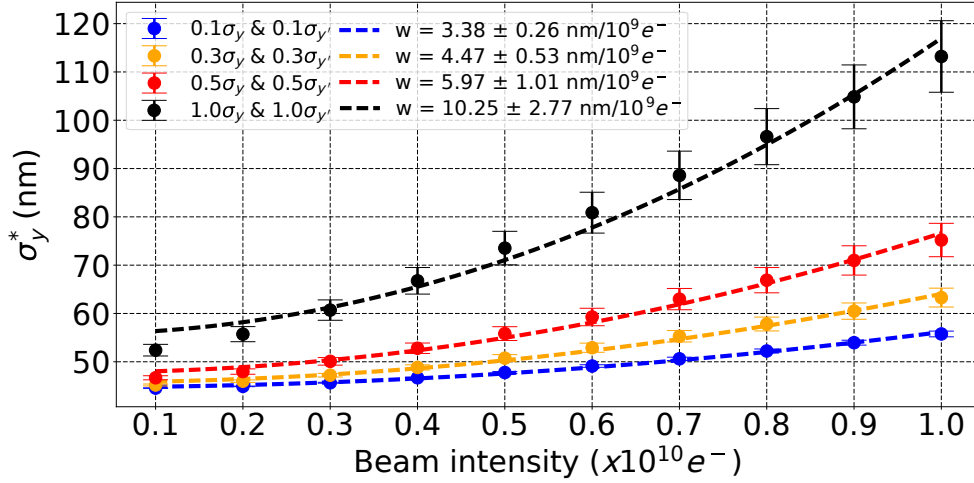


Figure 3.23: Effect of both incoming 0.1 , 0.3 , 0.5 and 1.0 σ_y beam position and 0.1 , 0.3 , 0.5 and 1.0 $\sigma_{y'}$ beam angle jitters on the vertical beam size at the IP (σ_y^*) vs. the beam intensity, calculated with PLACET in the presence of wakefields.

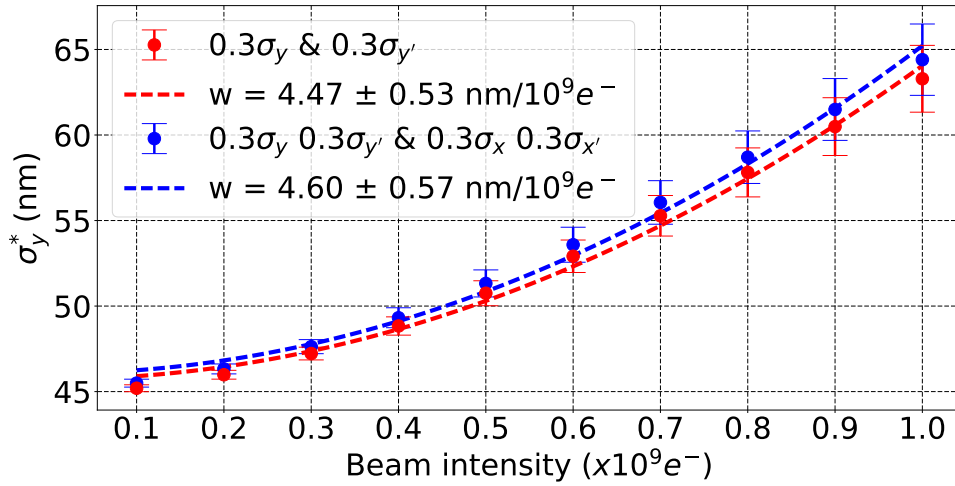


Figure 3.24: Effect of incoming horizontal position and angle jitters of respectively $0.3\sigma_x$ and $0.3\sigma_{x'}$ and incoming vertical position and angle jitters of respectively $0.3\sigma_y$ and $0.3\sigma_{y'}$ on the vertical beam size at the IP (σ_y^*) vs. the beam intensity, calculated with PLACET in the presence of wakefields.

Table 3.4: Impact of the incoming position and angle jitters separately at low and high beam intensities on the vertical beam size at the IP (σ_y^*) calculated with PLACET.

Jitter	w [nm/10⁹ e⁻]	Intensity [e⁻]	Average σ_y^* [nm]
Inc. position jitter $0.1\sigma_y$	3.37 ± 0.26	1.0×10^9	45 ± 0.05
		10.0×10^9	56 ± 0.58
Inc. angle jitter $0.1\sigma_{y'}$	3.21 ± 0.23	1.0×10^9	44 ± 0.03
		10.0×10^9	55 ± 0.10
Inc. position jitter $0.3\sigma_y$	4.43 ± 0.52	1.0×10^9	45 ± 0.20
		10.0×10^9	63 ± 1.92
Inc. angle jitter $0.3\sigma_{y'}$	3.26 ± 0.24	1.0×10^9	45 ± 0.05
		10.0×10^9	55 ± 0.30
Inc. position jitter $0.5\sigma_y$	5.91 ± 0.99	1.0×10^9	47 ± 0.41
		10.0×10^9	75 ± 3.39
Inc. angle jitter $0.5\sigma_{y'}$	3.33 ± 0.25	1.0×10^9	45 ± 0.08
		10.0×10^9	55 ± 0.51

Table 3.5: Impact of the incoming position and angle jitters simultaneously at low and high beam intensities on the vertical beam size at the IP (σ_y^*) calculated with PLACET.

Jitter	w [nm/10⁹ e⁻]	Intensity [e⁻]	Average σ_y^* [nm]
Inc. pos. jitter $0.1\sigma_y$ and ang. jitter $0.1\sigma_{y'}$	3.38 ± 0.26	1.0×10^9	45 ± 0.05
		10.0×10^9	56 ± 0.59
Inc. pos. jitter $0.3\sigma_y$ and ang. jitter $0.3\sigma_{y'}$	4.47 ± 0.53	1.0×10^9	45 ± 0.20
		10.0×10^9	63 ± 1.95
Inc. pos. jit. $0.3\sigma_x$ & $0.3\sigma_y$ and ang. jit. $0.3\sigma_{x'}$ & $0.3\sigma_{y'}$	4.60 ± 0.57	1.0×10^9	45 ± 0.23
		10.0×10^9	64 ± 2.09
Inc. pos. jitter $0.5\sigma_y$ and ang. jitter $0.5\sigma_{y'}$	5.97 ± 1.01	1.0×10^9	47 ± 0.42
		10.0×10^9	75 ± 3.45
Inc. pos. jitter $1.0\sigma_y$ and ang. jitter $1.0\sigma_{y'}$	10.25 ± 2.77	1.0×10^9	52 ± 1.20
		10.0×10^9	113 ± 7.41

Table 3.6: Summary of the impact of the static and dynamic errors on the vertical IP beam size at low/high intensity in presence of wakefields calculated with PLACET.

Static error	Misalignment	Strength error	Roll error
Error amplitude	100 [μm]	1×10^{-4}	200 [μrad]
σ_y^* growth at $10^9 e^-$	16%	4%	6%
σ_y^* growth at $10^{10} e^-$	22%	15%	12%
Dynamic error	Angle jitter	Position jitter	Both jitters
Error amplitude	$0.5\sigma_{y'}$	$0.5\sigma_y$	$0.5\sigma_y$ and $0.5\sigma_{y'}$
σ_y^* growth at $10^9 e^-$	22%	27%	27%
σ_y^* growth at $10^{10} e^-$	49%	103%	103%

Table 3.4 and Table 3.5 summarise respectively the impact of the angle and position jitters, separately at low and high intensity on the vertical beam size at the IP, and the impact of the angle and position jitters simultaneously at low and high intensity on the vertical beam size at the IP. Table 3.6 summarize the impact of the statics and dynamic effects on the vertical beam size at the IP (σ_y^*) in function of the beam intensity with wakefields calculated with PLACET.

In conclusion, static and dynamic errors have a significant impact on the vertical beam size at the IP at high intensities, in the presence of wakefields. However dynamic errors have a larger impact on the beam size. An initial position jitter of $0.5\sigma_y$ leads to increase of the average vertical beam size at the IP of 27% and 103% at respectively $0.1 \times 10^{10} e^-$ and $1.0 \times 10^{10} e^-$. One can observe that when both jitters are taken into account the impact of the incoming angle jitter is negligible. This is due to the phase advance between the extraction kicker and the IP. Indeed, the impact of a kick at a certain position translates into a position offset at the IP if the phase advance is $(n+1/2)\pi$ between those two points. The vertical phase advance between the extraction kicker and the IP is 8π , thus the incoming angle offset translates into an angle offset at the IP, making negligible its impact on the vertical beam size.

3.5 Wakefield knobs

In order to reduce the beam size growth due to wakefields, a system of wakefield knobs was installed and tested in the beamline between BPMs MQD10AFF and MQF9AFF (see Fig. 3.3). It consists of two C-BPMs on one mover and a bellows on a second

mover as shown in Fig. 3.25. The idea is to scan the positions of these sources independently. The performed 2D scan permits one to find the best position of each mover that corrects the wakefield kicks generated by the previously studied wakefield sources. The correction consists of creating a compensating wakefield kick of opposite sign to the one generated by the beam line elements. The system was installed at $s=61.6$ m, in a high- β region to maximize the impact as shown in Fig. 2.1 and the phase advance between the position of the system and the IP is 2.5π as shown in Fig. 2.5. This means that a wakefield kick at the position of the system will translate into a position offset at the IP. The impact of this system was simulated with PLACET. The following simulation conditions were used: misalignment of quadrupoles, C-BPMs and sextupoles of $100 \mu\text{m}$ RMS for 100 random seeds and One-to-one, DFS and first order knobs at the IP. The position of each mover is scanned from $-3000 \mu\text{m}$ to $3000 \mu\text{m}$ with 20 steps. Figures 3.26 and 3.27 show the impact of the position scans of the bellows and the C-BPM respectively on the vertical IP beam size (σ_y^*) in one machine considering the other mover at zero. A 2D scan of the positions of the two sources leads to a minimum beam size of 37 nm shown in Fig. 3.28. This correction was tested with beam intensities from $0.1 \times 10^{10} e^-$ to $1.0 \times 10^{10} e^-$. The impact of the wakefield knobs and how it scales with the beam intensity is shown in Fig. 3.29. The error bars represent the standard error for 100 machines and 200 pulses per machine. The correction is effective, decreasing the average vertical beam size at the IP ($\overline{\sigma_y^*}$) for 100 machines from more than 61 nm to around 45 nm . As one can expect, the impact of the mover with 2 C-BPMs is larger than the one with the bellows as shown in Table 3.7. Thanks to the wakefield knobs, a vertical beam size at the IP of 37 nm was obtained for 16 machines at $1.0 \times 10^{10} e^-$. An histogram of the impact of the wakefield knobs on the vertical beam size at the IP at $1.0 \times 10^{10} e^-$ is shown in Fig. 3.30.

Table 3.7: Impact of the wakefield knobs on the average vertical beam size at the IP for 100 machines in the presence of wakefields calculated with PLACET.

Case	$\overline{\sigma_y^*}$ [nm]
No source on movers	61.2 ± 1.4
Bellows on mover	48.4 ± 1.0
2 C-BPMS on mover	45.5 ± 0.9
Both the bellows and the 2 C-BPMs on movers	45.2 ± 0.9

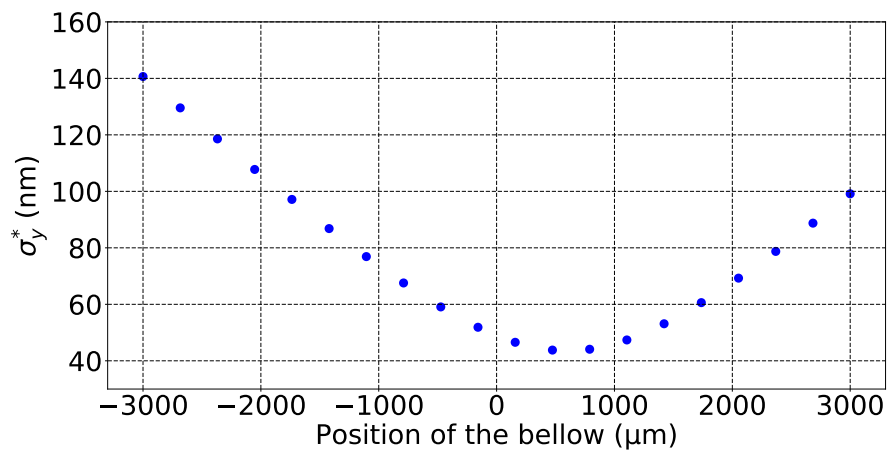
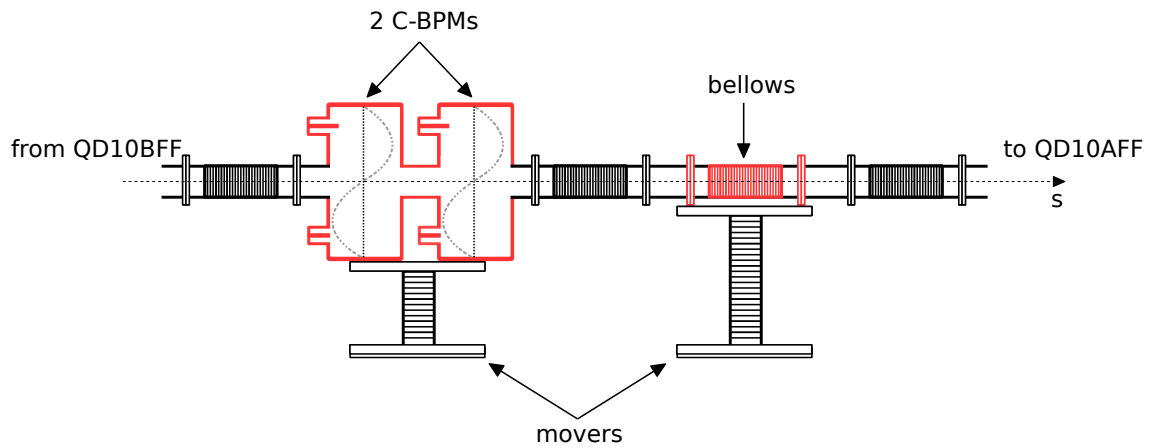


Figure 3.26: Vertical beam size at the IP σ_y^* vs. the position of the bellows, for one machine, calculated with PLACET in the presence of wakefields.

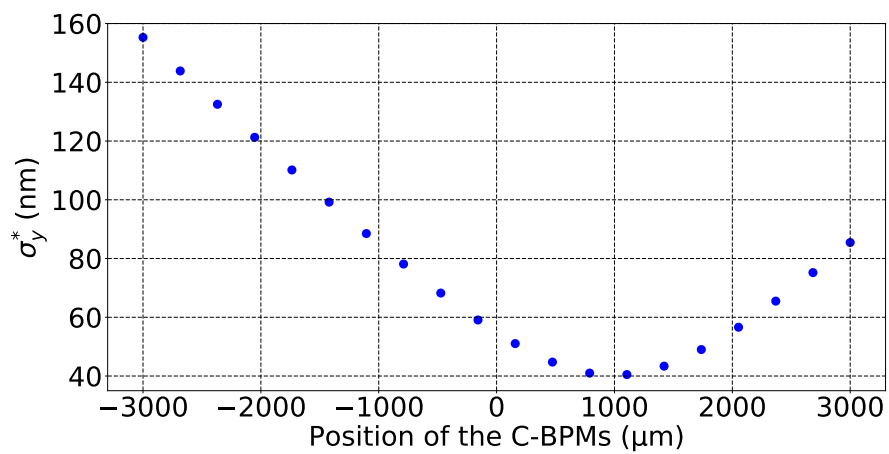


Figure 3.27: Vertical beam size at the IP σ_y^* vs. the position of the bellows, for one machine, calculated with PLACET in the presence of wakefields.

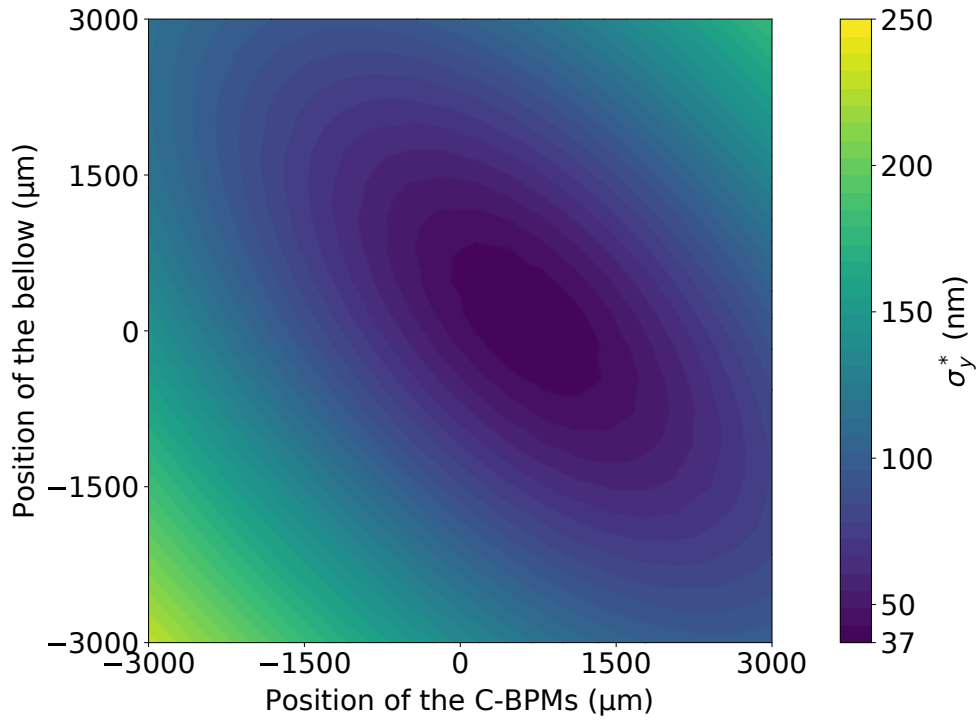


Figure 3.28: Contour plot of the simulation of the impact of the position of the C-BPMs and the bellows on the vertical beam size at the IP σ_y^* , for one machine, calculated with PLACET in the presence of wakefields.

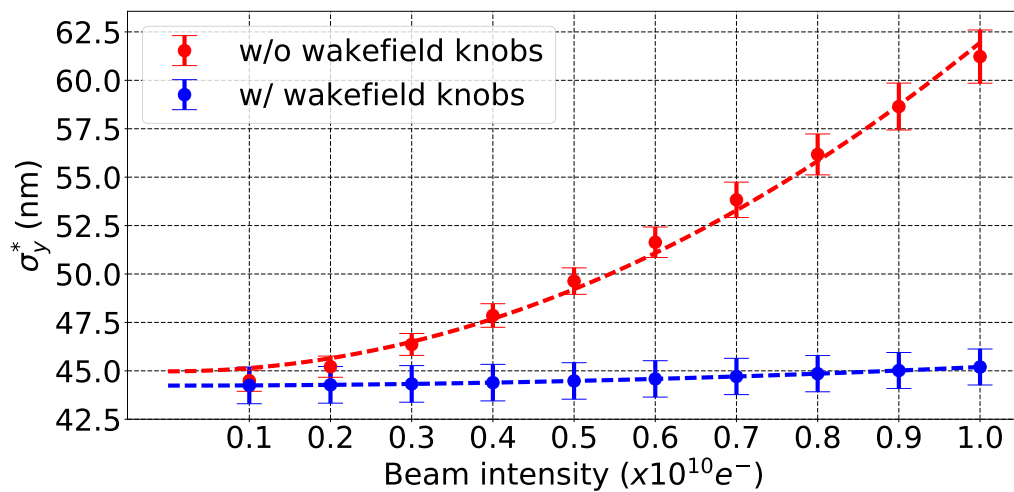


Figure 3.29: Vertical beam size at the IP σ_y^* vs. the beam intensity, for 100 machines with ATF2 wakefield knobs, calculated with PLACET in the presence of wakefields.

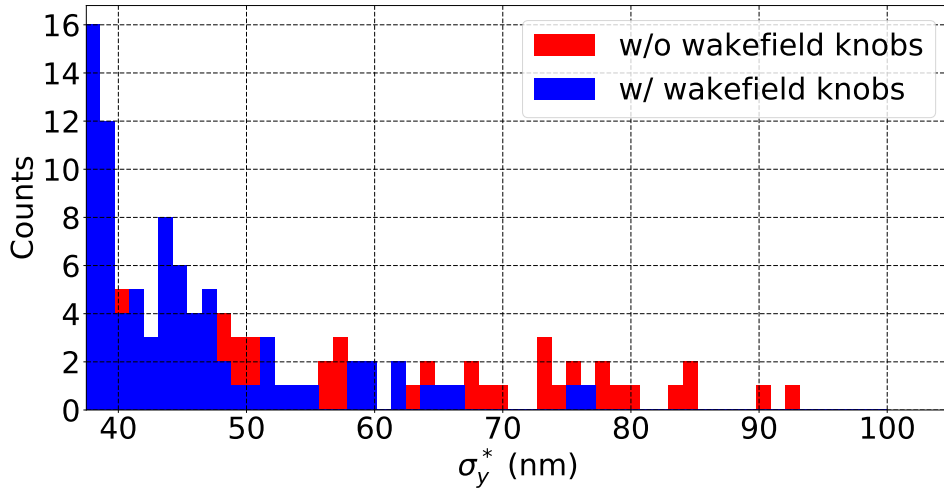


Figure 3.30: Histogram of the vertical beam size at the IP with and without wakefield knobs, calculated with PLACET in the presence of wakefields.

3.6 Bunch length impact on the beam intensity.

For all the previous ATF2 simulations, a 7 mm long bunch was considered. However, bunch length measurements showed that the bunch length, σ_z , depends on the beam intensity. As will be discussed in section 4.1, σ_z varies from 6.2 mm at $0.1 \times 10^{10} e^-$ to 8.5 mm at $0.8 \times 10^{10} e^-$. In order to show the impact of the bunch length on the intensity-dependent effects, the following simulation conditions were considered: quadrupoles, C-BPMs and sextupoles have a misalignment of 100 μm RMS and a roll error of 200 μrad RMS and the strength error of quadrupoles and sextupoles is 10^{-4} RMS. In this case again, One-to-one, DFS, WFS corrections and IP knobs are applied on each machine. This is done for 100 machines and 200 pulses per machine considering an incoming position jitter of $0.3\sigma_y$. The impact of taking into account the correlation between the bunch length (σ_z) and the beam intensity is shown in Fig. 3.31. The error bars represent the standard error for 100 machines and 200 pulses per machine. As shown in section 4.1, the bunch length was measured for intensities between $0.1 \times 10^{10} e^-$ and $0.8 \times 10^{10} e^-$. The dashed line is the intensity-dependent parameter fit defined in Eq. 3.8. The average vertical beam size at the IP is smaller for a beam with a correlated bunch length at low intensity, $0.1 \times 10^{10} e^-$, since the bunch length is smaller than 7 mm. However, at high intensity, $1.0 \times 10^{10} e^-$, since the bunch is longer than 7 mm, the wakefield kick is larger, and thus the beam size at the IP is 3 nm larger as shown in Fig. 3.32, which is not negligible. The error

bars represent the standard error for 100 machines and 200 pulses per machine. The results are summarized in Table 3.8.

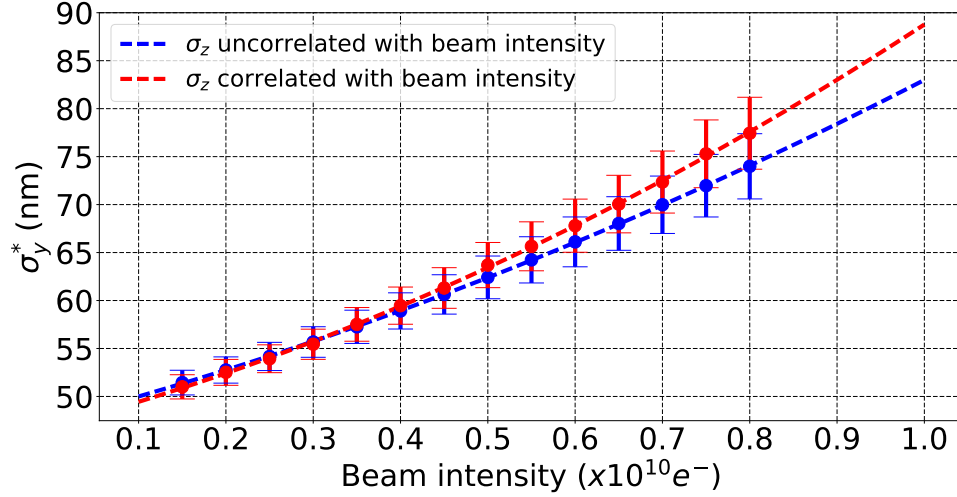


Figure 3.31: Simulations of the impact of the ATF2 bunch length (σ_z) on the vertical IP beam size (σ_y^*) vs. the beam intensity, calculated with PLACET in the presence of wakefields.

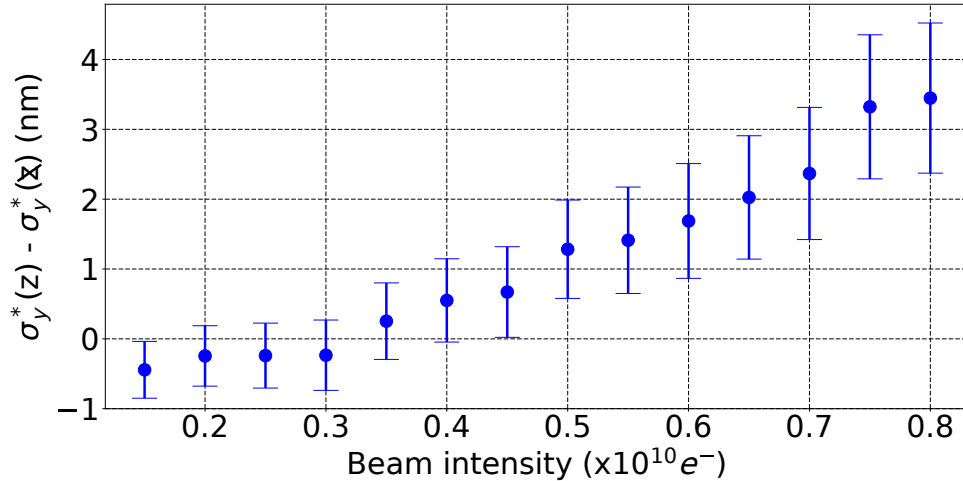


Figure 3.32: Difference between the vertical IP beam size (σ_y^*) considering the bunch length (σ_z) is correlated and the vertical IP beam size (σ_y^*) considering the bunch length (σ_z) is not correlated with the beam intensity, calculated with PLACET in the presence of wakefields.

Table 3.8: Impact of the wakefield knobs on the average vertical beam size at the IP for 100 machines in the presence of wakefields calculated with PLACET.

Case	Beam intensity	$\overline{\sigma}_y^*$ [nm]
σ_z is uncorrelated with the beam intensity	$0.1 \times 10^{10} e^-$	51.4 ± 1.3
σ_z is correlated with the beam intensity	$0.1 \times 10^{10} e^-$	51.0 ± 1.3
σ_z is uncorrelated with the beam intensity	$1.0 \times 10^{10} e^-$	74.0 ± 3.4
σ_z is correlated with the beam intensity	$1.0 \times 10^{10} e^-$	77.4 ± 3.7

3.7 Conclusion

The static and dynamic imperfections were studied with PLACET and the ATF2 target value of 37 nm seems hard to obtain with realistic conditions at $1.0 \times 10^{10} e^-$ with the One-to-one, DFS, WFS corrections and the IP knobs. However, they decrease the average vertical beam size drastically. Indeed, without applying any corrections, the average vertical beam size at the IP for 100 machines with static imperfections is $13.8 \pm 86.2 \mu$. However, in order to mitigate those effects, correction techniques were implemented and tested, showing good results. One-to-one correction decreased the average vertical beam size at the IP for 100 machines to 1220 ± 337 nm. DFS and WFS corrections squeezed the beam to 904 ± 145 nm. Then, the IP knobs reduced the beam size to 58.4 ± 4.7 nm.

An average IP vertical beam size of 45.2 ± 0.9 was obtained with static imperfections and after applying the One-to-one, DFS, WFS corrections, IP knobs and wakefield knobs. Thanks to the wakefield knobs, the ATF2 goal 1 was achieved for 16 machines at the nominal beam intensity of $1.0 \times 10^{10} e^-/\text{bunch}$. This correction is really promising for future ATF2 beam tuning operations.

These corrections were tested experimentally in the ATF2 machine and are described in the next chapter.

Chapter 4

Intensity-dependent effects in ATF2, measurements

In order to measure the intensity-dependent effects and to compare them with simulations, different sets of measurements were done in the ATF2 beam line with the help of local scientists.

4.1 Impact of the intensity on the bunch length

The bunch length was obtained by using a streak camera to measure the time structure of the synchrotron radiation from one of the bending magnets in the arcs of the ATF2 damping ring [20, 57]. Light emitted by synchrotron radiation in the ATF2 damping ring passes through a system of 3 mirrors and 2 lenses before arriving at the streak camera as shown in Fig. 4.1. The source point is located 270 mm downstream of the entrance edge of a bending magnet at the end of the west arc of the damping ring. The first mirror, made of aluminum-coated copper, reflects the synchrotron radiation light by 90° upward. The light is then reflected by a second mirror and focused by passing through the first lens. Then, it is reflected by a third mirror and passes through the second lens to focus the light before it arrives at the streak camera. The second lens has a rotating filter which can be used to reduce or increase the intensity of the light received by the streak camera.

In order to measure the bunch length, the shutter of the camera and the gain were setup and remained constant for the rest of the measurement. The chosen parameters were 20 ms for the shutter and 27 for the gain. The amount of light arriving at the camera, also called “area”, was kept constant using the filtered lens. An example of an observed streak image is shown in Fig. 4.2. The bunch length was measured for 15 beam intensities, ranging from $0.1 \times 10^{10} e^-$ to $0.8 \times 10^{10} e^-$. The measurements were

repeated on two separate days. The estimated bunch length, average of 10 bunches per beam intensity, is shown in Fig. 4.3. The error bars represent the standard error for 10 consecutive bunch length measurements for each beam intensity.

The conclusion is that the bunch length, σ_z , varies from 6.2 mm at $0.1 \times 10^{10} e^-$ to 8.5 mm at $0.8 \times 10^{10} e^-$. This result matches measurements from 2004 [27] and the model established in 2001 [58] for calculation of the intra-beam scattering effects in the ATF damping ring.

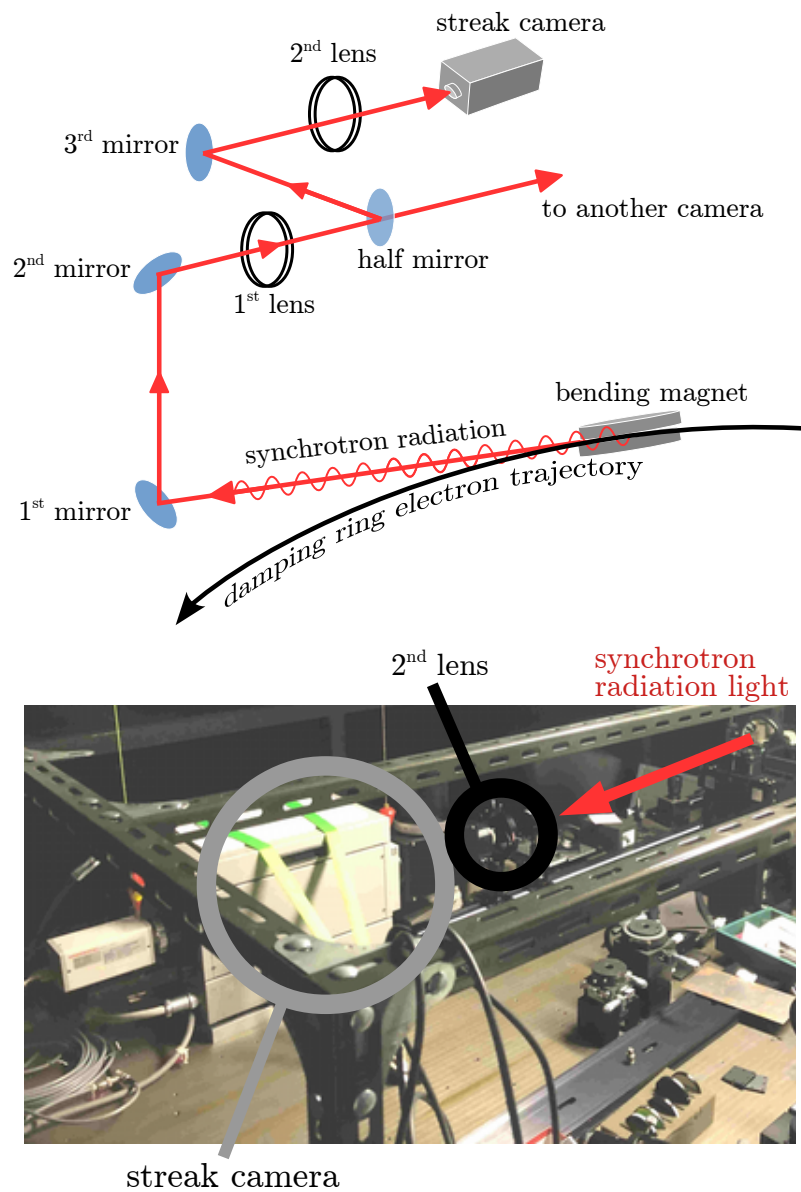


Figure 4.1: Schematic of the bunch length measurement setup (top), picture of the bunch length measurement system (bottom).

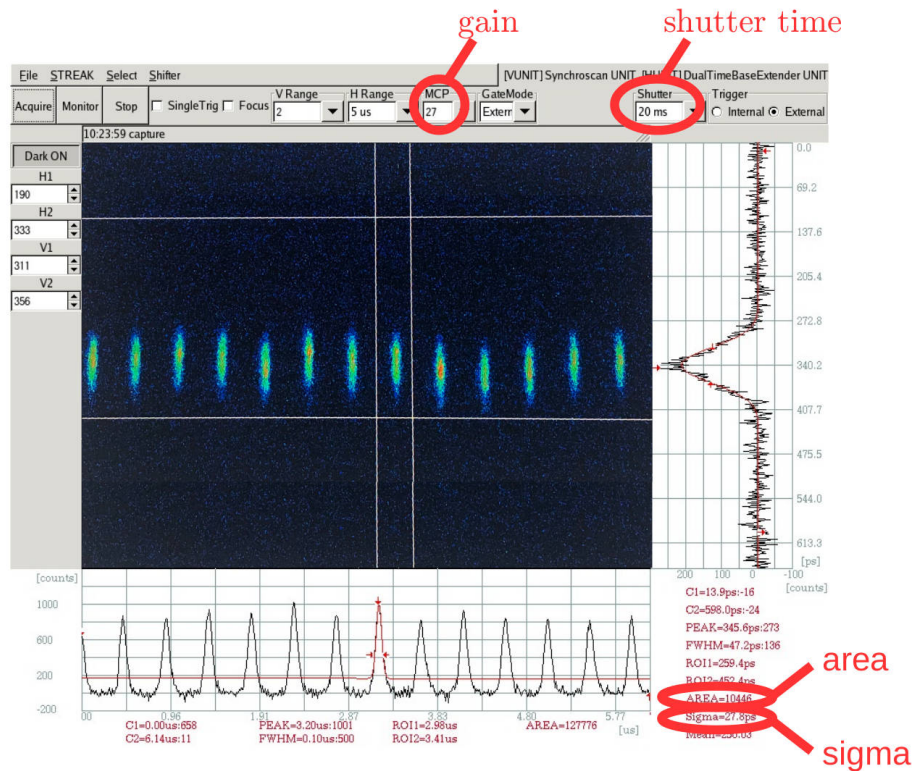


Figure 4.2: Screenshot of the software used for the ATF2 bunch length measurement. The gain, shutter time and area parameters are shown for the measurement. The longitudinal profile of consecutive bunches is shown at the bottom of the figure. The bunch length, sigma is in ps.

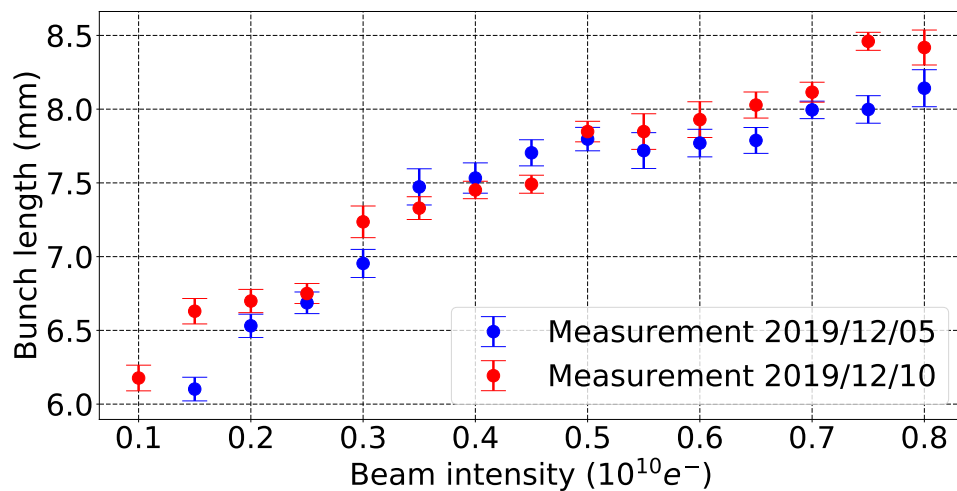


Figure 4.3: Bunch length measurement vs. beam intensity measured on two separate days.

4.2 Machine and beam instabilities

ATF2 is a test facility and is suffers from different types of instabilities and drifts such as slow orbit drifts, beam intensity and beam energy drifts.

4.2.1 Slow Beam orbit drift

The orbit drift, With a period of a few hours, makes the beam unstable and the beamline needs to be re-tuned regularly. Figure 4.4 shows the vertical orbit at 2 selected BPMs over a few hours. The orbit drift varies from a few μm to a few tenths of μm . The vertical orbit spread is due to the beam orbit jitter.

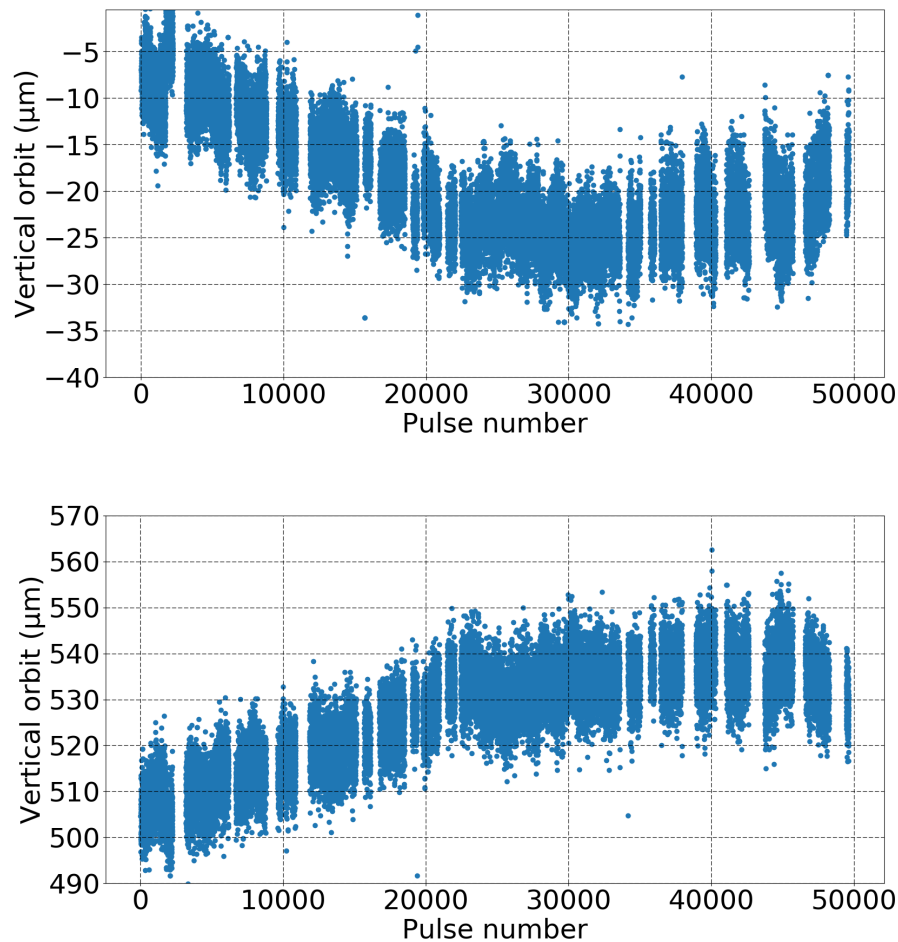


Figure 4.4: Vertical orbit at 2 selected BPMs: QD10AFF and QF9AFF. 50000 pulses travel in ATF2 in 4h27.

4.2.2 Beam intensity drift

As shown in Fig. 4.5, the beam intensity can drift by $2.0 \times 10^9 e^-$ in a few hours. One reason for this drift is the temperature drift during the day for the long period oscillations and the temperature of the damping ring for the short period oscillations. Figure 4.6 shows the correlation between the variation of the beam intensity and the air temperature inside the damping ring.

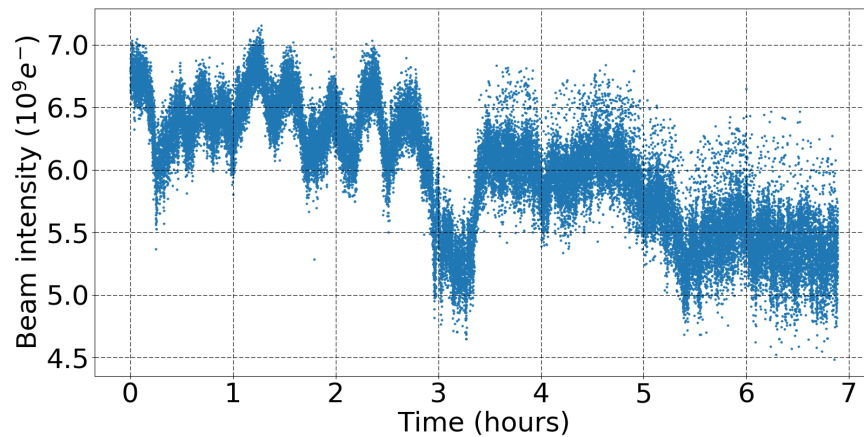


Figure 4.5: ATF2 beam intensity drift, measured by the Integrated Current Transformer located near the IP.

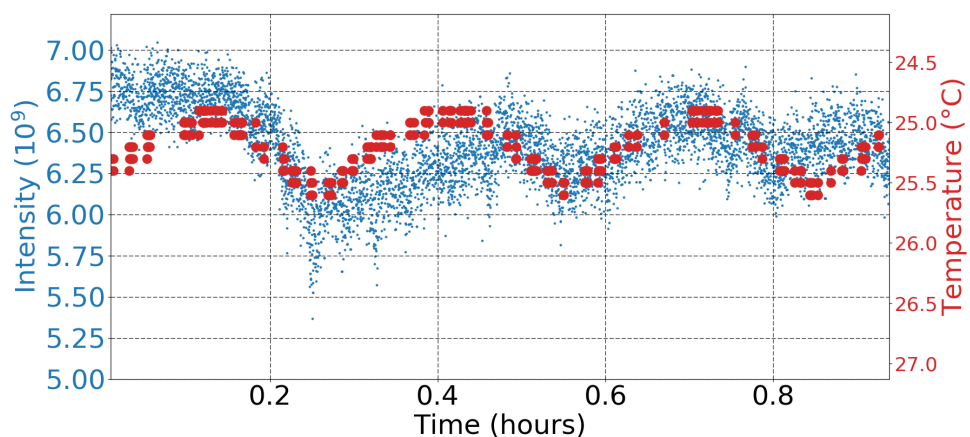


Figure 4.6: ATF2 beam intensity (left-hand side), measured by the Integrated Current Transformer located near the IP and the air temperature in the damping ring (right-hand side).

4.2.3 Dispersion drift

The dispersion drift is due to the fluctuation of the beam energy coupled with the kick of the extraction kicker. The vertical dispersion (η_y) was measured four times. One can observe in Fig. 4.7 that the vertical dispersion drifts away from its target value of zero. After 6:30 hours, close to the IP, the vertical dispersion drifted by 38 mm.

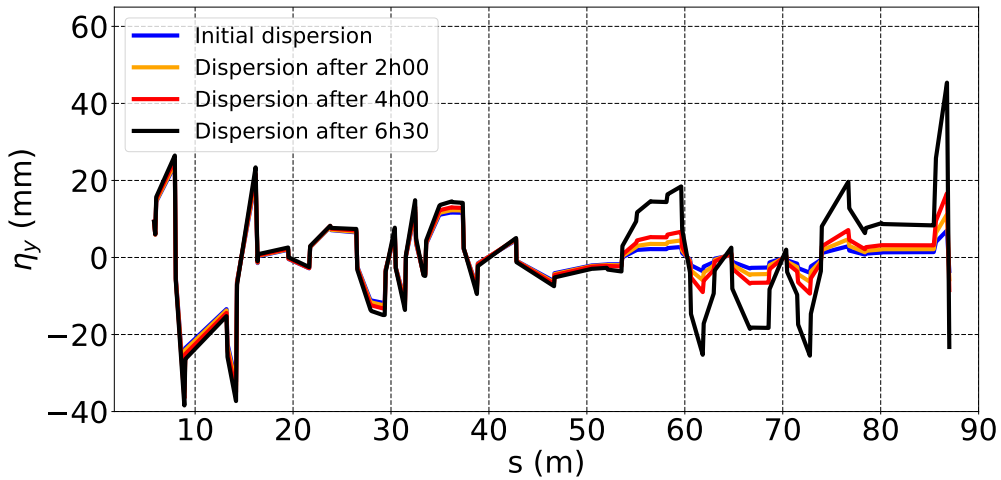


Figure 4.7: Vertical dispersion (η_y) vs s (m) measured at four different times.

4.3 Measurement of the incoming position and angle jitters

As explained in Sec. 2.2.3, 3 BPMs are localized in the ATF2 upstream area: P1, P2 and P3. They were used to measure the vertical and horizontal beam positions with a resolution of 157 ± 8 nm at $0.82 \times 10^{10} e^-$ [59]. In November 2018, the upstream beam position and angle jitters were measured. The vertical position was measured for 400 consecutive pulses each for beam intensities in the range $0.11 \times 10^{10} e^-$ to $0.79 \times 10^{10} e^-$. shown in Fig. 4.8. The position resolution of those three stripline BPMs is better with a higher beam intensity [42]. This behavior explains the fact that the correlation between the measured jitter and the beam intensity is decreasing with the beam intensity. The measured upstream vertical position jitter at $0.79 \times 10^{10} e^-$ is $0.9 \mu\text{m}$ at P1, $1.4 \mu\text{m}$ at P2 and $0.8 \mu\text{m}$ at P3.

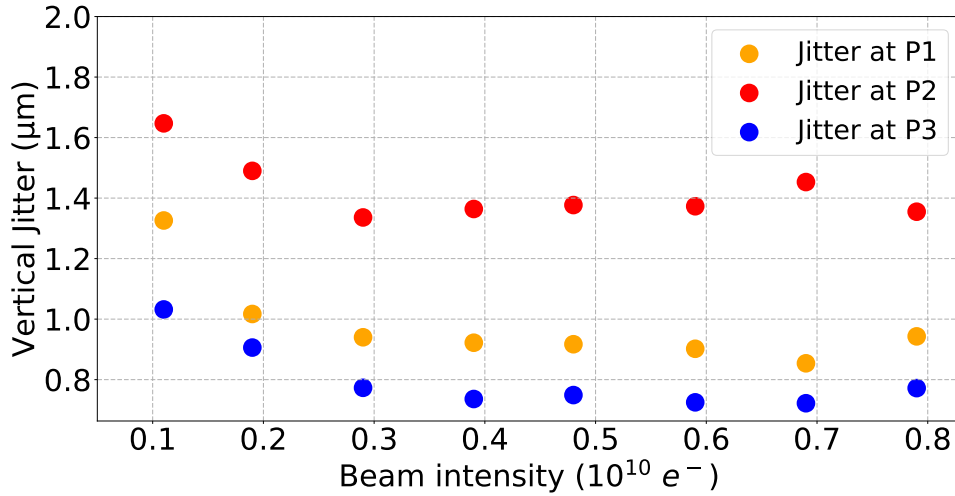


Figure 4.8: Vertical position beam jitters at upstream BPMs P1, P2 and P3 vs. beam intensity.

In order to extrapolate the incoming jitter to other locations in ATF2, the orbit was calculated using transfer matrices. Let the initial beam have a vertical position jitter of y_0 , an initial angle jitter of y'_0 and an initial energy jitter of δ_0 . If the vertical position jitter, angle jitter and energy jitter at the BPM P3 are noted y_{P3} , y'_{P3} and δ_{P3} . Then the relationship between y_0 and y_{P3} is given by:

$$\begin{pmatrix} y_{P3} \\ y'_{P3} \\ \delta_{P3} \end{pmatrix} = R_{0 \rightarrow P3} \begin{pmatrix} y_0 \\ y'_0 \\ \delta_0 \end{pmatrix} \quad (4.1)$$

with $R_{0 \rightarrow P3}$ the transfer matrix between the extraction of the damping ring and BPM P3. y_0 and y'_0 are obtained simply by inverting the $R_{0 \rightarrow P3}$ matrix. The position and angle jitters measured at P3 were $0.84 \mu\text{m}$ and $1.07 \mu\text{rad}$ respectively, and hence the calculated incoming vertical position jitter using the transfer matrix from the model is $1.3 \mu\text{m}$ and μrad respectively.

The measured beam position at one of the first calibrated ATF2 striplines, MQF3X ($s=10.2 \text{ m}$) is shown in Fig. 4.9. This measurement was done at $0.65 \times 10^{10} e^-$. The measured vertical jitter at this BPM was extrapolated to the jitter at the extraction kicker and an incoming vertical jitter of $11.3 \mu\text{m}$ for 1000 consecutive pulses was calculated.

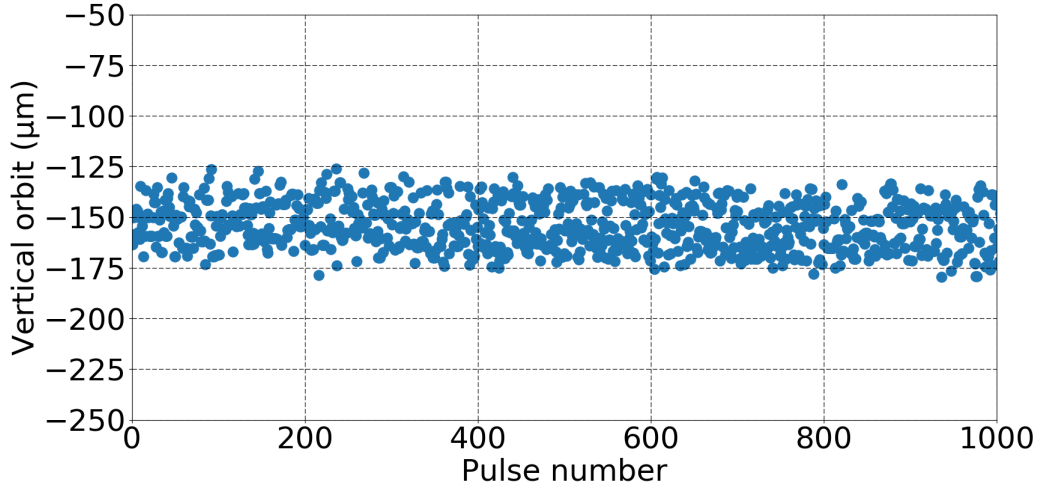


Figure 4.9: Vertical position beam position at upstream stripline BPM MQF3X.

An incoming vertical position jitter of $6 \mu\text{m}$ was considered in the simulations, average of the jitter measured by the FONT BPM and by the stripline. This corresponding to $1.0 \times \sigma_y$, with σ_y the vertical beam size at the extraction kicker if one considers the nominal incoming Twiss parameters. A similar amplitude was considered for the incoming angle jitter, $1.0 \times \sigma_{y'}$, with $\sigma_{y'}$ the vertical beam divergence at the extraction kicker.

However, as stated earlier, striplines and C-BPM resolutions are strongly linked to the beam intensity as explain in the next section.

4.4 Impact of the intensity on the BPM resolution

ATF2 employs two types of BPMs to measure the beam orbit: striplines and C-BPMs. In general, C-BPMs have a better resolution than the striplines. In order to calculate the resolution of each BPM, one can use the Model Independent Analysis [60]. The purpose is to remove the correlations between all BPM measurements. The correlation coefficients can be calculated as follows:

$$\begin{pmatrix} d_{1k} \\ d_{2k} \\ \vdots \\ d_{Mk} \end{pmatrix} = \begin{pmatrix} d_{1,1} & d_{1,2} & \cdots & d_{1,N-1} \\ d_{2,1} & d_{2,2} & \cdots & d_{2,N-1} \\ \vdots & \vdots & & \vdots \\ d_{M,1} & d_{M,2} & \cdots & d_{M,N-1} \end{pmatrix} \cdot \begin{pmatrix} v_1 \\ v_2 \\ \vdots \\ v_{N-1} \end{pmatrix} \quad (4.2)$$

$$\vec{d}_k = D_k \cdot \vec{v}_k \quad (4.3)$$

With d_{ik} the measured beam orbit in BPM k for machine pulse i , M the number of machine pulses, N the number of BPMs and v_j the correlation coefficients between BPMs and the one of interest, k . $N - 1$ BPMs are considered for D_k and \vec{v}_k since the orbit of BPM k is removed for the resolution calculation [60]. For a vertical angle jitter of $0.8 \mu\text{m}$ at P3, \vec{v} can then be computed using:

$$\vec{v}_k = D_k^{-1} \cdot \vec{d}_k \quad (4.4)$$

One defines \vec{R}_k the position residuals vector as:

$$\vec{R}_k = \vec{d}_k - D_k \cdot \vec{v}_k \quad (4.5)$$

Finally, the resolution of BPM k , σ_k , is as follows:

$$\sigma_k = \sqrt{\frac{\sum_i^M R_{ki}^2}{M}} \quad (4.6)$$

This resolution depends on the beam intensity q . It can be characterized by:

$$\sigma = \sqrt{\frac{A}{q^2} + B^2} \quad (4.7)$$

with A an amplitude and B a constant error associated with mechanical motion and electronics noise [61]. Figure 4.10 shows, for one of the cavity BPM, MQD4AFF, the vertical resolution and how it evolves with the beam intensity. The calculated vertical resolution is around 350 nm at low beam intensity ($0.1 \times 10^{10} e^-$) and 68 nm at a higher beam intensity ($0.47 \times 10^{10} e^-$). This is the best BPM in the beamline. This resolution calculation can also be used to find if there is any problem with BPMs along the line. Figure 4.11 shows the resolution of BPMs along the line. One can easily see where are the stripline BPMs. They have a poorer resolution (few microns) than cavity BPMs (tens of nanometers). Striplines are located from $s=0 \text{ m}$ to $s=25$, at $s=31.7 \text{ m}$ and $s=32.7$. C-BPMs are located at $s=27.7 \text{ m}$, $s=29.2 \text{ m}$ and $s=30.6 \text{ m}$ and from $s=34.8 \text{ m}$ to the end of the line.

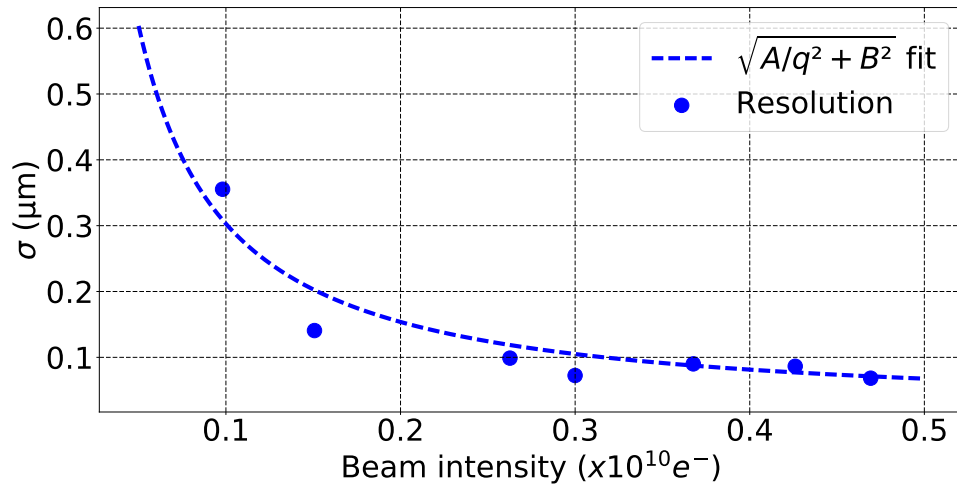


Figure 4.10: Vertical resolution vs. beam intensity for BPM MQD4AFF, a cavity BPM.

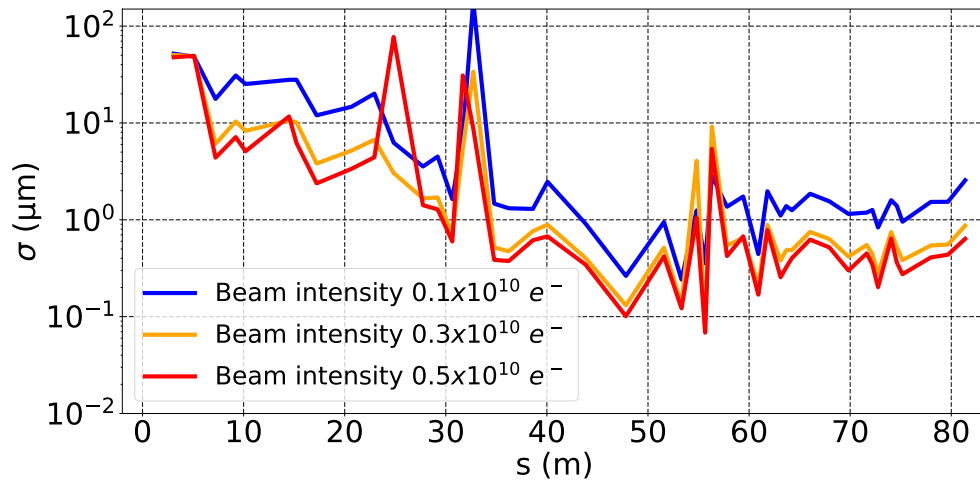


Figure 4.11: BPM vertical resolutions along the beamline.

However, the measured beam orbit is correlated with the beam intensity. In order to quantify this correlation, a mathematical factorisation was used and is explained in the next section.

4.5 Impact of the intensity on the beam orbit

4.5.1 Correlation between beam orbit and beam intensity using the Singular Value Decomposition (SVD)

The Singular Value Decomposition (SVD) is a method of factorisation of a rectangular matrix [60, 62, 63]. Given D , a $N \times M$ matrix, then the singular value decomposition of D exists and is a factorization of the form:

$$D = USV^T \quad (4.8)$$

where:

U is a $M \times M$ orthogonal matrix,

S is a $M \times N$ diagonal matrix with non-negative real numbers on the diagonal, and

V^t is a transpose of a $N \times N$ orthogonal matrix.

The diagonal values of S are the singular values, noted S_n . They are sorted from the highest to the smallest and they represents how strong are the correlations between the data in D . A typical way to use SVD on the orbit is to store in the D matrix the information as follows:

$$D = \begin{pmatrix} d_{1,1} & d_{1,2} & \cdots & d_{1,N} \\ d_{2,1} & d_{2,2} & \cdots & d_{2,N} \\ \vdots & \vdots & \ddots & \vdots \\ d_{M,1} & d_{M,2} & \cdots & d_{M,N} \end{pmatrix} \quad (4.9)$$

where:

d_{ik} is the measured displacement in BPM k for machine pulse i ,

M is the number of pulses, and

N is the number of BPMs.

The SVD of D gives information about correlations between the spatial parameter, the beam position at BPMs, and the temporal parameter, the pulses. In order to see the correlations between the beam position at BPMs and the beam intensity or between consecutive pulses and the beam intensity, one can add the beam intensity information in the last column of the D_q matrix as:

$$D_q = \begin{pmatrix} d_{1,1} & d_{1,2} & \cdots & d_{1,N} & q_1 \\ d_{2,1} & d_{2,2} & \cdots & d_{2,N} & q_2 \\ \vdots & \vdots & \ddots & \vdots & \vdots \\ d_{M,1} & d_{M,2} & \cdots & d_{M,N} & q_M \end{pmatrix} \quad (4.10)$$

where:

q_i is the charge or beam intensity of pulse i .

The D_q matrix can then be written as follows:

$$D_q = \underbrace{\begin{pmatrix} u_{1,1} & u_{1,2} & \cdots & u_{1,M} \\ u_{2,1} & u_{2,2} & \cdots & u_{2,M} \\ \vdots & \vdots & \ddots & \vdots \\ u_{M,1} & u_{M,2} & \cdots & u_{M,M} \end{pmatrix}}_{\substack{\mathbf{U} \\ [M \times M]}} \cdot \underbrace{\begin{pmatrix} s_{1,1} & 0 & \cdots & 0 \\ 0 & s_{2,2} & \ddots & \vdots \\ \vdots & \ddots & \ddots & 0 \\ \vdots & & \ddots & s_{N+1,N+1} \\ 0 & \cdots & \cdots & 0 \\ \vdots & & & \vdots \\ 0 & \cdots & \cdots & 0 \end{pmatrix}}_{\substack{\mathbf{S} \\ [M \times N+1]}} \cdot \underbrace{\begin{pmatrix} v_{1,1} & v_{1,2} & \cdots & v_{1,N+1} \\ v_{2,1} & v_{2,2} & \cdots & v_{2,N+1} \\ \vdots & \vdots & \ddots & \vdots \\ v_{N+1,1} & v_{N+1,2} & \cdots & v_{N+1,N+1} \end{pmatrix}}_{\substack{\mathbf{V}^T \\ [N+1 \times N+1]}} \quad (4.11)$$

In order to study the correlations between the vertical orbit in the ATF2 beamline and the beam intensity, data were collected pulse by pulse. In the following case, the beam intensity was increased step by step every 1000 pulses from 1.0×10^9 electrons per bunch to 5.0×10^9 electrons per bunch as shown in Fig. 4.12.

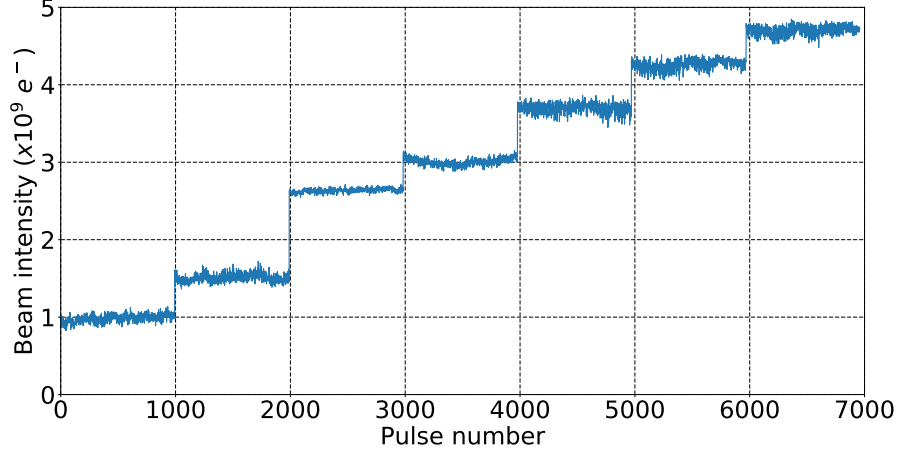


Figure 4.12: Beam intensity vs. pulse number, used for the Singular Value Decomposition studies.

The diagonal S matrix is shown in Fig. 4.13. In this case, a cut-off threshold for the noise was assumed at $\log_{10}(S_n) < 3$. This means that only the 6 first singular values were considered to be physical and the others are considered to be measurement noise.

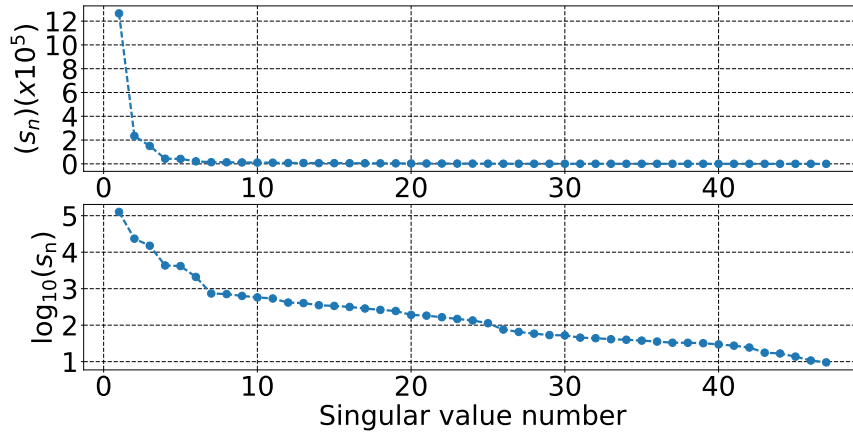


Figure 4.13: Amplitude of the singular values S_n vs. singular value number.

V: the spatial matrix

$$V = \underbrace{\begin{pmatrix} v_{1,1} & v_{1,2} & \cdots & v_{1,N+1} \\ v_{2,1} & v_{2,2} & \cdots & v_{2,N+1} \\ \vdots & \vdots & \ddots & \vdots \\ v_{N+1,1} & v_{N+1,2} & \cdots & v_{N+1,N+1} \end{pmatrix}}_{\text{Singular value number}} \left. \begin{array}{l} \text{BPM number} \\ \text{Beam intensity information} \end{array} \right\} \quad (4.12)$$

Each row of the spatial matrix V represents the amplitude of the correlation between the same column of D and a particular singular value. For example, the element V_{ij} tells how strong is the correlation between the i -th BPM (or the beam intensity for $i = N + 1$) and the j -th singular value. The strength of the correlation corresponds to the ranking of the singular values: the singular value ranking first corresponds to the strongest correlation. Thus, the spatial matrix V contains the information on the parameters that evolve with the orbit (betatron oscillations, dispersion, etc.). In this case, for example, the second column displays a very good match with the nominal dispersion through the ATF2 beamline, as shown in Fig. 4.14. The second singular value amplitudes were scaled to the vertical dispersion measurements. This suggests that the second singular value is associated with the beam energy variations.

The last row of the spatial matrix V represents the correlation between all singular values and the beam intensity. This is shown in Fig. 4.15. While the data show, for example, no correlation between the beam intensity and the second singular value, namely decoupling bunch charge variations from beam energy variations, one can observe a peak at the sixth singular value. This means that this singular value

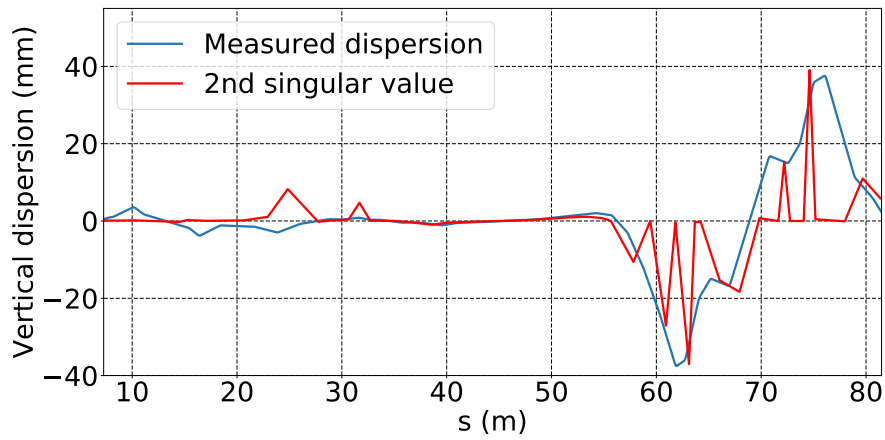


Figure 4.14: Amplitude of the second column of the spatial matrix V and measured vertical dispersion vs. s .

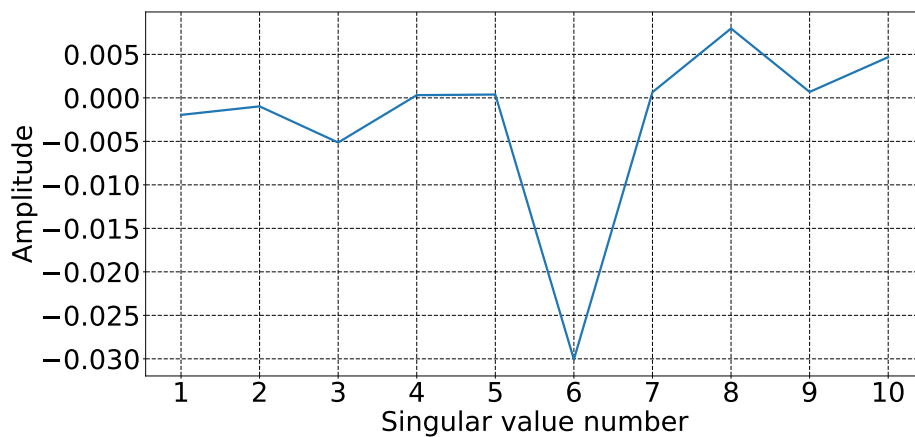


Figure 4.15: Last row of the spatial matrix V .

represents the correlation between the vertical orbit and the beam intensity. Thus, the sixth column of the spatial matrix V represents the correlation between the vertical orbit and the beam intensity vs. the BPM number. Figure 4.16 shows $V(:,6)$. Six peaks are seen, at BPM number 4, 6, 10 and 15, which are stripline BPMs and at BPMs 25 and 27 which are C-BPMs.

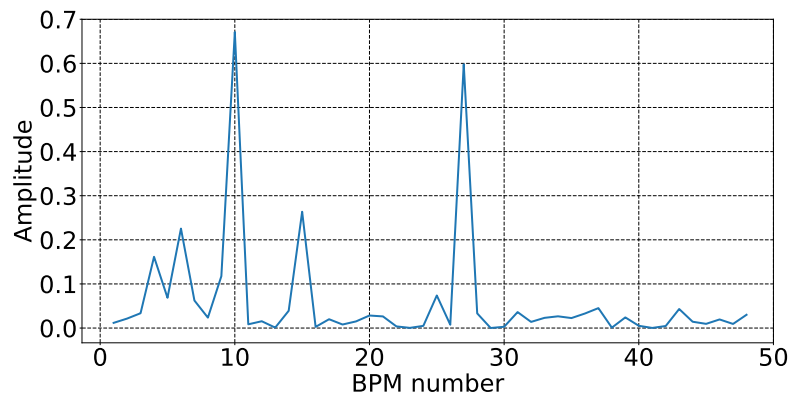


Figure 4.16: Amplitude of the sixth column of the spatial matrix V , representing correlation amplitude between the vertical beam orbit and the beam intensity vs. s .

U: the temporal matrix

$$U = \underbrace{\begin{pmatrix} u_{1,1} & u_{1,2} & \cdots & u_{1,M} \\ u_{2,1} & u_{2,2} & \cdots & u_{2,M} \\ \vdots & \vdots & \ddots & \vdots \\ u_{M,1} & u_{M,2} & \cdots & u_{M,M} \end{pmatrix}}_{\text{Singular value number}} \left. \vphantom{\begin{pmatrix} u_{1,1} \\ u_{2,1} \\ \vdots \\ u_{M,1} \end{pmatrix}} \right\} \text{Pulse number} \quad (4.13)$$

The temporal matrix U contains the information about correlations with the pulse number. As visible in Fig. 4.17, the sixth column corresponds to the evolution of the beam intensity with time, which confirms that the sixth singular value contains the beam intensity information.

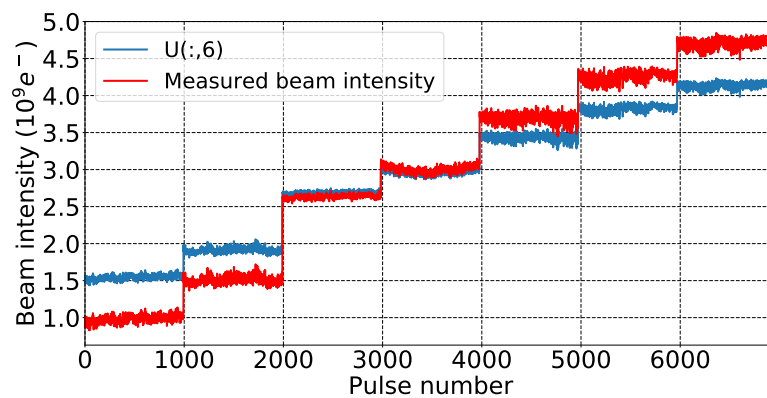


Figure 4.17: Amplitude of the sixth column of the temporal matrix U and the beam intensity vs. s .

One can now reconstruct the matrix D_q as $D_q = US_qV^T$, with S_q the diagonal matrix keeping only the sixth singular value. D_q represents the difference in the vertical orbit due to intensity-dependent effects for each BPM and pulse. Fig. 4.18 is a contour plot of the matrix D_q . The peaks show the locations where a strong correlation is observed between the orbit and the beam intensity: four stripline BPMs, MQD2X, MQF4X, MQD8X and MQD13X, corresponding to BPMs 4,6, 10 and 15 and two C-BPMs (MQM14FF and MQM12FF). This can mean two things, either the BPM is not properly calibrated and then it needs to be calibrated or if it is calibrated, then there is a strong wakefield source upstream of those BPMs or at those calibrated BPMs.

$$S_q = \begin{pmatrix} 0 & \dots & \dots & \dots & 0 \\ \vdots & \ddots & \ddots & & \vdots \\ \vdots & \ddots & s_{6,6} & \ddots & \vdots \\ \vdots & & \ddots & \ddots & 0 \\ 0 & \dots & \dots & 0 & 0 \\ \vdots & & & & \vdots \\ 0 & \dots & \dots & \dots & 0 \end{pmatrix} \quad (4.14)$$

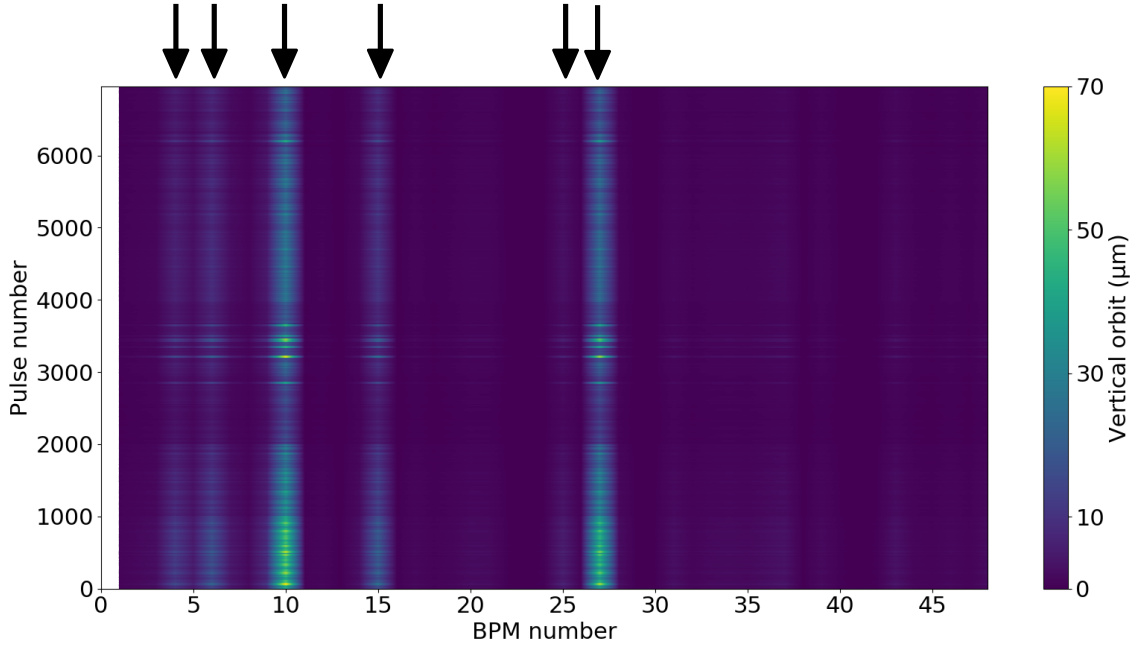


Figure 4.18: Contour plot of the reconstructed matrix D_q using only the sixth singular value. The arrows show the BPMs having a strong correlation between the measured vertical orbit and the beam intensity.

In conclusion, the SVD data analysis permitted one to extract, from raw BPM data, several physical parameters. If the beam intensity is added in the analysis, it permits one to localize BPMs where a strong correlation between the vertical orbit and the beam intensity is observed after filtering the noise part and to quantify the size of the impact of wakefields on the vertical orbit.

The beam intensity also has a significant impact on the vertical beam size at the IP as explained in the next section.

4.6 Impact of the beam intensity on the beam size

The ATF2 beam size is measured with the IPBSM, as described in Sec. 2.2.1. For each of the following experimental results, the beam had to be tuned manually. The first- and second-order knobs were applied iteratively in order to decrease the vertical IP beam size. As shown in Fig. 2.7, there are three laser crossing modes for the IPBSM. The ranges of the measurable beam sizes are summarized in Table 4.1. The “2-8° mode” can measure a beam size between 6 μm and 360 nm. Tuning starts with this mode. Then, when the beam is smaller than 400 nm, one can switch to the “30° mode” and continue the tuning until the beam size is smaller than 80 nm. Tuning is finally done after switching to the “174° mode”.

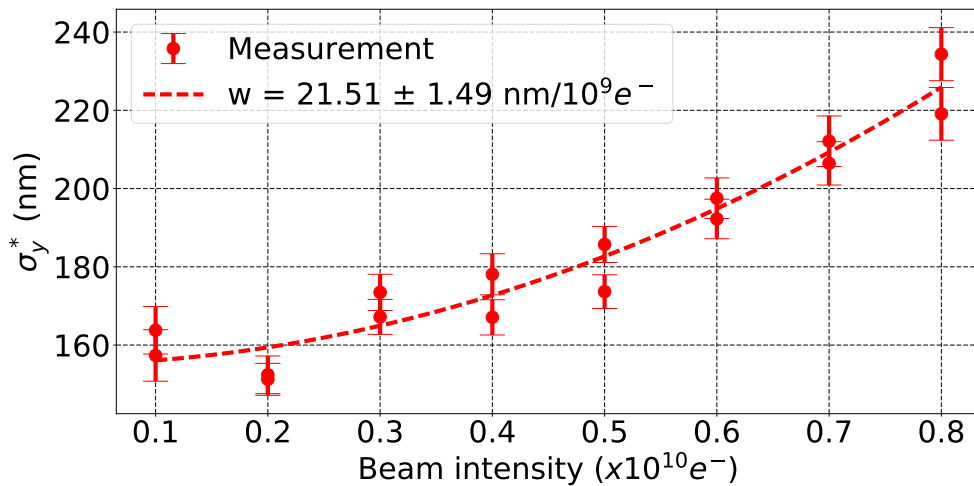


Figure 4.19: Measured vertical IP beam size (σ_y^*) vs. the beam intensity without applying DFS and WFS corrections and wakefield knobs.

Table 4.1: Dynamic range of the IPBSM.

Crossing angle θ	174°	30°	2-8°
Measurable range of σ_y^*	25 - 100 nm	80 - 400 nm	360 nm - 6 μm

Numerous measurements were done in order to study the intensity-dependent effects in ATF2. Most of them were done at “30° mode”. Figure 4.19 shows an example of measurements of σ_y^* vs. the beam intensity without applying DFS and WFS corrections and wakefield knobs, done at “30° mode”. 200 pulses were required to measure each beam size. The error bars represent the error due the IPBSM laser jitter, the beam orbit jitter and other types of errors, explained in [38]. The intensity dependence parameter w is $21.51 \pm 1.49 \text{ nm}/10^9 e^-$. This means that the vertical IP beam size would be 110 nm larger at $1 \times 10^{10} e^-$ than at $0.1 \times 10^{10} e^-$.

4.7 Mitigation strategies

4.7.1 Dispersion Free Steering

In order to reduce the intensity-dependent effects and to make the machine more stable, mitigation techniques and corrections were implemented and tested in ATF2. As in the simulations, the Dispersion Free Steering correction uses the ATF2 extraction line steering magnets or correctors to correct the difference in the orbit due to dispersion. A script was implemented in order to automatically calculate the impact of kicks at different positions on the orbit and build the response matrix. This matrix is $(N \times M)$ with N the number of steering magnets and M the number of BPMs. A first response matrix is calculated with a beam at the nominal beam energy of 1.3 GeV. A second response matrix is calculated for a beam with a higher energy of 1.3017 GeV. The DFS script finds a combination of corrector kicks that minimizes the impact of a change of energy and corrects the orbit at the same time. The results are shown in Fig. 4.20 and Fig. 4.21. In the horizontal plane, the goal is to make the dispersion as close as possible to the target (in red). In the vertical plane, the goal is to minimize the dispersion in the line. In both planes, the DFS correction decreases the impact of dispersion on the orbit and thus makes the machine more stable.

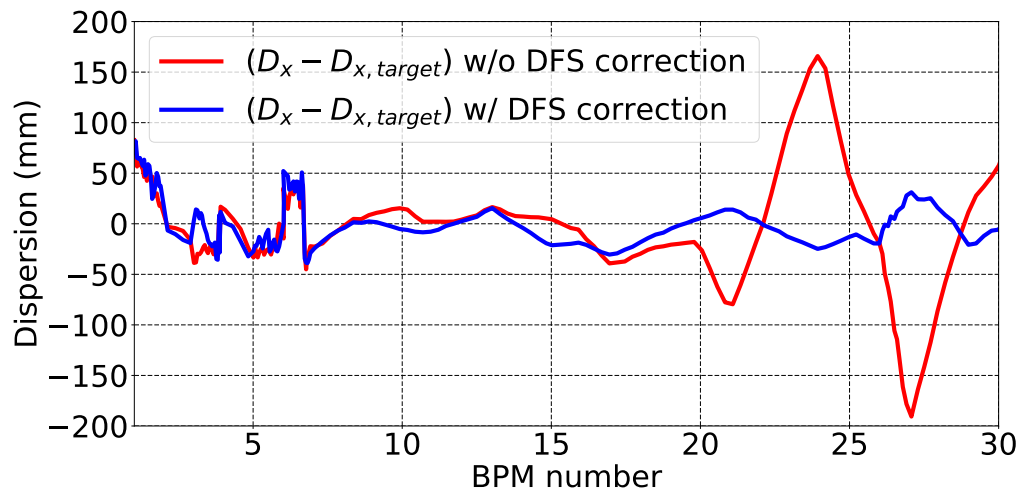


Figure 4.20: Difference between the measured horizontal dispersion (D_x) and the target dispersion ($D_{x,target}$) in the ATF2 beamline before and after applying DFS correction vs. BPM number.

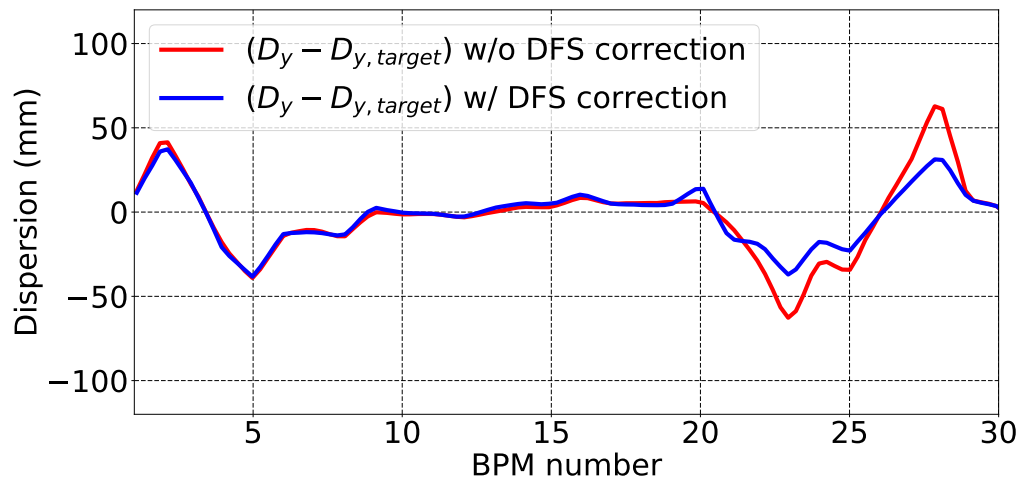


Figure 4.21: Difference between the measured vertical dispersion (D_y) and the target dispersion ($D_{y,target}$) in the ATF2 beam line before and after DFS correction vs. BPM number.

4.7.2 Wakefield Free Steering

The Wakefield Free Steering works like DFS but uses the beam intensity instead of the beam energy. The first WFS response matrix is computed for a beam intensity of 2.0×10^9 electrons. The second WFS response matrix is computed for a beam intensity of 6.0×10^9 electrons. As in DFS, the strength of the correctors is calculated in order to reduce the impact of wakefields on the beam orbit. Figure 4.22 shows the convergence of the WFS correction. After 10 iterations, the norm of the difference between the vertical orbit at high intensity, 6.0×10^9 electrons (y_{HQ}) and at low intensity, 2.0×10^9 electrons, (y_{LQ}) defined as $\|y_{HQ} - y_{LQ}\| = \sqrt{\sum |y_{HQ} - y_{LQ}|^2}$, at each BPM, is decreased by more than 30%. This means that, on average, at each BPM, the impact of wakefields on the vertical orbit was decreased by 12μ .

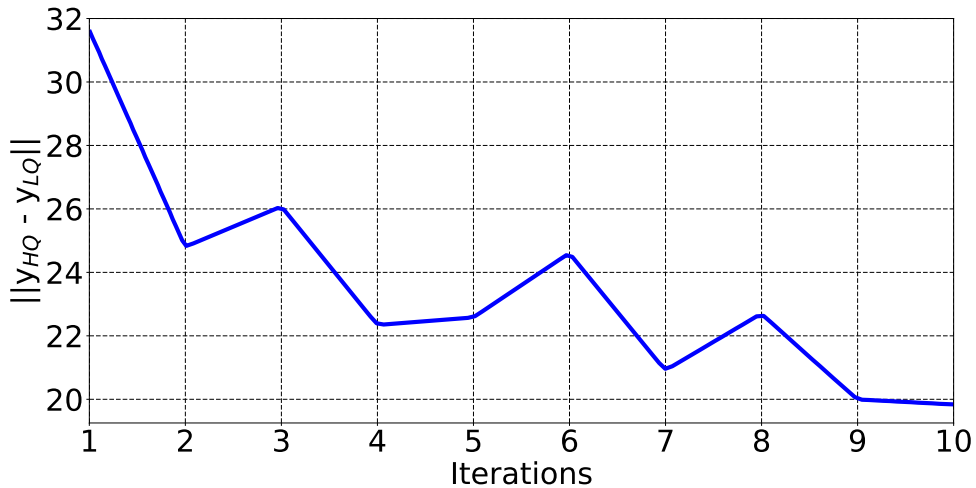


Figure 4.22: Norm of the difference between the vertical orbit at high intensity, 6.0×10^9 electrons (y_{HQ}) and at low intensity, 2.0×10^9 electrons, (y_{LQ}) vs. the number of iterations of the WFS correction.

4.7.3 Impact of DFS and WFS on the vertical IP beam size

After applying DFS and WFS corrections, the machine should be less sensitive to dispersion and wakefields. In Fig. 4.23 is shown the impact of DFS and WFS the vertical beam size at the IP σ_y^* . For each beam size measurement, 200 consecutive pulses are taken into account. The error bars represent the standard error for 200 pulses. In conclusion, the DFS and WFS corrections reduced the intensity dependence parameter from $22.39 \pm 1.18 \text{ nm}/10^9 e^-$ to $15.04 \pm 2.02 \text{ nm}/10^9 e^-$. Intensity-dependent effects on the beam size at the IP were clearly decreased.

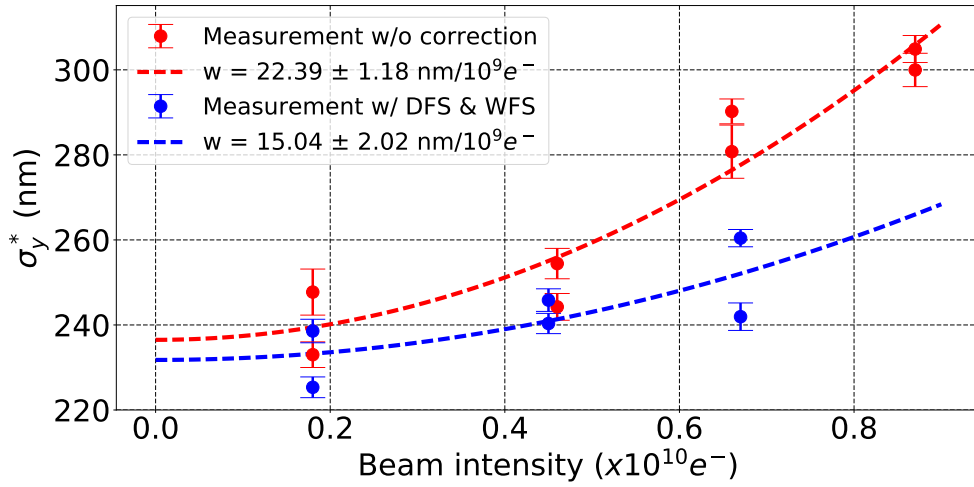
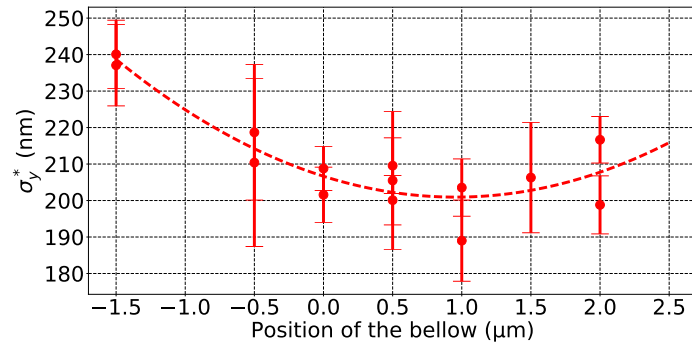


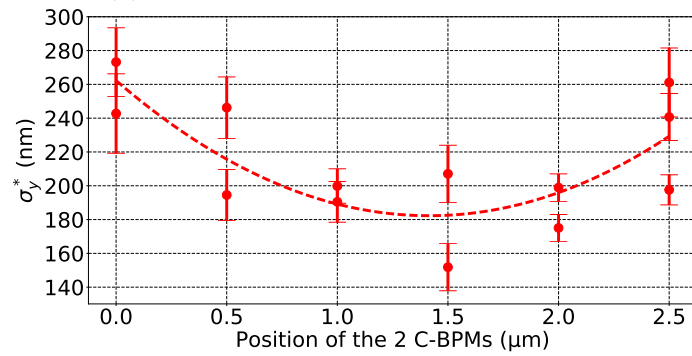
Figure 4.23: Measured vertical IP beam size (σ_y^*) vs. the beam intensity without correction and with DFS and WFS corrections.

4.7.4 Wakefield knobs

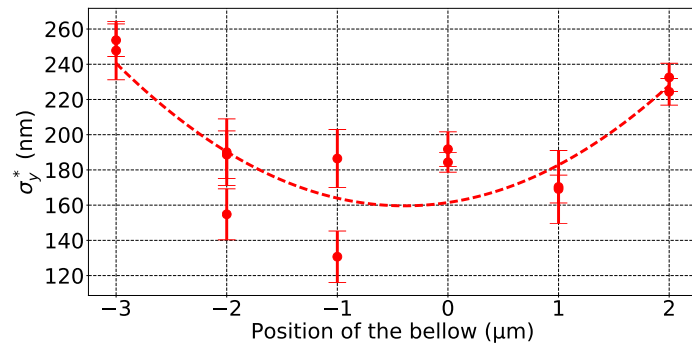
As described in 3.5, a wakefield knobs system was implemented inside the ATF2 beam line. The measurements are similar to what is done in simulations. The position of the mover with two C-BPMs was first scanned, then the position of the mover with the bellows. This was done iteratively in order to find the best position of those two movers. A few iterations of these measurements are shown in Fig. 4.24. First, the position of the bellows mover is scanned and a minimum beam size of 200 nm is achieved as shown in Fig. 4.24a. The position of the C-BPMs mover is then scanned and decrease the vertical IP beam size (σ_y^*) to 180 nm as shown in Fig. 4.24b. A second iteration of the bellows mover is then applied to obtain a beam size of 160 nm as shown in Fig. 4.24c. Finally, a beam size of 150 nm is reached with a second iteration of the C-BPMs mover as shown in Fig. 4.24d. These scans were done at $0.77 \times 10^{10} e^-$. The impact of the wakefield corrections is shown in Fig. 4.25. The error bars represent the standard error for 200 pulses. One has to note that the wakefield correction was applied on an uncorrected machine and not after applying DFS and WFS because of issues in the beamline during the measurement. The intensity-dependent parameter was decreased from $27.13 \pm 1.40 \text{ nm}/10^9 e^-$ to $14.51 \pm 1.26 \text{ nm}/10^9 e^-$. This wakefield knob system seems efficient to reduce the impact of wakefield kicks and the intensity-dependent effects in general. It offers freedom in the correction with two movers and two different wakefield sources.



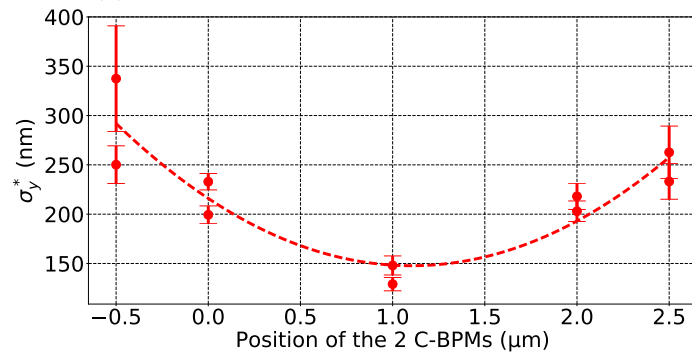
(a) First iteration of the bellows mover



(b) First iteration of the C-BPMs mover



(c) Second iteration of the bellows mover



(d) Second iteration of the C-BPMs mover

Figure 4.24: Impact of ATF2 wakefield knobs iterations measurements: 4 consecutive steps of the vertical IP beam size (σ_y^*) vs. the wakefield knobs movers' positions.

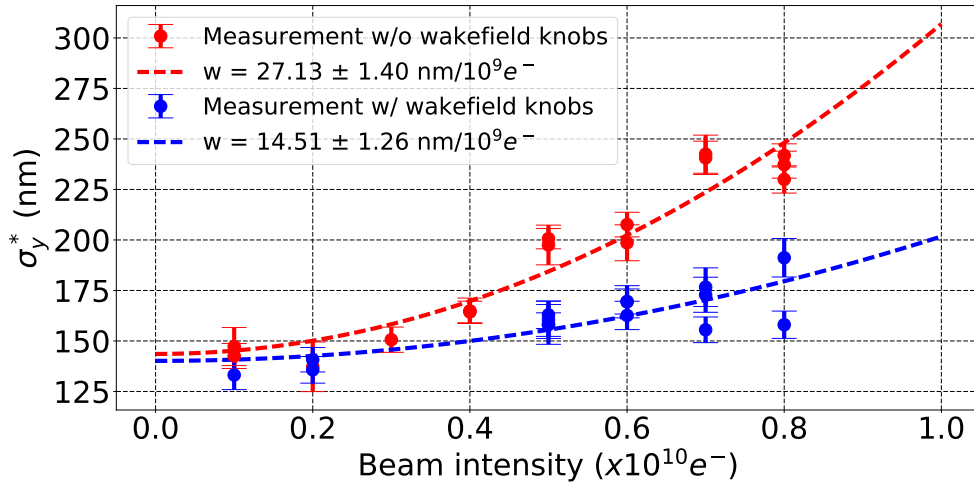


Figure 4.25: Measured vertical IP beam size (σ_y^*) vs. the beam intensity before and after applying wakefield knobs.

4.8 Comparison between simulations and measurements

In order to compare simulations and measurements, the vertical IP beam size was measured at 174° mode after spending a long time tuning the beam and applying corrections. Figure 4.26 shows that at low beam intensity, $0.1 \times 10^{10} e^-$, a vertical IP beam size of 57 nm was obtained and at a higher beam intensity, $0.4 \times 10^{10} e^-$, the vertical IP beam size was 72 nm. The error bars represent the standard error for 200 pulses. The measured intensity-dependent parameter was $w = 13.76 \pm 1.59$ nm/ $10^9 e^-$. These measurements are compared with PLACET simulation considering the following simulation conditions: quadrupoles, C-BPMs and sextupoles have a misalignment of 100 μm RMS and a roll error of 200 μrad RMS, the strength error of quadrupoles and sextupoles is 10^{-4} RMS. One-to-one, DFS, WFS corrections and IP knobs are applied on the machine. This is done for 100 machines and 200 pulses per machine. The incoming position jitter is $1.0\sigma_y$ and the incoming angle jitter is $1.0\sigma_{y'}$. The simulated intensity-dependent parameter was $w = 13.78 \pm 0.34$ nm/ $10^9 e^-$. These results are summarized in Table 4.2.

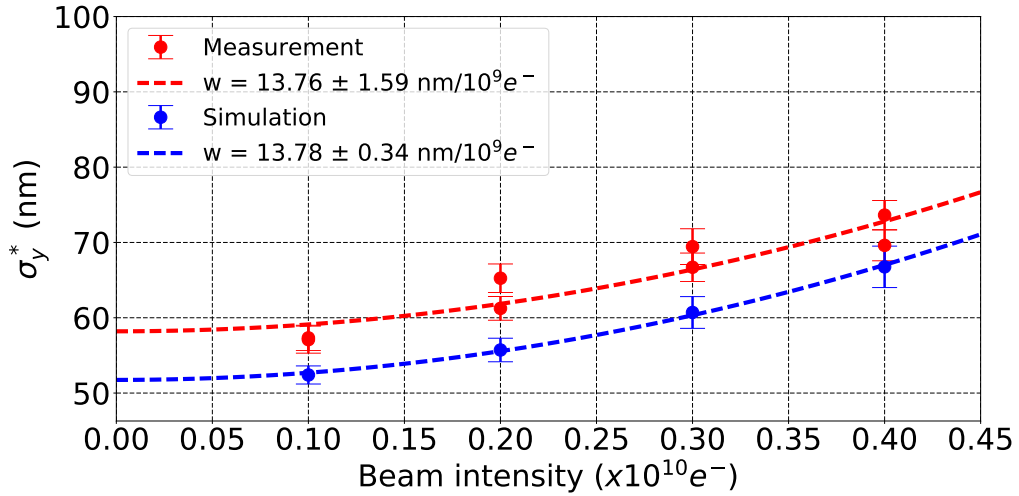


Figure 4.26: Comparison between measurements and simulations of the vertical beam size at the IP (σ_y^*) vs. the beam intensity and the intensity-dependent parameter w .

Table 4.2: Comparison between measurements and simulations of the vertical beam size at the IP (σ_y^*) vs. the beam intensity and the intensity-dependent parameter w .

Case	w [nm/ $10^9 e^-$]	Beam intensity [e^-]	Average σ_y^* [nm]
Measurement	13.76 ± 1.59	0.1×10^{10}	57 ± 1.7
		0.2×10^{10}	63 ± 1.7
		0.3×10^{10}	68 ± 2.1
		0.4×10^{10}	72 ± 2.0
Simulation	13.78 ± 0.34	0.1×10^{10}	52 ± 1.2
		0.2×10^{10}	56 ± 1.6
		0.3×10^{10}	61 ± 2.1
		0.4×10^{10}	67 ± 2.8

In conclusion, measurements in the ATF2 beamline permitted to quantify and mitigate a few effects. The bunch length is increasing from 6 mm at $0.1 \times 10^{10} e^-$ to 8.5 mm at $0.8 \times 10^{10} e^-$ in ATF2. The orbit, dispersion and beam intensity drifts have been measured and the temperature seems to be responsible on the short period drift of the beam intensity. The incoming position jitter was measured with both FONT and ATF2 stripline-BPMs. The conclusion is that the incoming vertical position jitter is around 6 μm , which represents $1.0 \times \sigma_y$. The BPMs vertical resolution

was measured for each BPMs, with an average of 600 nm for C-BPMs at $0.5 \times 10^{10} e^-$, with a minimum of 68 nm at BPM MQD4AFF. The SVD analysis permitted to reconstruct the correlation matrix D_q in order to localise the sources of wakefields or the uncalibrated BPMs. The DFS and WFS corrections lead to a decrease of the dispersion in both planes and reduced the intensity-dependent parameter from 22.39 ± 1.18 nm/ $10^9 e^-$ to 15.04 ± 2.02 nm/ $10^9 e^-$. The wakefield knobs corrections also showed some promising results, decreasing the intensity-dependent parameter from 27.13 ± 1.40 nm/ $10^9 e^-$ to 14.51 ± 1.26 nm/ $10^9 e^-$. ATF2 PLACET realistic simulations considering the number of wakefield sources, their localisation, their wakepotential, the static and dynamic imperfections but also the impact of the One-to-one, DFS, WFS corrections and the IP and wakefield knobs, reproduce what was measured in the ATF2 beamline. The measured intensity-dependent parameter was 13.76 ± 1.59 nm/ $10^9 e^-$ and the simulated one was 13.78 ± 0.34 nm/ $10^9 e^-$.

The intensity-dependent effects due to wakefields were studied in both ILC and CLIC using the same wakefield implementation than in ATF2. The results are presented in the next two chapters. The good match between PLACET simulations and measurements in ATF2 makes the results on ILC and CLIC more trustworthy.

Chapter 5

Intensity dependent effects in the ILC BDS

5.1 ILC BDS 250 GeV

5.1.1 Beam and machine parameters

The 250 GeV center-of-mass energy stage would be the first stage of the ILC. In order to simulate the impact of wakefields in the ILC BDS, the latest official 500 GeV lattice was translated from MAD (Methodical Accelerator Design) to PLACET. The MAD version was found on G. White's Bitbucket [64]. The 250 GeV lattice was obtained by scaling down the 500 GeV lattice. The ILC BDS final focus system is based on local chromaticity correction (Section 2.1.3). For the 250 GeV ILC, the vertical beam size at the IP is squeezed to 7.7 nm and a luminosity of $0.82 \times 10^{34} \text{ cm}^{-2}\text{s}^{-1}$ is obtained [18]. At the end of the 2254 meter long BDS, as in ATF2, a final doublet is used, with two strong quadrupoles, in order to focus the beam at the IP. The vertical phase advance between the entrance of the BDS and the IP is 12π , which means that an incoming angle offset will translate into an angle offset at the IP and an incoming position offset will translate into a position offset at the IP. The horizontal and vertical phase advances and the Twiss functions in the ILC 250 GeV BDS are shown in Fig. 5.1. The ILC 250 GeV main parameters are summarized in Table 5.1.

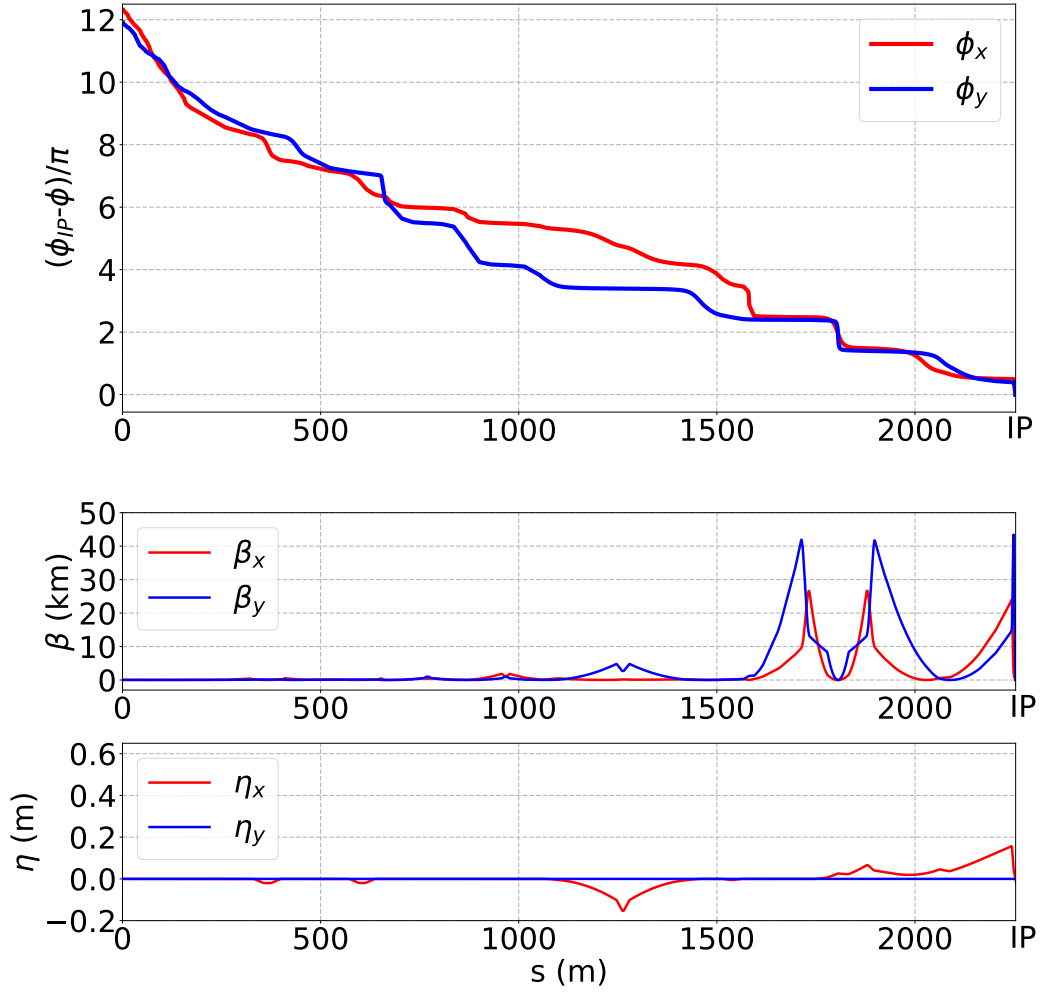


Figure 5.1: The ILC BDS 250 GeV phase advance (top) and the ILC BDS 250 GeV Twiss parameters calculated with PLACET (bottom).

Table 5.1: ILC 250 GeV beam parameters.

Parameter	Symbol	Value
Centre-of-mass energy	E_{CM}	250 GeV
Length of the BDS	L_{BDS}	2254 m
Number of bunches	n_b	1312
Bunch population	N	$2.0 \times 10^{10} e^-$
RMS bunch length	σ_z	0.3 mm
Bunch separation	Δt_b	554 ns
IP RMS beam sizes	σ_x^*/σ_y^*	516/7.7 nm

5.1.2 Single-bunch simulations

5.1.2.1 Efficiency of Beam-Based Alignment corrections

The efficiency of the Beam-Based Alignment correction and knobs in the ILC BDS was studied with PLACET. A Gaussian beam comprised of 2.0×10^{10} electrons and 30,000 macro-particles was tracked from the entrance of the BDS to the IP. As in ATF2, the ILC 101 C-BPMs generate wakefield kicks. The positions of those BPMs are listed in Appendix B. The wakepotential of these C-BPMs was calculated using GdfidL for a 300 μm long bunch and is shown in Fig. 5.2. Imperfections are taken into account: misalignment and roll error of quadrupoles, C-BPMs and sextupoles by respectively 50 μm RMS and 200 μrad RMS and a quadrupole, and sextupole strength error of 1.0×10^{-4} . These values are based on the studies done in [65]. 100 machines were studied and the same corrections as in ATF2 were applied: One-to-one steering, DFS, WFS and the following knobs: $\langle y, x' \rangle$, $\langle y, y' \rangle$, $\langle y, E \rangle$ and $\langle y, x' \times x' \rangle$, $\langle y, x' \times y' \rangle$ $\langle y, x' \times E \rangle$.

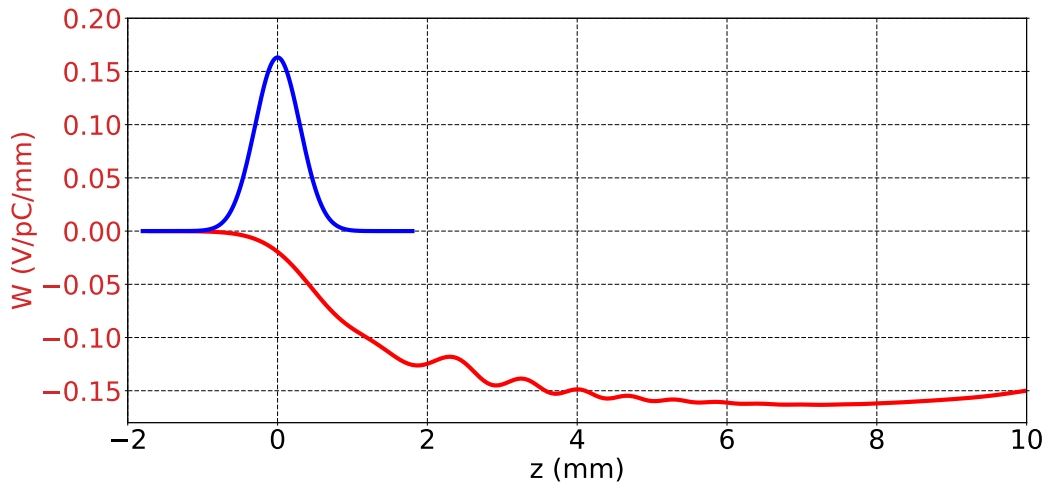


Figure 5.2: Transverse wakepotential in V/pC/mm of the ILC C-BPM, calculated with GdfidL for a vertical offset of 1 mm, Gaussian bunch length of 0.3 mm and 1 pC charge (in red). For reference, the distribution of the electrons in one bunch is shown (in blue).

The impact of the corrections on the particle distribution at the IP for one machine is shown in Fig. 5.3. In order to show the impact of each single correction, the particle distributions were centered plotting $Y' - \overline{Y'}$ and $Y - \overline{Y}$. The results of the corrections on the average vertical beam size at the IP ($\overline{\sigma_y^*}$) for 100 machines are shown in Fig. 5.4 and are summarized in Table 5.2.

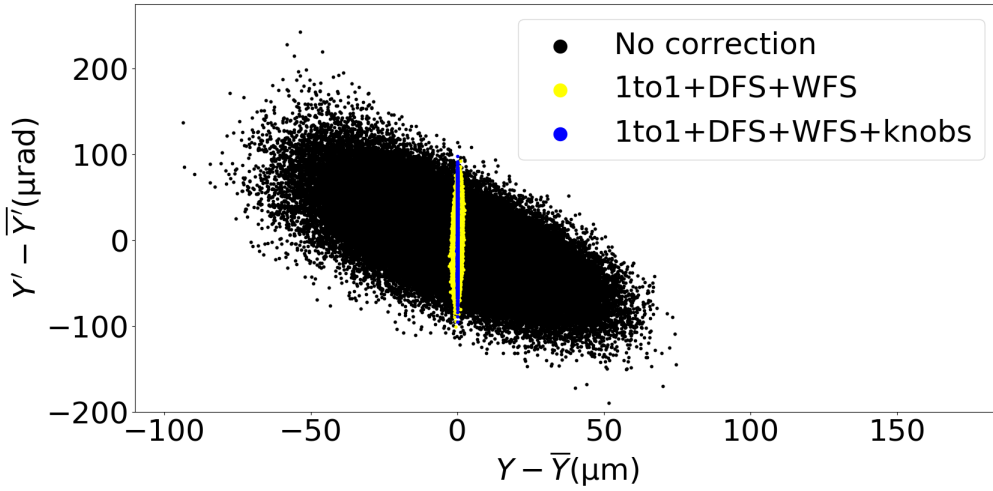


Figure 5.3: Centered vertical phase space at the 250 GeV ILC BDS IP, $Y' - \bar{Y}'$ vs. $Y - \bar{Y}$, for 3 cases: no correction, One-to-one steering, DFS, WFS and One-to-one steering, DFS, WFS and knobs, calculated with PLACET with wakefields.

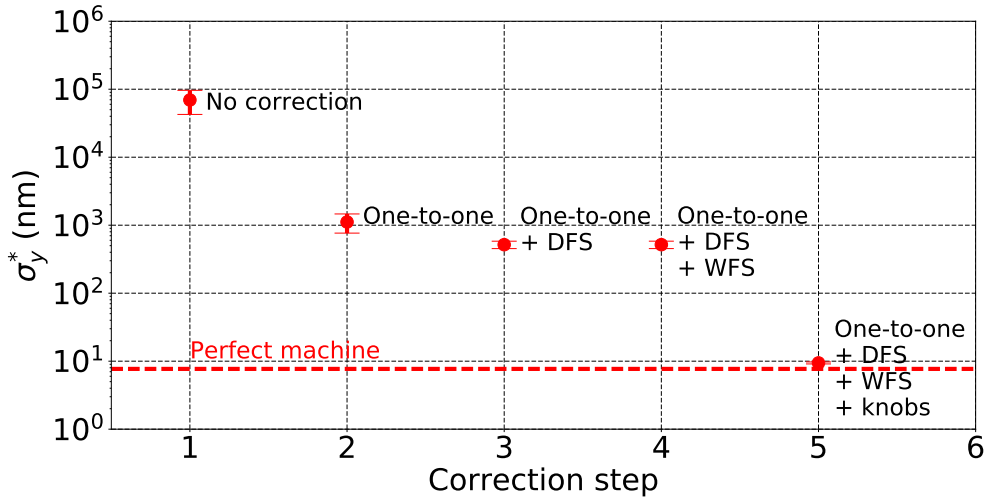


Figure 5.4: Average vertical beam size at the 250 GeV ILC IP (σ_y^*) vs. correction step: One-to-one, DFS, WFS corrections and IP tuning knobs. The red dashed line show the vertical beam size at the IP for a perfect machine, 7.7 nm.

The average vertical IP beam size is decreased after each correction. One-to-one correction does most of the work, then, DFS and WFS make the machine less sensitive to energy and intensity changes, while they decrease the IP beam size. The error bars represent the standard error for the 100 machines. The whole procedure reduces the

average vertical IP beam $\overline{\sigma_y^*}$ from $69.4 \pm 26.8 \mu\text{m}$ without any correction to $9.43 \pm 0.32 \text{ nm}$ with One-to-one, DFS, WFS and knobs. In comparison, the vertical IP beam size in a perfect machine is 7.7 nm .

Table 5.2: Impact of the corrections on the ILC 250 GeV vertical beam size at the IP (σ_y^*) for 100 machines with wakefields and with a beam intensity of $2.0 \times 10^{10} e^-$, simulated with PLACET.

Correction	$\overline{\sigma_y^*}$
No correction	$69.4 \pm 26.8 \mu\text{m}$
One-to-one	$1.1 \pm 0.3 \mu\text{m}$
One-to-one + DFS	$514 \pm 65 \text{ nm}$
One-to-one + DFS + WFS	$512 \pm 64 \text{ nm}$
One-to-one + DFS + WFS + knobs	$9.43 \pm 0.32 \text{ nm}$

5.1.2.2 Impact of static errors

In order to study the impact of static errors, the following simulation conditions were used with PLACET: misalignment and roll error of quadrupoles, C-BPMs and sextupoles by respectively $50 \mu\text{m}$ RMS and $200 \mu\text{rad}$ RMS and quadrupoles, sextupoles strength error of 1.0×10^{-4} . 100 machines were studied and the same corrections as in ATF2 were applied: One-to-one, DFS, and the following knobs: $\langle y, x' \rangle$, $\langle y, y' \rangle$, $\langle y, E \rangle$ and $\langle y, x' \times x' \rangle$, $\langle y, x' \times y' \rangle$ $\langle y, x' \times E \rangle$. This was done for intensities between $2.0 \times 10^9 e^-$ and $2.0 \times 10^{10} e^-$. The impact of wakefields on the average vertical IP beam size σ_y^* is shown in Fig. 5.5 and summarized in Table 5.3. The error bars represent the standard error for 100 machines. The beam size growth due to the short-range wakefield is negligible if one considers all C-BPMs as wakefield sources. Indeed, the growth between the vertical IP beam size at $2.0 \times 10^9 e^-$ and $2.0 \times 10^{10} e^-$ is 0.03 nm , around 0.32% of the nominal beam size. The effect is 430 times smaller in the ILC 250 GeV BDS than in ATF2 considering this previously cited conditions and imperfections. However, in reality, a bunch train made of 1312 bunches is traveling in the ILC BDS. Each bunch feels the already studied short range wakefield, wakefield acting on the bunch which generated it, but also generates a long-range wakefield which affects the following bunches.

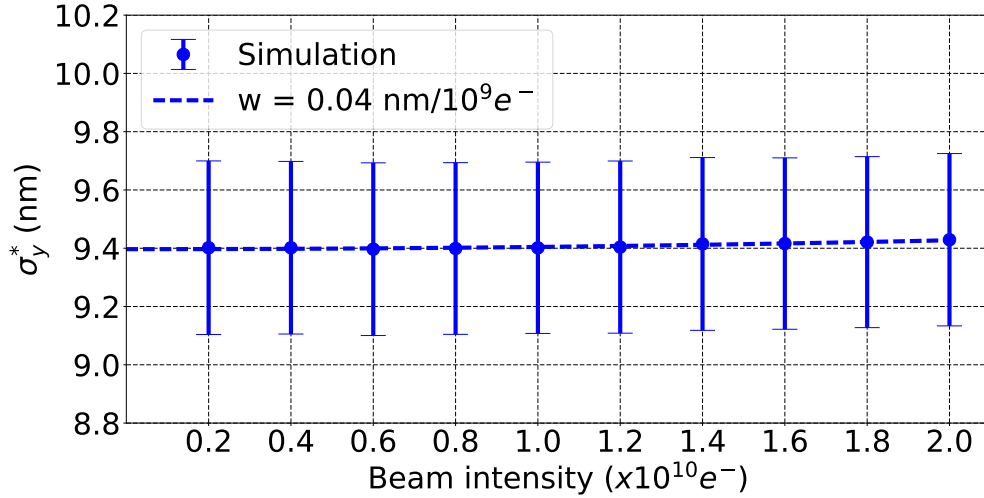


Figure 5.5: Vertical IP beam size σ_y^* vs. beam intensity in the 250 GeV BDS, calculated with PLACET with wakefields.

Table 5.3: Intensity-dependent effects due to wakefields on the vertical IP beam size σ_y^* in the 250 GeV ILC BDS, calculated with PLACET with wakefields.

Beam intensity	$\overline{\sigma_y^*}$ (nm)	w (nm/10 ⁹ e ⁻)
0.2×10 ¹⁰ e ⁻	9.40 ± 0.30	0.04
2.0×10 ¹⁰ e ⁻	9.43 ± 0.30	

5.1.3 Multi-bunch simulations

5.1.3.1 Long range wakefield

In order to study the multi-bunch intensity dependence and dynamic imperfection effects in the ILC BDS, one should consider long-range wakefields such as those generated by resistive walls. The ILC BDS beam aperture profile is shown in Fig. 5.6. It has an aperture between 10 mm and 30 mm. The resistive walls wakepotential W_l used in the simulations is defined as follows [66][67]:

$$W_l(z) = -\frac{c}{\pi b^3} \sqrt{\frac{Z_0}{\sigma_r \pi z}} L \quad (5.1)$$

where b is the radius of the beam pipe, Z_0 is the impedance of the vacuum, σ_r the conductivity of the pipe, L the length of the beam line segment. In the ILC BDS, the

bunch separation is 554 ns and there are 1312 consecutive bunches. Thus, the length of the bunch train is 217.9 km. In Fig. 5.7 is shown the calculated wakepotential for the ILC BDS resistive walls, considering a copper beam pipe and a beam pipe radius of 10 mm for the length of a train (~ 218 km) and for the length of the ILC BDS (~ 2254 m). A corresponding wakepotential was calculated and used as a wakefield sources for each beam pipe aperture.

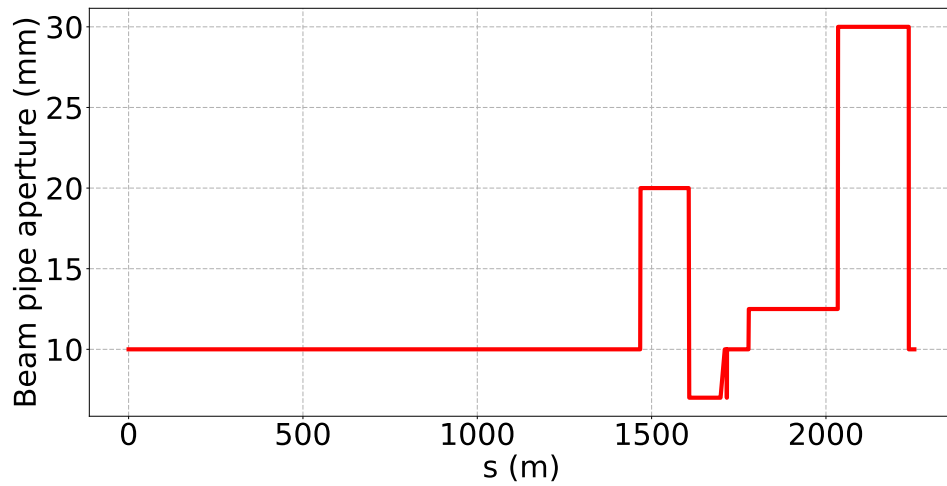


Figure 5.6: The ILC BDS beam aperture profile vs. s .

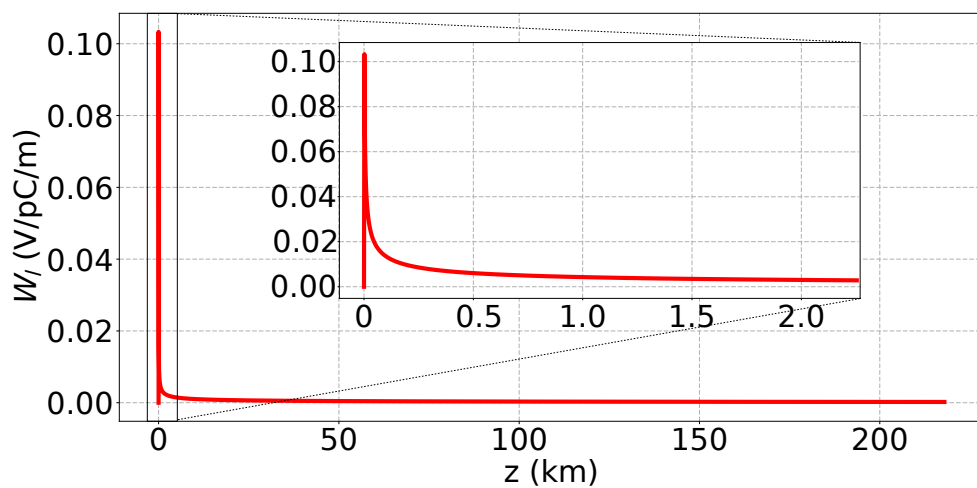


Figure 5.7: The ILC resistive walls wakepotential for a copper beam pipe with a constant radius of 10 mm for the length of a train (~ 218 km). The zoom shows the wakepotential for the length of the ILC BDS (~ 2254 m).

5.1.3.2 Impact of long-range wakefields for a train with a constant incoming offset

Given that the kick due to long-range wakefields is uniform on one whole bunch, one can consider just one macro-particle per bunch. This macro-particle represents the barycenter of this bunch and carries the full charge of the bunch. The effects of the resistive walls with PLACET were simulated using one macro-particle per bunch. The consecutive 1312 bunches of the ILC train were injected in a perfectly aligned machine with the same offset. The bunches were tracked all the way to the IP where the orbit of each bunch was calculated. This study was done for initial offsets of $0.01\sigma_y$, $0.05\sigma_y$ and $0.1\sigma_y$ in position and $0.1\sigma_{y'}$ in angle (where σ_y and $\sigma_{y'}$ are respectively the beam size and beam divergence at the entrance of the BDS). In Fig. 5.8 and Fig. 5.9 are shown the vertical orbit difference (Δ_{y^*}) between the first bunch and the last bunch of a train at the IP for five different beam intensities for respectively an incoming position offset of $0.1\sigma_y$ and an incoming angle offset of $0.1\sigma_{y'}$. The conclusion is that the impact of dynamic error is significant. Indeed, the last bunch of a train gets deflected by more than 3.0 nm for an incoming position offset of $0.1\sigma_y$ and by 19.9 nm for an incoming angle offset of $0.1\sigma_{y'}$ at $1.0 \times 10^{10} e^-$. The orbit deflection increases linearly with the bunch number. The IP vertical orbit deflection also scales with the amplitude of the error as shown in Fig. 5.10. In order to quantify more easily the impact of dynamic errors, one can use the vertical orbit deflection at the IP (Δ_{y^*}) normalised by the vertical IP beam size (σ_y^*), in this case $\sigma_y^* = 7.7$ nm. Figure 5.11 shows the impact of an incoming position offset of $0.01\sigma_y$ and an angle offset of $0.01\sigma_{y'}$ on the vertical orbit deflection at the IP and how it scales with the beam intensity. These offset values are in the order of magnitude of the ones calculated for CLIC [68, 69]. At $2.0 \times 10^{10} e^-$, the last bunch of the train is deflected by $1.85\sigma_y^*$ compared to the first one. In reality, the incoming jitter will also have a horizontal component. The impact of an incoming position offset of $0.01\sigma_x$ and an angle offset of $0.01\sigma_{x'}$ in the horizontal plane and $0.01\sigma_y$ and $0.01\sigma_{y'}$ in the vertical plane on the vertical orbit deflection at the IP is shown in Fig. 5.12. In this case, at $2.0 \times 10^{10} e^-$, the last bunch of the train is deflected by $4.15\sigma_y^*$ compared to the first one.

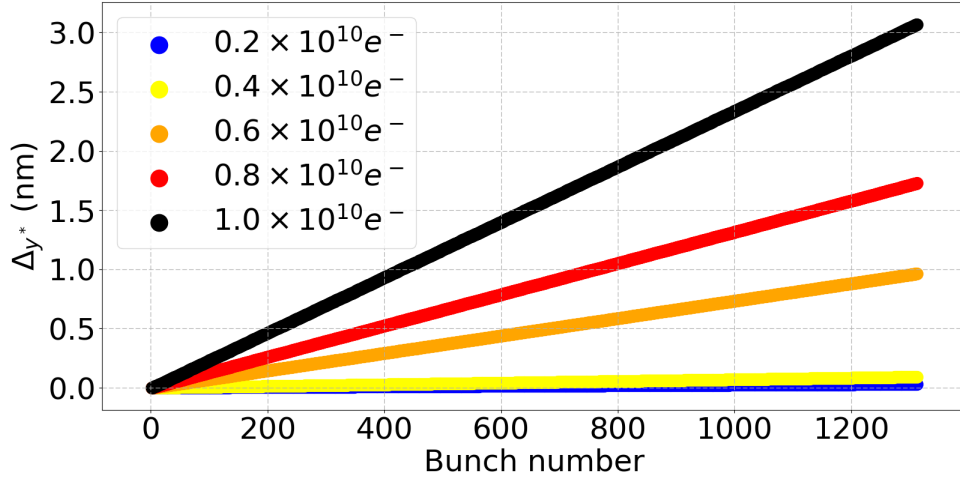


Figure 5.8: Vertical orbit deflection at the IP between the first and last bunch of a train Δy^* vs. bunch number for a train with a constant incoming position offset of $0.1\sigma_y$ of the train of bunches in the 250 GeV ILC BDS for 5 beam intensities, calculated with PLACET with resistive wall effects included.

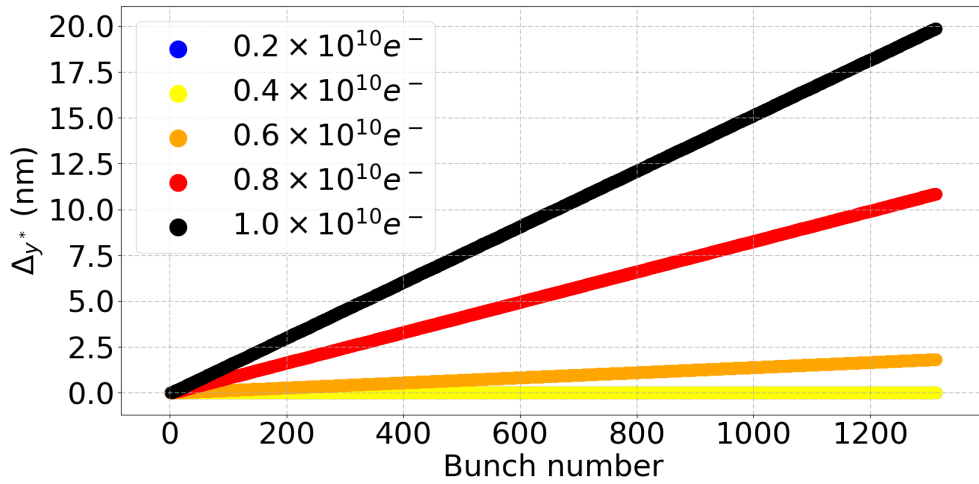


Figure 5.9: Vertical orbit deflection at the IP between the first and last bunch of a train Δy^* vs. bunch number for a train with a constant incoming angle offset of $0.1\sigma_{y'}$ of the train of bunches in the 250 GeV ILC BDS for 5 beam intensities, calculated with PLACET with resistive wall effects included.

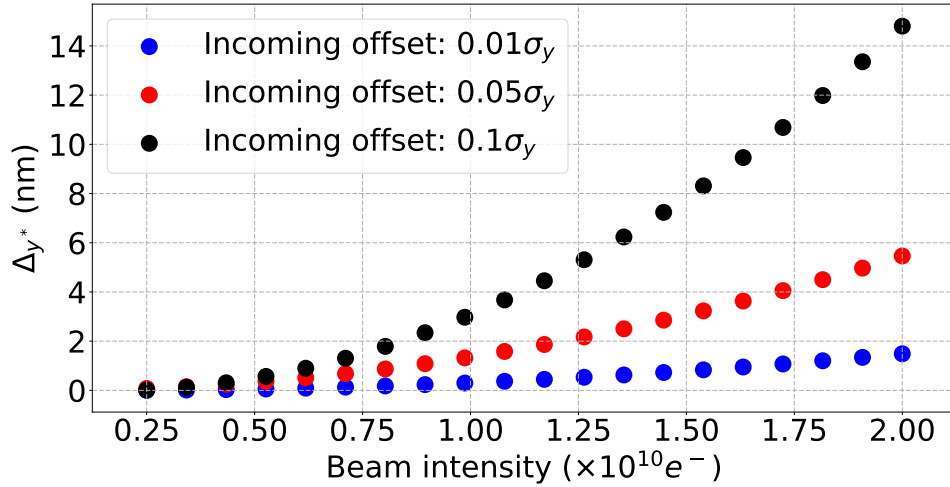


Figure 5.10: Vertical orbit deflection at the IP between the first and last bunch of a train Δy^* vs. beam intensity for three incoming constant position offsets of the train of bunches in the 250 GeV ILC BDS: $0.01\sigma_y$, $0.05\sigma_y$ and $0.1\sigma_y$, calculated with PLACET with resistive wall effects included.

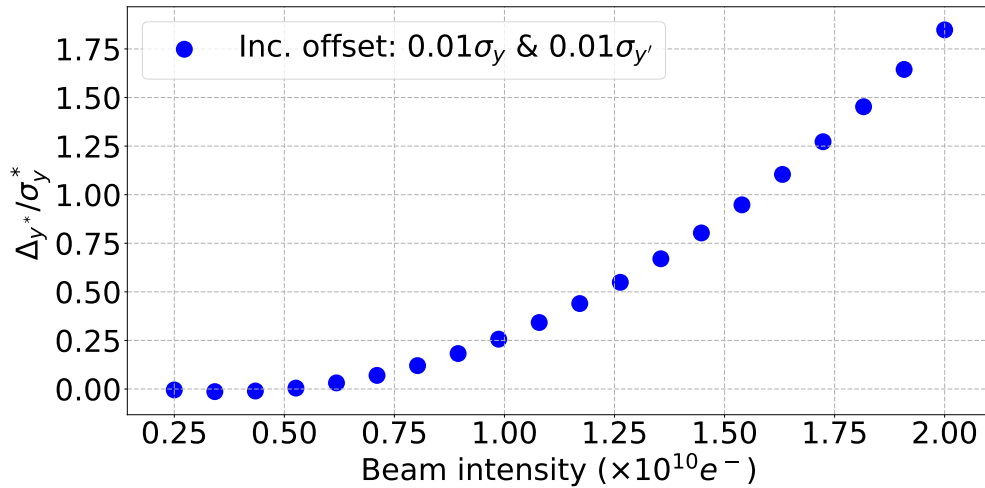


Figure 5.11: Vertical orbit deflection at the IP between the first and last bunch of a train normalised by the IP vertical beam size ($\Delta y^*/\sigma_y^*$) vs. beam intensity for a train with incoming constant position and angle offsets of respectively $0.01\sigma_y$ and $0.01\sigma_{y'}$ in the 250 GeV ILC BDS, calculated with PLACET with resistive wall effects included.

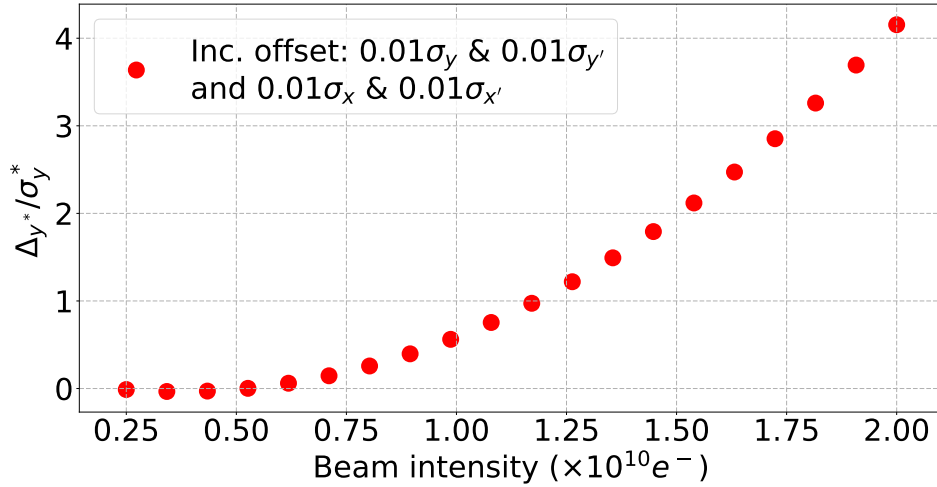


Figure 5.12: Vertical orbit deflection at the IP between the first and last bunch of a train normalised by the IP vertical beam size ($\Delta y^*/\sigma_y^*$) vs. beam intensity for a train with incoming constant horizontal position and angle offsets of respectively $0.01\sigma_x$ and $0.01\sigma_{x'}$ and vertical incoming position and angle offsets of respectively $0.01\sigma_y$ and $0.01\sigma_{y'}$ in the 250 GeV ILC BDS, calculated with PLACET with resistive wall effects included.

5.1.3.3 Impact of long-range wakefields for a train with random incoming offset

A different approach is to consider incoming consecutive bunches of a train with a random incoming offset. Indeed, the incoming jitter could fluctuate due to different sources like the vibration of quadrupole magnets, strength jitter of quadrupole and dipole magnets, etc. [70]. In this study, incoming consecutive 1312 bunches were injected with normally distributed position and angle offsets between -5% and 5% with an average of zero [71]. The distribution of the incoming offsets is shown in Fig. 5.13. This offset distribution was used for the incoming horizontal and vertical position and angle jitters and multiplied by the corresponding values of σ_x , $\sigma_{x'}$, σ_y and $\sigma_{y'}$. The resulting vertical vertical orbit deflection between the first and last bunch is shown in Fig. 5.14. The effects of random incoming offsets lead to kicks compensating each other inside the ILC BDS, resulting in a small orbit deflection at the IP. The last bunch of a train is deflected by $0.065\sigma_y^*$, or 0.501 nm, which is negligible compared to the beam size of 7.7 nm.

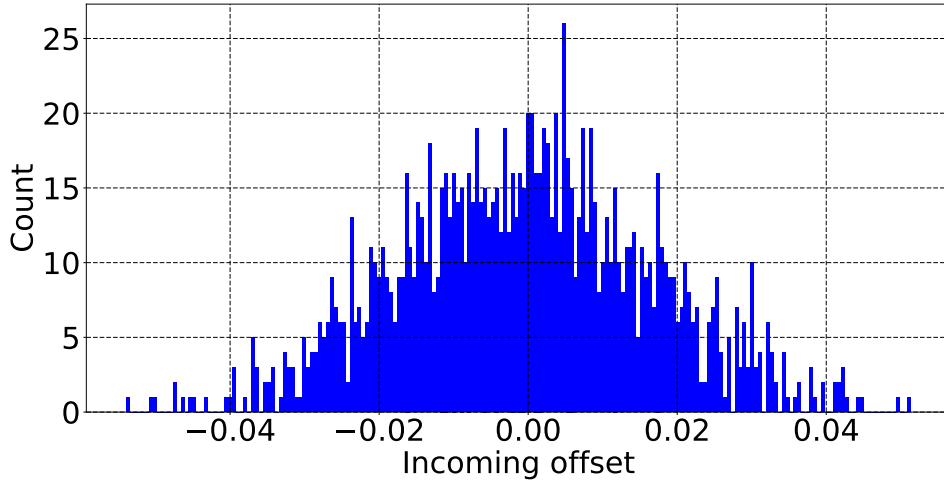


Figure 5.13: Distribution of incoming position and angle offsets from $-0.05\sigma_{x,y}$ to $0.05\sigma_{x,y}$.

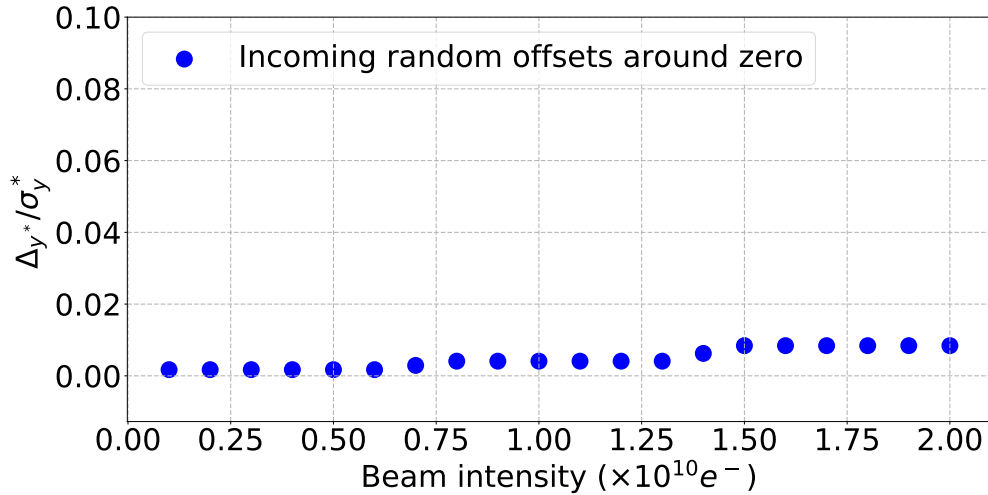


Figure 5.14: Vertical orbit deflection at the IP between the first and last bunch of a train normalised by the IP vertical beam size ($\Delta y^*/\sigma_y^*$) vs. beam intensity for a train with a random and around zero incoming vertical and horizontal position and angle offsets of between -0.05 and 0.05σ in the 250 GeV ILC BDS, calculated with PLACET with resistive wall effects included.

5.1.3.4 Impact of long-range wakefields on the luminosity

The quality of the delivered electron and positron beams is quantified by the luminosity at the IP. In order to study the impact of the previous dynamic imperfections,

one considered that the tracked electron beam was colliding with a perfectly centered positron beam coming from the positron BDS. Thus, the vertical offset between the two beams corresponds to the vertical orbit of the electron beam at the IP. The calculations were done with the code GUINEA-PIG [72]. The resulting luminosity degradation versus the relative offset of the colliding beams is shown in Fig. 5.15, where L is the calculated luminosity and $L_0 = 0.82 \times 10^{34} \text{ cm}^{-2} \text{ s}^{-1}$. The results of the impact of incoming dynamic errors in the 250 GeV ILC BDS on the luminosity are summarized in Table 5.4. At low beam intensity ($2.0 \times 10^9 e^-$) the impact of an incoming position or angle offset has a negligible impact on the luminosity. However, at high beam intensity ($2.0 \times 10^{10} e^-$), an incoming position offset of $0.1\sigma_y$ leads to a luminosity loss of 36% and an incoming angle offset of $0.1\sigma_{y'}$ leads to a luminosity loss of 75%. For a train injected with both position and angle offsets of $0.1\sigma_y$ and $0.1\sigma_{y'}$ respectively, the luminosity loss is 47%. Last but not least, a train injected with a position and angle offsets in both planes of 0.1σ leads to a luminosity loss of 64%. However, if one considers random offset around zero, it seems that the long-range wakefield kicks are compensating each other which leads to a small vertical deflection between the first bunch and the last bunch of the train at the IP, which makes it negligible.

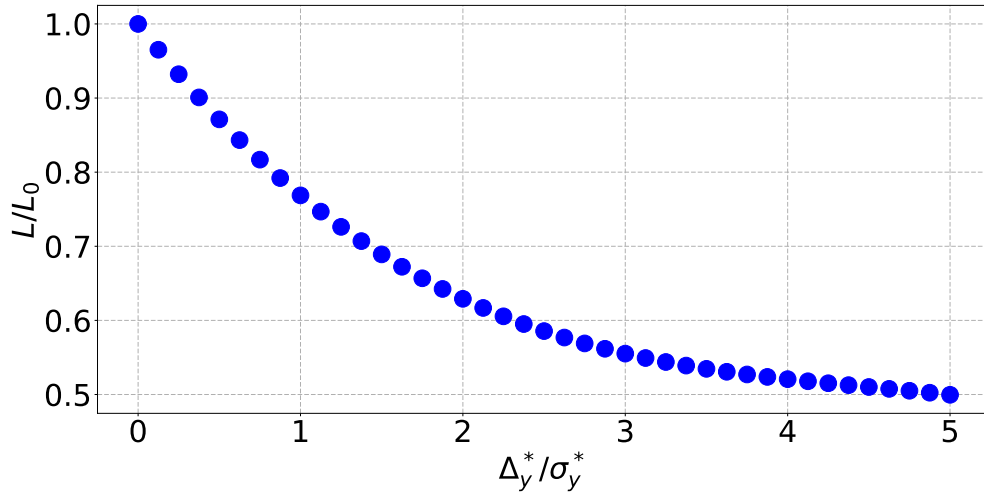


Figure 5.15: 250 GeV ILC luminosity degradation vs. relative vertical offset of the colliding beams.

Table 5.4: Impact of different incoming vertical position and angle offsets on the relative vertical offset at the IP (Δ_y^*) and the luminosity for low and high beam intensities in the 250 GeV ILC BDS.

Case	Δ_y^* [nm]	Δ_y^*/σ_y^*	\mathbf{L}/\mathbf{L}_0
Inc. position offset $0.1\sigma_y$			
$0.2 \times 10^{10} e^-$	0.013	0.002	~ 1.0
$2.0 \times 10^{10} e^-$	14.8	1.92	0.64
Inc. angle offset $0.1\sigma_{y'}$			
$0.2 \times 10^{10} e^-$	0.015	0.002	~ 1.0
$2.0 \times 10^{10} e^-$	127	16.5	0.25
Inc. offsets $0.01\sigma_y$ & $0.01\sigma_{y'}$			
$0.2 \times 10^{10} e^-$	0.039	0.005	~ 1.0
$2.0 \times 10^{10} e^-$	14.2	1.85	0.53
Inc. offsets $0.01\sigma_y$ & $0.01\sigma_{y'}$ and $0.01\sigma_x$ & $0.01\sigma_{x'}$			
$0.2 \times 10^{10} e^-$	2.77	0.36	0.87
$2.0 \times 10^{10} e^-$	32.0	4.15	0.36
Inc. random offsets around zero			
$0.2 \times 10^{10} e^-$	0.100	0.013	~ 1.0
$2.0 \times 10^{10} e^-$	0.501	0.065	0.98

5.2 ILC BDS 500 GeV

5.2.1 Beam and machine parameters

The second phase of the ILC would be an upgrade to 500 GeV center-of-mass energy. For the 500 GeV ILC, the vertical beam size at the IP is squeezed to 5.9 nm and a luminosity of $1.8 \times 10^{34} \text{ cm}^{-2}\text{s}^{-1}$ is obtained [18]. The phase advances are slightly different in the ILC 500 GeV BDS, compared to the 250 GeV one, but still around 12π between the entrance of the BDS and the IP. The phase advances and the Twiss functions are shown in Fig. 5.16. The ILC 500 GeV main parameters are summarized in Table 5.5.

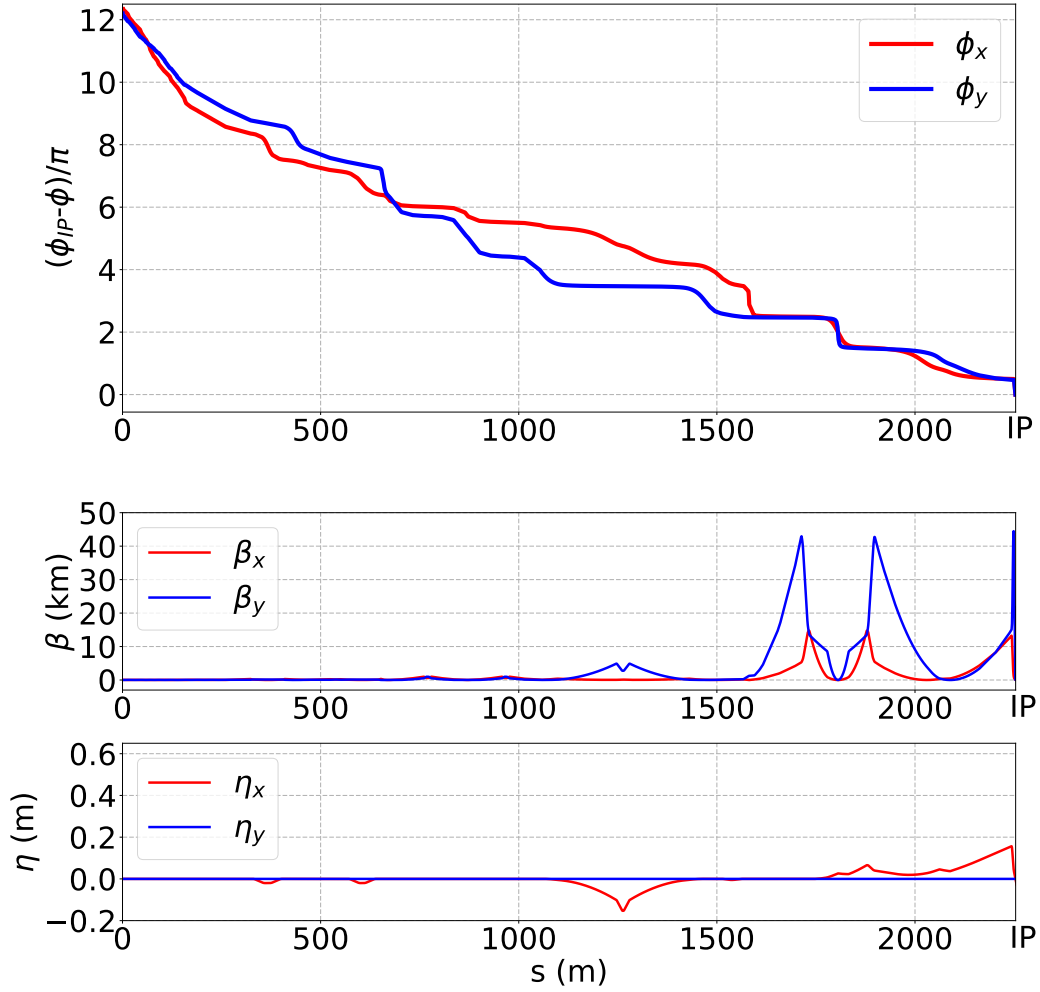


Figure 5.16: The ILC BDS 500 GeV phase advance (top) and the ILC BDS 500 GeV Twiss parameters calculated with PLACET (bottom).

Table 5.5: 500 GeV ILC beam parameters.

Parameter	Symbol	Value
Centre-of-mass energy	E_{CM}	500 GeV
Number of bunches	n_b	1312
Bunch population	N	$2.0 \times 10^{10} e^-$
RMS bunch length	σ_z	0.3 mm
Bunch separation	Δt_b	554 ns
IP RMS beam sizes	σ_x^*/σ_y^*	474/5.9 nm

5.2.2 Single-bunch simulations

5.2.2.1 Efficiency of Beam-Based Alignment corrections

The efficiency of the Beam-Based Alignment correction and knobs in the 500 GeV ILC BDS was studied with PLACET. As in the 250 GeV BDS, a Gaussian beam made of 2.0×10^{10} electrons and 30,000 macro-particles was tracked from the entrance of the ILC BDS to the IP. The simulation conditions are the same as in Section 5.1.2.1. The impact of the corrections on the particles distribution at the IP for one machine is shown in Fig. 5.17. The results of the corrections on the vertical beam size at the IP (σ_y^*) for 100 machines are shown in Fig. 5.18 and are summarized in Table 5.6.

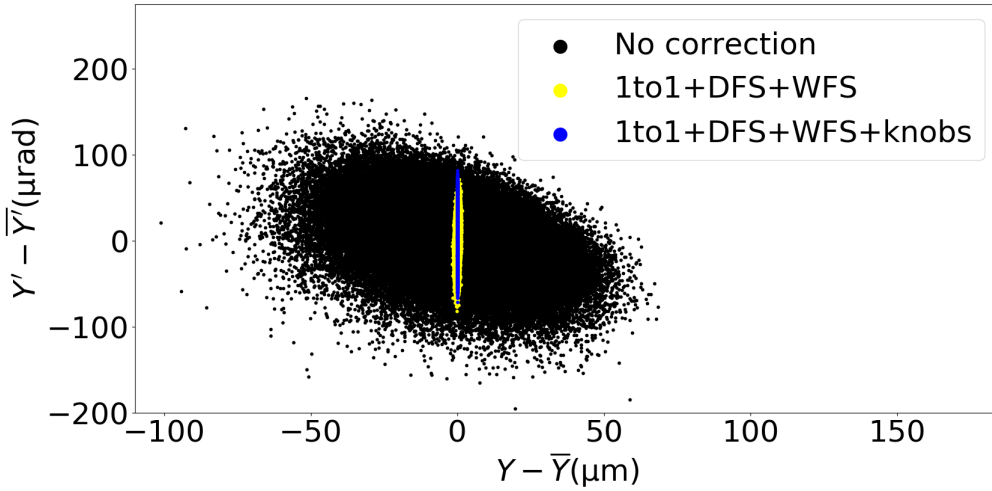


Figure 5.17: Centered vertical phase space at the 500 GeV ILC BDS IP, $Y' - \bar{Y}'$ vs. $Y - \bar{Y}$, for 3 cases: no correction, One-to-one steering, DFS, WFS and One-to-one steering, DFS, WFS and knobs, calculated with PLACET with wakefields.

Table 5.6: Impact of the corrections on the 500 GeV ILC vertical beam size at the IP (σ_y^*) for 100 machines with wakefields and $2 \times 10^{10} e^-$, simulated with PLACET.

Correction	$\bar{\sigma}_y^*$
No correction	$33.0 \pm 10.7 \mu\text{m}$
One-to-one	$7.1 \pm 2.6 \mu\text{m}$
One-to-one + DFS	$452 \pm 81 \text{ nm}$
One-to-one + DFS + WFS	$372 \pm 47 \text{ nm}$
One-to-one + DFS + WFS + knobs	$6.06 \pm 0.12 \text{ nm}$

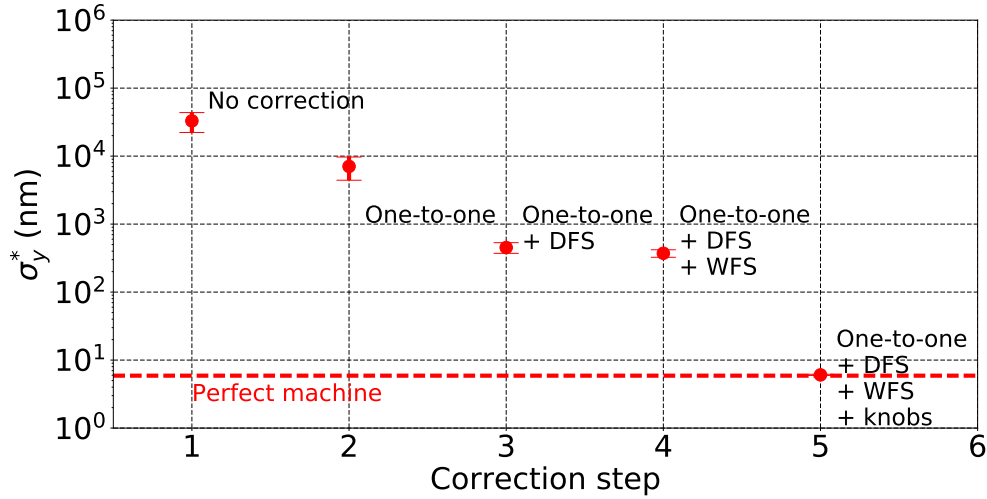


Figure 5.18: Average vertical beam size at the 500 GeV ILC IP (σ_y^*) vs. correction step: One-to-one, DFS, WFS corrections and IP tuning knobs. The red dashed line show the vertical beam size at the IP for a perfect machine, 5.9 nm.

The corrections gave really good results in the 500 GeV BDS as well. The whole procedure reduces the average vertical IP beam size for 100 machines ($\overline{\sigma_y^*}$) from $33.0 \pm 10.7 \mu\text{m}$ without any correction to $6.06 \pm 0.12 \text{ nm}$ with One-to-one, DFS, WFS and knobs, really close to the beam size in the perfect machine, 5.9 nm.

5.2.2.2 Impact of static errors

In order to study the impact of the short-range wakefields and static errors, the same simulations were done in the 500 GeV BDS. The simulation conditions are the the same as in Section 5.1.2.2. The impact of wakefields on the average vertical IP beam size σ_y^* is shown in Fig. 5.19 and summarized in Table 5.7.

Table 5.7: Intensity-dependent effects due to wakefields on the vertical IP beam size σ_y^* in the 500 GeV BDS, calculated with PLACET with wakefields.

Beam intensity	$\overline{\sigma_y^*}$ (nm)	w (nm/ $10^9 e^-$)
$0.2 \times 10^{10} e^-$	6.07 ± 0.30	
$2.0 \times 10^{10} e^-$	6.11 ± 0.30	0.04

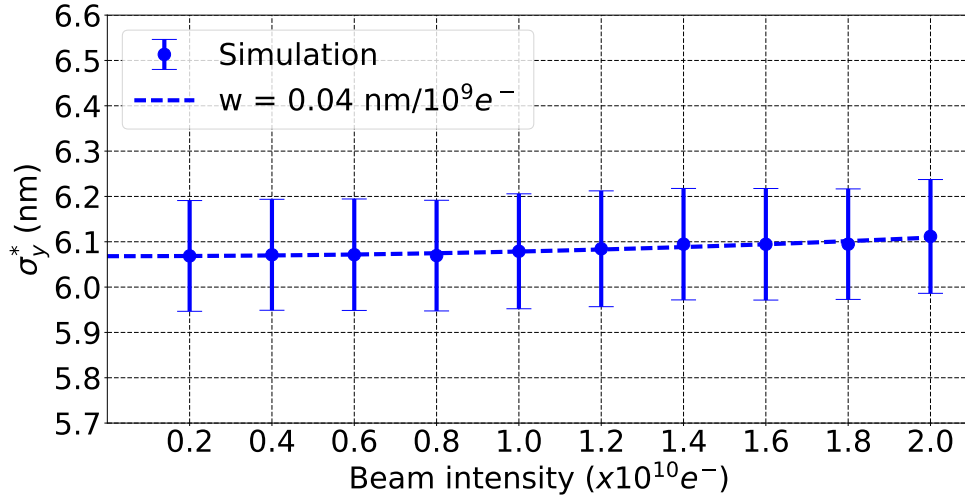


Figure 5.19: Vertical IP beam size σ_y^* vs. beam intensity in the 500 GeV BDS, calculated with PLACET with wakefields.

The beam size growth due to the short-range wakefield is also rather small in the 500 GeV BDS if one considers all C-BPMs as wakefield sources. Indeed, the growth between the vertical IP beam size at $2.0 \times 10^9 e^-$ in a bunch and $2.0 \times 10^{10} e^-$ is 0.04 nm, less than 0.7 % of the nominal beam size of 5.9 nm.

5.2.3 Multi-bunch simulations

5.2.3.1 Impact of long-range wakefields for a train with a constant incoming offset

The same multi-bunch studies were done for the 500 GeV BDS. The beam was injected with offsets of $0.01\sigma_y$, $0.05\sigma_y$ and $0.1\sigma_y$ in position and $0.1\sigma_{y'}$ in angle. In Fig. 5.20 and Fig. 5.21 are shown the vertical orbit differences between the first bunch and the last bunch of a train at the IP (Δ_{y^*}) for five different beam intensities for respectively an incoming position offset of $0.1\sigma_y$ and an incoming angle offset of $0.1\sigma_{y'}$. The impact of dynamic error is significant. Indeed, the last bunch of a train gets deflected by more than 3.1 nm for an incoming position offset of $0.1\sigma_y$ and by 32.6 nm for an incoming angle offset of $0.1\sigma_{y'}$ at $2.0 \times 10^{10} e^-$. The IP vertical orbit deflection also scales with the amplitude of the error as shown in Fig. 5.22. Figure 5.23 shows the impact of an incoming position offset of $0.1\sigma_y$ and an angle offset of $0.1\sigma_{y'}$ on the vertical orbit deflection at the IP and how it scales with the beam intensity. The last bunch of the train is deflected by $0.6\sigma_y^*$ compared to the first one at $2.0 \times 10^{10} e^-$. The impact of an incoming position offset of $0.01\sigma_x$ and an angle offset of $0.01\sigma_{x'}$ in

the horizontal plane and $0.01\sigma_y$ and $0.01\sigma_{y'}$ in the vertical plane on the vertical orbit deflection at the IP is shown in Fig. 5.24. In this case, the last bunch of the train is deflected by $1.51\sigma_y^*$ compared to the first one at $2.0 \times 10^{10} e^-$.

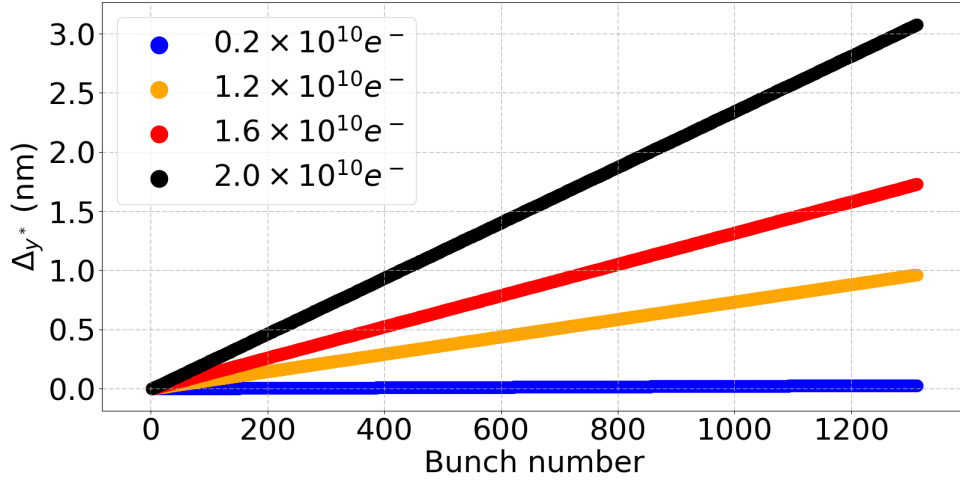


Figure 5.20: Vertical orbit deflection at the IP between the first and last bunch of a train Δy^* vs. bunch number for a train with a constant incoming position offset of $0.1\sigma_y$ of the train of bunches in the 500 GeV ILC BDS for 5 beam intensities, calculated with PLACET with resistive wall effects included.

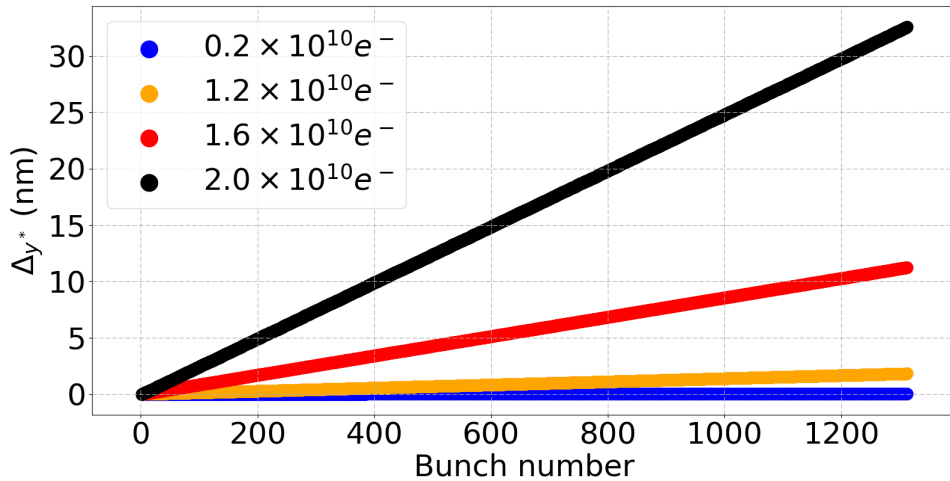


Figure 5.21: Vertical orbit deflection at the IP between the first and last bunch of a train Δy^* vs. bunch number for a train with a constant incoming angle offset of $0.1\sigma_{y'}$ of the train of bunches in the 500 GeV ILC BDS for 5 beam intensities, calculated with PLACET with resistive wall effects included.

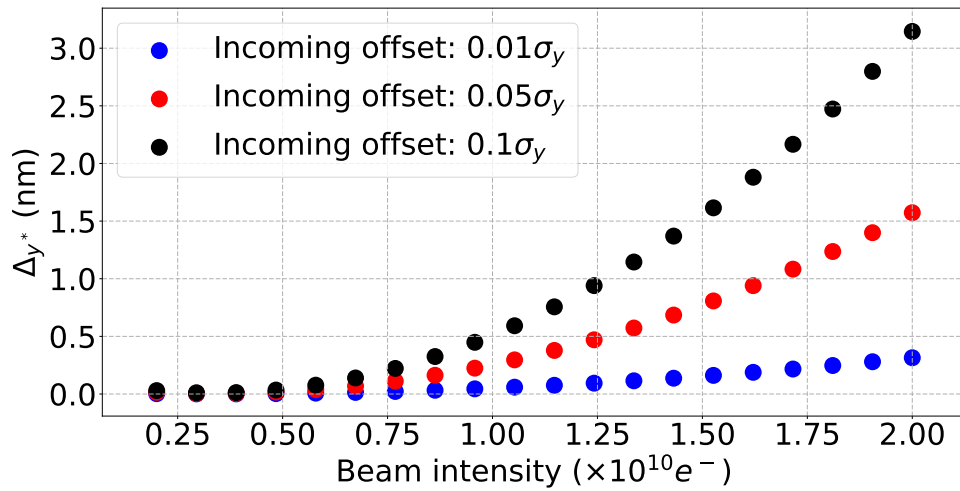


Figure 5.22: Vertical orbit deflection at the IP between the first and last bunch of a train Δy^* vs. beam intensity for three incoming constant position offsets of the train of bunches in the 500 GeV ILC BDS: $0.01\sigma_y$, $0.05\sigma_y$ and $0.1\sigma_y$, calculated with PLACET with resistive wall effects included.

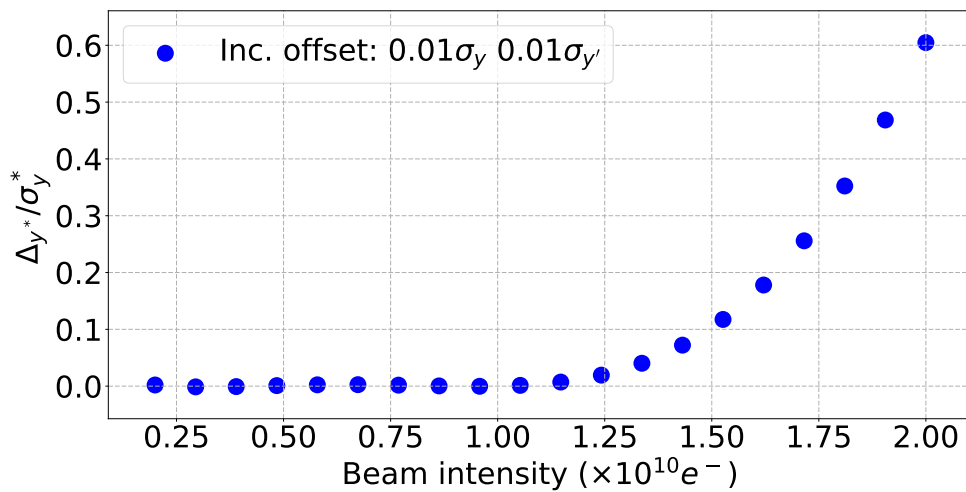


Figure 5.23: Vertical orbit deflection at the IP between the first and last bunch of a train normalised by the IP vertical beam size ($\Delta y^*/\sigma_y^*$) vs. beam intensity for a train with incoming constant position and angle offsets of respectively $0.01\sigma_y$ and $0.01\sigma_{y'}$ in the 500 GeV ILC BDS, calculated with PLACET with resistive wall effects included.

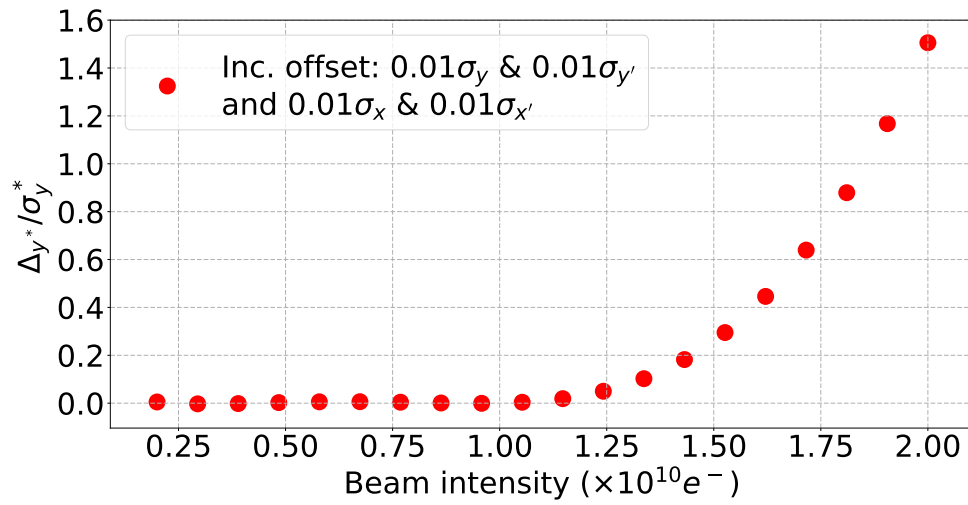


Figure 5.24: Vertical orbit deflection at the IP between the first and last bunch of a train normalised by the IP vertical beam size ($\Delta y^*/\sigma_y^*$) vs. beam intensity for a train with incoming constant horizontal position and angle offsets of respectively $0.01\sigma_x$ and $0.01\sigma_{x'}$ and vertical incoming position and angle offsets of respectively $0.01\sigma_y$ and $0.01\sigma_{y'}$ in the 500 GeV ILC BDS, calculated with PLACET with resistive wall effects included.

5.2.3.2 Impact of long-range wakefields for a train with random incoming offset

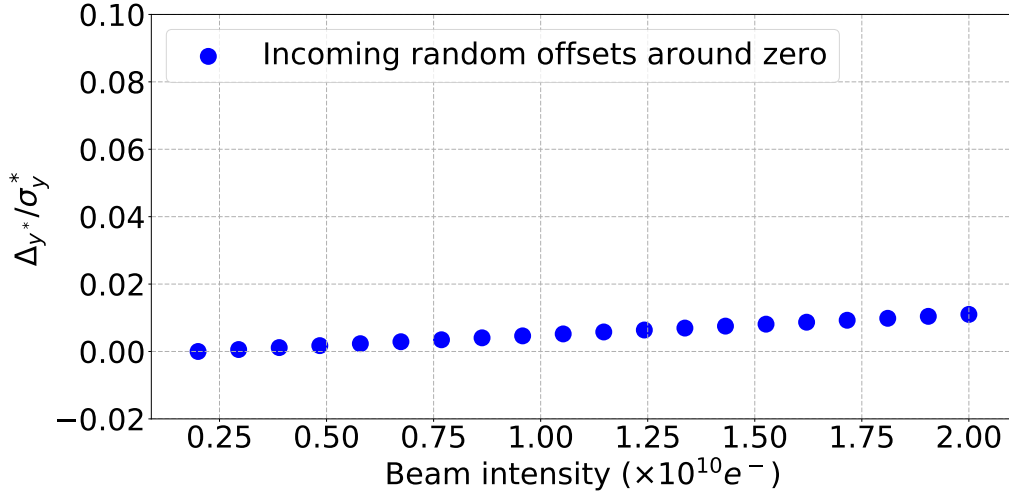


Figure 5.25: Vertical orbit deflection at the IP between the first and last bunch of a train normalised by the IP vertical beam size ($\Delta y^*/\sigma_y^*$) vs. beam intensity for a train with a random and around zero incoming vertical and horizontal position and angle offsets of between -0.05 and 0.05σ in the 500 GeV ILC BDS, calculated with PLACET with resistive wall effects included.

As in the 250 GeV BDS, in order to study the impact of a train with random jitter, the incoming consecutive 1312 bunches were injected with normally distributed offsets between -5% and 5% with an average of zero [71]. The resulting vertical orbit deflection between the first and last bunch is shown in Fig. 5.25. The last bunch of a train is deflected by $0.003 \sigma_y^*$, or 0.015 nm, which is negligible compared to the beam size of 5.9 nm.

5.2.3.3 Impact of long-range wakefields on the luminosity

As in the 250 GeV BDS, the previously studied electron beam was collided with a perfectly centered positron beam coming from the positron BDS. The resulted luminosity degradation versus the relative offset of the colliding beams is shown in Fig. 5.26, where $L_0 = 1.8 \times 10^{34} \text{ cm}^{-2} \text{ s}^{-1}$. The results of the impact of incoming dynamic errors in the 500 GeV ILC BDS on the luminosity are summarized in Table 5.8. As in the 250 GeV BDS, at low beam intensity ($2.0 \times 10^9 e^-$) the impact of an incoming position or angle offset has a negligible impact on the luminosity. However, at high beam intensity ($2.0 \times 10^{10} e^-$), an incoming position offset of $0.1\sigma_y$ leads to

a luminosity loss of 18% and an incoming angle offset of $0.1\sigma_{y'}$ leads to a luminosity loss of 68%. For a train injected with both position and angle offsets of $0.1\sigma_y$ and $0.1\sigma_{y'}$ respectively, the luminosity loss is 20%. Last but not least, a train injected with a position and angle offsets in both planes of 0.1σ leads to a luminosity loss of 41%. In the ILC 500 GeV BDS, the impact of incoming random offsets around zero is also negligible. Thus, the deflection of one bunch in the train between the entrance of the BDS and the IP is rather small, 0.06 nm in this case. The resulting luminosity loss is then negligible.

Those results are obtained if no correction is applied. In the ILC, the bunch separation is large, so, in reality, such a position drift at the IP could be compensated with an intra-train feedback, diminishing its effects on the luminosity.

In conclusion, the intensity-dependent effects due to short-range wakefields are negligible in both the 250 and 500 GeV ILC BDS. The intensity-dependent parameter is around $0.04 \text{ nm}/10^9 e^-$ for both energies, representing an increase on the vertical beam size at the IP of 0.03 nm and 0.04 nm for 250 GeV and 500 GeV respectively. However, the intensity-dependent effects due to long-range wakefields have a significant impact on the luminosity. Indeed, at $2.0 \times 10^{10} e^-$, the impact of incoming vertical and horizontal position offsets of $0.01\sigma_y$ and $0.01\sigma_x$, respectively, and incoming vertical and horizontal angle offsets of $0.01\sigma_{y'}$, $0.01\sigma_{x'}$, respectively leads to a luminosity loss of 64% in the 250 GeV BDS and of 41% in the 500 GeV BDS.

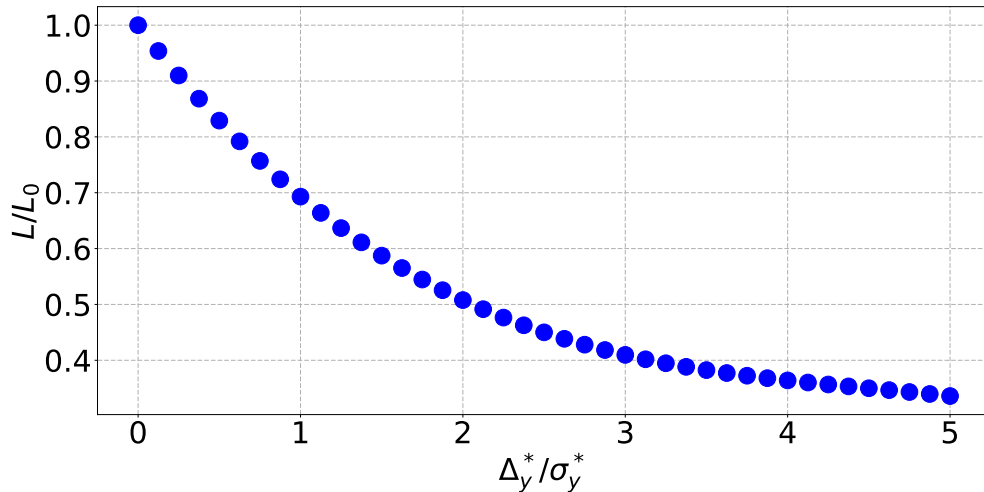


Figure 5.26: 500 GeV ILC BDS luminosity degradation vs. relative vertical offset of the colliding beams.

Table 5.8: Impact of different incoming vertical position and angle offsets on the relative vertical offset Δ_y^* at the IP and the luminosity for low and high beam intensities in the ILC BDS 500 GeV.

Case	Δ_y^* [nm]	Δ_y^*/σ_y^*	\mathbf{L}/\mathbf{L}_0
Inc. position offset $0.1\sigma_y$			
$0.2 \times 10^{10} e^-$	0.028	0.005	~ 1.0
$2.0 \times 10^{10} e^-$	3.08	0.522	0.82
Inc. angle offset $0.1\sigma_{y'}$			
$0.2 \times 10^{10} e^-$	0.0178	0.003	~ 1.0
$2.0 \times 10^{10} e^-$	32.57	5.52	0.32
Inc. offsets $0.01\sigma_y$ & $0.01\sigma_{y'}$			
$0.2 \times 10^{10} e^-$	0.012	0.002	~ 1.0
$2.0 \times 10^{10} e^-$	3.54	0.6	0.80
Inc. offsets $0.01\sigma_y$ & $0.01\sigma_{y'}$ and $0.01\sigma_x$ & $0.01\sigma_{x'}$			
$0.2 \times 10^{10} e^-$	0.03	0.005	~ 1.0
$2.0 \times 10^{10} e^-$	8.91	1.51	0.59
Inc. random offsets around zero			
$0.2 \times 10^{10} e^-$	0.01	0.002	~ 1.0
$2.0 \times 10^{10} e^-$	0.06	0.01	~ 1.0

However, the bunch separation is large in the ILC, thus the bunch-to-bunch position and angle offsets caused by dynamic effects can be corrected with intra-train IP position and angle feedback corrections. They are applied using a stripline kicker located near the IP. The impact of such a system was studied and the conclusions are reassuring, it can recover more than 90% of the luminosity [43, 73].

Chapter 6

Intensity-dependent effects in the CLIC BDS

6.1 CLIC 380 GeV BDS

The CLIC 380 GeV center-of-mass energy stage would be the first stage of CLIC. The Twiss functions and the CLIC BDS 380 GeV main parameters are shown in Fig. 6.1 and Table 6.1. The main differences between the ILC and CLIC BDS for the wakefield studies are the bunch population, 4 times smaller, the bunch length, 4.3 times smaller and the bunch separation, 1108 times smaller. The CLIC BDS final focus system is also based on the local chromaticity correction seen in Section 2.1.3.

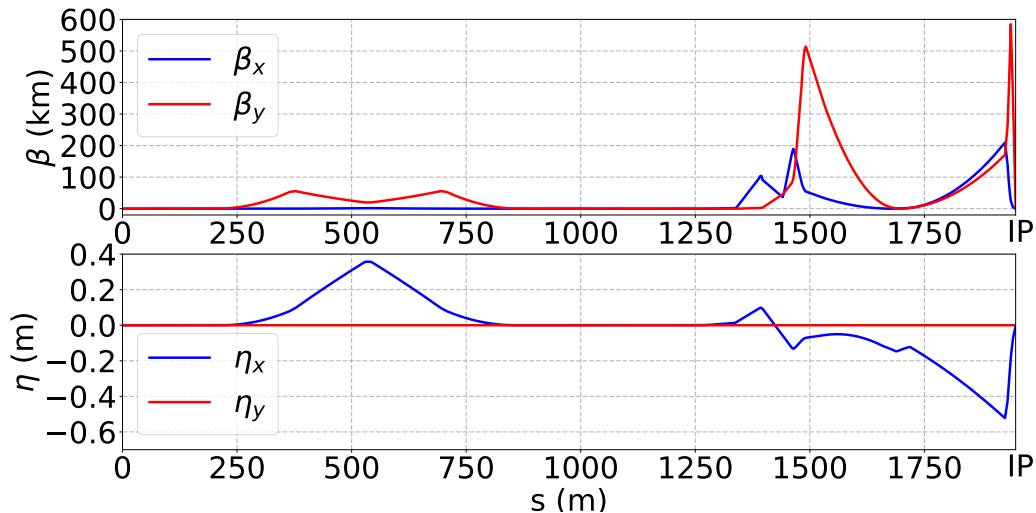


Figure 6.1: CLIC BDS 380 GeV Twiss parameters calculated with PLACET.

As in the ILC BDS, the phase advance in CLIC is a key parameter for the wakefield studies. The vertical and horizontal phase advances in the CLIC 380 GeV BDS are

shown in Fig. 6.2. The vertical phase advance between the entrance of the BDS and the IP is 12π as in the ILC.

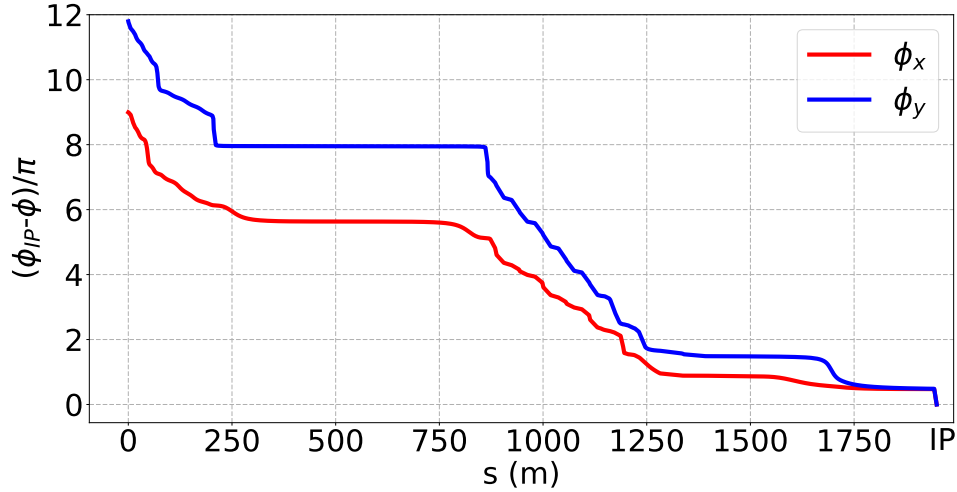


Figure 6.2: CLIC BDS 380 GeV phase advance.

Table 6.1: CLIC 380 GeV beam parameters.

Parameter	Symbol	Value
Centre-of-mass energy	E_{CM}	380 GeV
Length of the BDS	L_{BDS}	1949 m
Number of bunches	n_b	352
Bunch population	N	$5.2 \times 10^9 e^-$
RMS bunch length	σ_z	70 μm
Bunch separation	Δt_b	0.5 ns
IP RMS beam sizes	σ_x^*/σ_y^*	149/2.9 nm

6.1.1 Single-bunch simulations

6.1.1.1 Efficiency of base based alignment corrections

As for the ILC BDS, the effect of the Beam-Based Alignment correction and knobs in the CLIC BDS was studied with PLACET. A Gaussian beam comprising 5.2×10^9 electrons and 30,000 macro-particles was tracked from the entrance of the CLIC BDS to the IP. The 134 BPMs used in CLIC are X-band BPMs [74]. The positions of the CLIC BPMs are listed in Appendix C and their geometry is shown in Fig. 6.3. The

wakepotential of these BPMs was calculated using GdfidL for a 70 μm long bunch and is shown in Fig. 6.4. For the static imperfections in the CLIC BDS, the following number were taken into account: misalignment and roll error of quadrupoles, BPMs and sextupoles by respectively 50 μm RMS and 200 μrad RMS and quadrupole, sextupole strength error of 1.0×10^{-4} . This is larger to the ones considered in the FFS [75] since aligning the BPMs and magnets in the whole BDS would be harder [76]. 100 machines were studied and the same corrections as in ATF2 were applied: One-to-one, DFS, and the following knobs: $\langle y, x' \rangle$, $\langle y, y' \rangle$, $\langle y, E \rangle$ and $\langle y, x' \times x' \rangle$, $\langle y, x' \times y' \rangle$, $\langle y, x' \times E \rangle$. Those corrections use a slightly different technique than the one used in ATF2 or in ILC. Indeed, in CLIC, all quadrupole magnets and BPMs would be on movers. Thus, the orbit correction would be based on moving the magnets and the BPMs and not by changing the strength of steering magnets [77]. Hence, if the beam travels through the center of a quadrupole it experiences no dipolar kick and thus the downstream trajectory remains unchanged if the strength of the quadrupole magnets is changed. The beam can then be centered in the quadrupole by finding a position where changing the strength of the quadrupole gives a minimum difference in beam position at a downstream BPM. Ideally there should not be any other magnetic elements between the quadrupole and the closest downstream BPM.

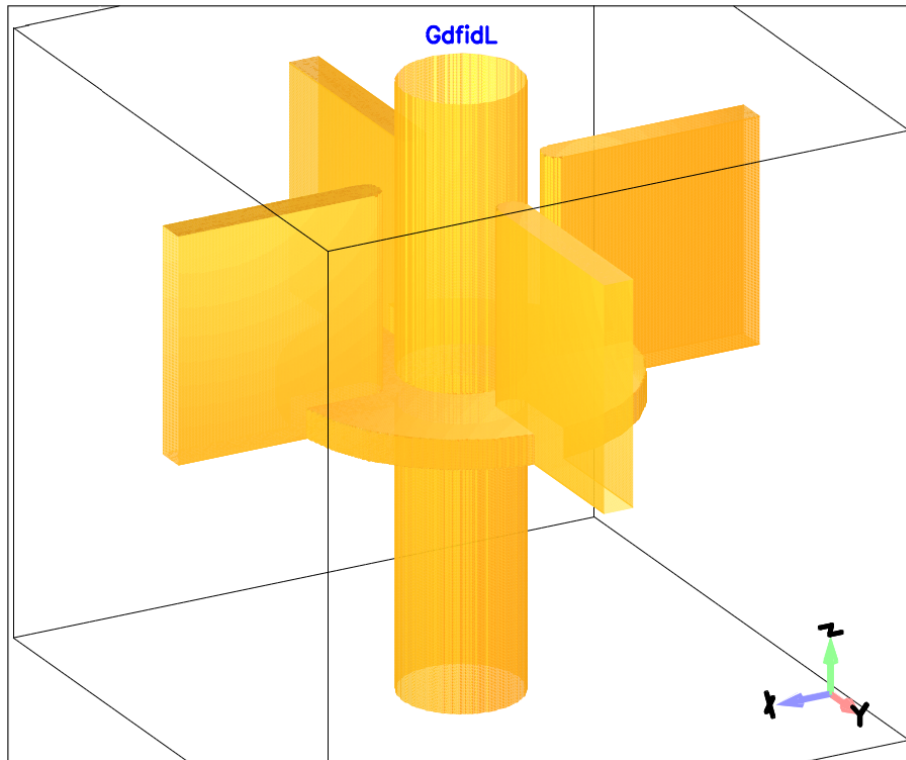


Figure 6.3: Geometry of the CLIC C-BPM, generated with GdfidL.

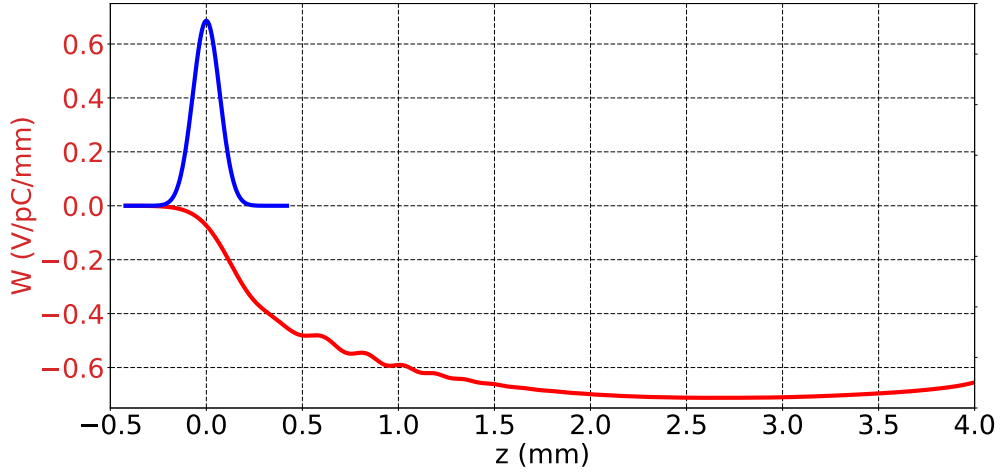


Figure 6.4: Transverse wakepotential in V/pC/mm of the CLIC C-BPM, calculated with GdfidL for a vertical offset of 1 mm, Gaussian bunch length of 70 μm and 1 pC charge (in red). For reference, the distribution of the electrons in one bunch is shown (in blue).

The impact of the corrections on the particles distribution at the IP for one machine is shown in Fig. 6.5. The results of the corrections on the vertical beam size at the IP (σ_y^*) for 100 machines are shown in Fig. 6.6 and are summarized in Table 6.2.

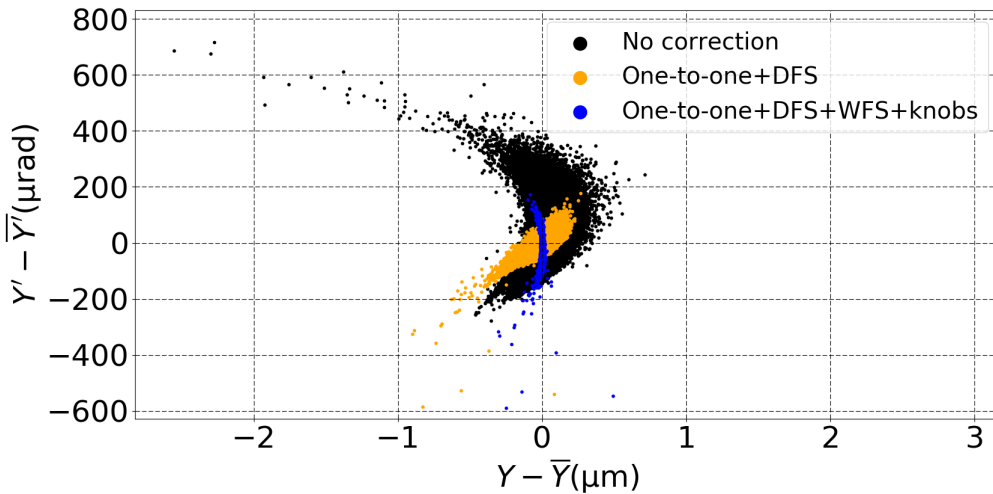


Figure 6.5: Centered vertical phase space at the 380 GeV CLIC BDS IP, $Y' - \bar{Y}'$ vs. $Y - \bar{Y}$, for 3 cases: no correction, One-to-one steering, DFS, WFS and One-to-one steering, DFS, WFS and knobs, calculated with PLACET with wakefields.

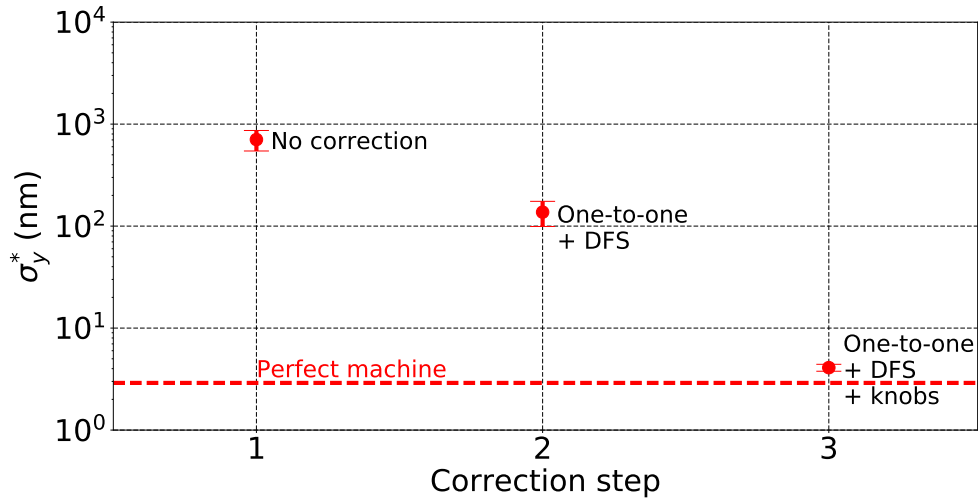


Figure 6.6: Average vertical beam size at the 380 GeV CLIC IP (σ_y^*) vs. correction step: One-to-one, DFS, WFS corrections and IP tuning knobs. The red dashed line show the vertical beam size at the IP for a perfect machine, 2.9 nm, calculated with PLACET with wakefields.

Table 6.2: Impact of the corrections on the CLIC 380 GeV vertical beam size at the IP (σ_y^*) for 100 machines with wakefields and with a beam intensity of $5.2 \times 10^9 e^-$, calculated with PLACET with wakefields.

Correction	$\overline{\sigma_y^*}$
No correction	706 ± 160 nm
One-to-one + DFS	$137 \pm 38,0$ nm
One-to-one + DFS + knobs	4.82 ± 0.570 nm

The average vertical IP beam size for 100 machines is decreased after each correction. One-to-one and DFS corrections reduce the average vertical IP beam size for 100 machines $\overline{\sigma_y^*}$ from 706 ± 161 μm without any correction to 137 ± 38 . Then, the IP knobs squeeze $\overline{\sigma_y^*}$ to 4.10 ± 0.32 nm. In comparison, the vertical IP beam size in a perfect machine is 2.9 nm.

6.1.1.2 Impact of static errors

The impact of static errors were simulated in the CLIC 380 GeV BDS the same way as was done in ATF2 and in the ILC BDS. The following simulation conditions were used with PLACET: misalignment and roll error of quadrupoles, BPMs and sextupoles by respectively 50 μm RMS and 200 μrad RMS and quadrupoles, sextupoles strength

error of 1.0×10^{-4} . 100 machines were studied and the following corrections were applied: One-to-one, DFS, and the following knobs: $\langle y, x' \rangle$, $\langle y, y' \rangle$, $\langle y, E \rangle$ and $\langle y, x' \times x' \rangle$, $\langle y, x' \times y' \rangle$, $\langle y, x' \times E \rangle$. This was done for intensities between $5.2 \times 10^8 e^-$ and $5.2 \times 10^9 e^-$ in order to show the intensity-dependent effects. The impact of wakefields on the average vertical IP beam size σ_y^* is shown in Fig. 6.7 and summarized in Table 6.3. The beam size growth due to the short-range wakefield is larger than in the ILC BDS if one considers all CLIC BPMs as wakefield sources. Indeed, at $5.2 \times 10^8 e^-$ bunch charge, the growth between the vertical IP beam size and $5.2 \times 10^9 e^-$ is 0.47 nm, around 9.8 %. This is due to the fact that the 134 CLIC C-BPMs have a wakepotential peak of 0.71 V/pC/mm compared to 0.16 V/pC/mm for the 101 ILC C-BPMs. In reality, a bunch train is made of 352 bunches is traveling in the CLIC BDS, hence one also has to take into account long-range wakefield effects.

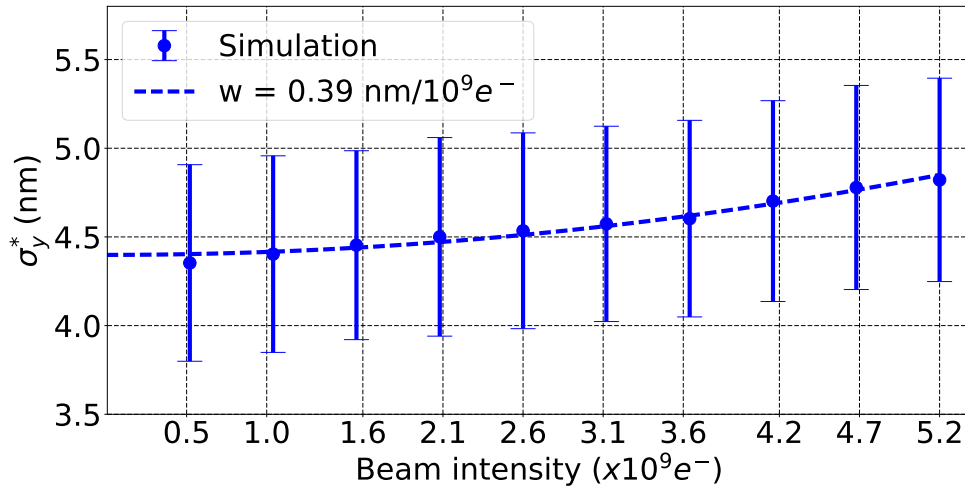


Figure 6.7: Vertical IP beam size σ_y^* vs. beam intensity in the 380 GeV BDS, calculated with PLACET with wakefields.

Table 6.3: Intensity-dependent effects due to wakefields on the vertical IP beam size (σ_y^*) in the 380 GeV BDS, calculated with PLACET with wakefields.

Beam intensity	$\overline{\sigma_y^*}$ (nm)	w (nm/ $10^9 e^-$)
$5.2 \times 10^8 e^-$	4.35 ± 0.55	0.39
$5.2 \times 10^9 e^-$	4.82 ± 0.57	

6.1.2 Multi-bunch simulations

6.1.2.1 Impact of long-range wakefields for a train with a constant incoming offset

In order to study the impact of the long-range wakefields in the CLIC BDS, the wakepotential due to resistive walls was calculated using Eq. 5.1. The CLIC BDS copper coated beam pipe has an aperture between 15 mm and 74.5 mm. The CLIC BDS beam aperture profile is shown in Fig. 6.8 [78].

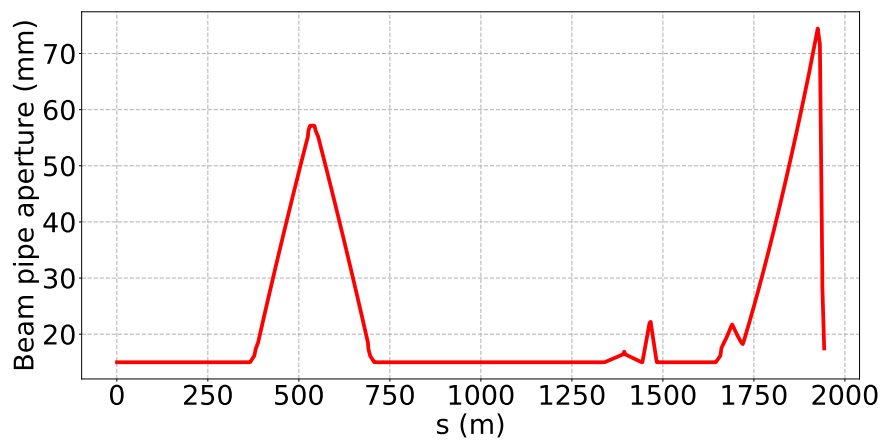


Figure 6.8: The CLIC BDS beam aperture profile.

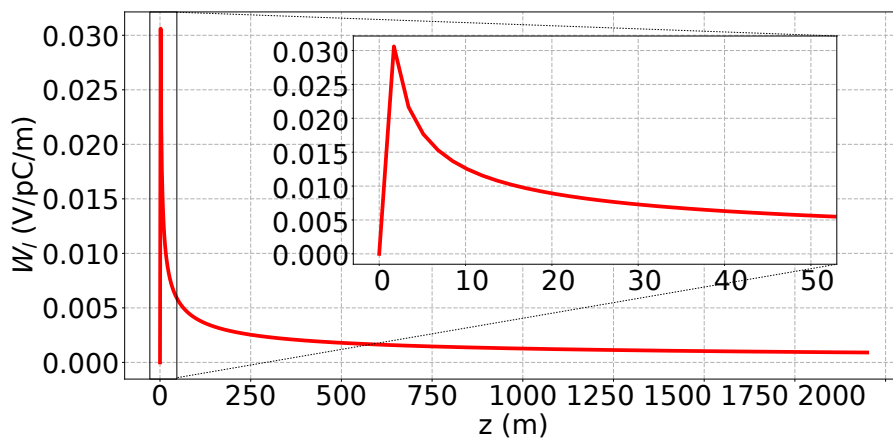


Figure 6.9: The CLIC resistive walls wakepotential for a copper beam pipe with a constant radius of 15 mm for the length of the CLIC BDS (~ 1949 m). The zoom shows the wakepotential for the length of a train (~ 52.8 m).

In the CLIC BDS, the bunch separation is 0.5 ns and there are 352 consecutive bunches. Thus, the length of the bunch train is 52.8 m. In Fig. 6.9 is shown the calculated wakepotential for the CLIC BDS resistive walls, considering a copper beam pipe and a beam pipe radius of 15 mm for the length of a train (~ 53 m) and for the length of the CLIC BDS (~ 1949 m).

The same multi-bunch studies were done for the CLIC 380 GeV BDS. Initial offsets of $0.01\sigma_y$, $0.05\sigma_y$ and $0.1\sigma_y$ in position and $0.1\sigma_{y'}$ in angle were considered [76]. In Fig. 6.10 and Fig. 6.11 are shown the vertical orbit difference (Δ_{y^*}) between the first bunch and the last bunch of a train at the IP for five different beam intensities for respectively an incoming position offset of $0.1\sigma_y$ and an incoming angle offset of $0.1\sigma_{y'}$. The conclusion is that the impact of long-range wakefields is significant in the CLIC BDS as well. Indeed, the last bunch of a train gets deflected by 2.79 nm for an incoming position offset of $0.1\sigma_y$ and by 1.71 nm for an incoming angle offset of $0.1\sigma_{y'}$ at $5.2 \times 10^9 e^-$. The orbit deflection increases linearly with the bunch number. The IP vertical orbit deflection also scales with the amplitude of the error as shown in Fig. 6.12. An incoming train with an incoming position offset of $0.01\sigma_y$ leads to a vertical orbit deflection at the IP of 0.28 nm. Figure 6.13 shows the impact of an incoming position offset of $0.1\sigma_y$ and an angle offset of $0.1\sigma_{y'}$ on the vertical orbit deflection at the IP and how it scales with the beam intensity.

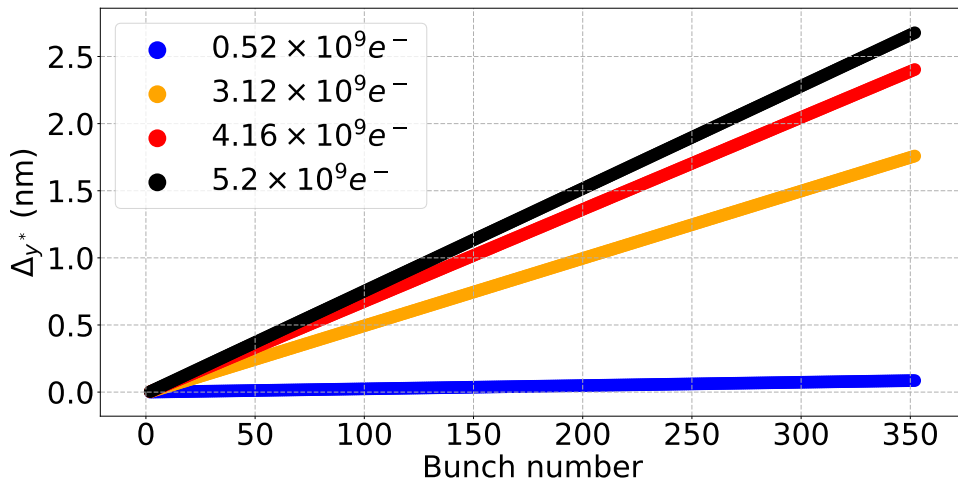


Figure 6.10: Vertical orbit deflection at the IP between the first and last bunch of a train Δ_{y^*} vs. bunch number for a train with a constant incoming position offset of $0.1\sigma_y$ of the train of bunches in the 380 GeV CLIC BDS, calculated with PLACET with resistive walls.

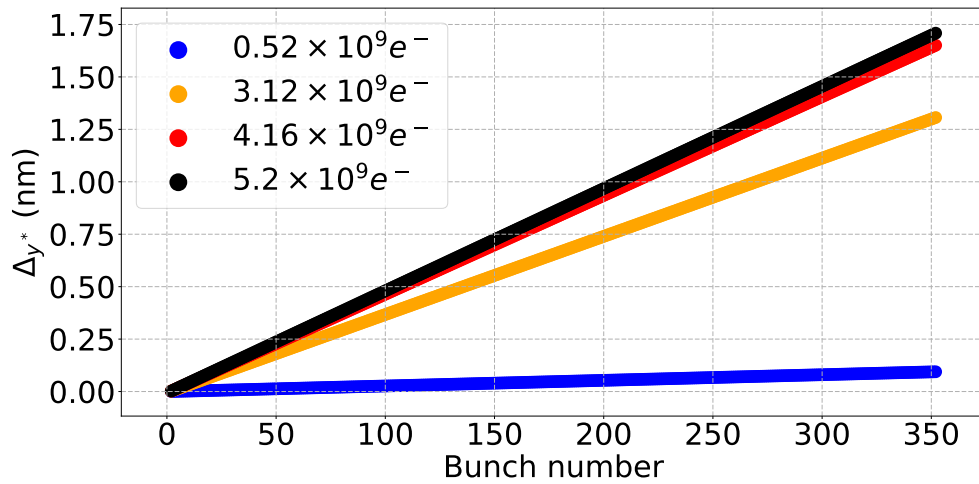


Figure 6.11: Vertical orbit deflection at the IP between the first and last bunch of a train Δy^* vs. bunch number for a train with a constant incoming angle offset of $0.1\sigma_y$ of the train of bunches in the 380 GeV CLIC BDS, calculated with PLACET with resistive walls.

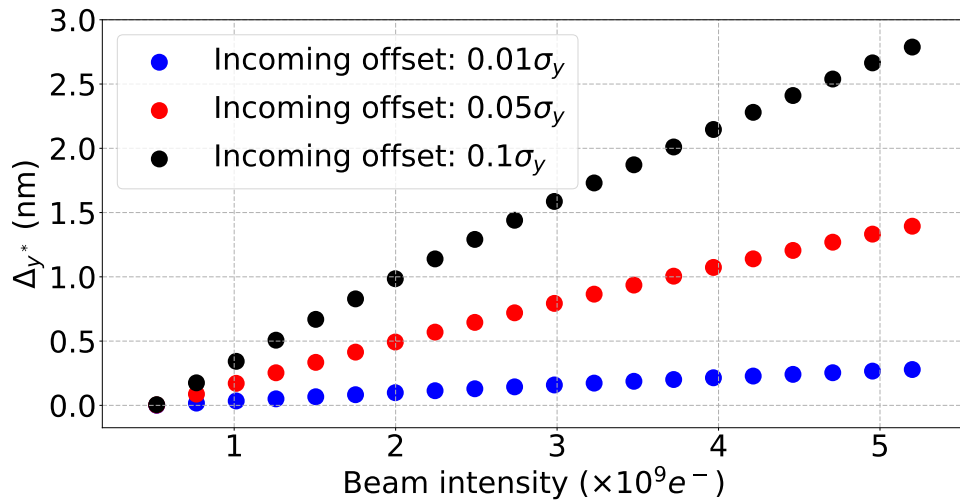


Figure 6.12: Vertical orbit deflection at the IP between the first and last bunch of a train Δy^* vs. beam intensity for three incoming constant position offsets of the train of bunches in the 380 GeV CLIC BDS: $0.01\sigma_y$, $0.05\sigma_y$ and $0.1\sigma_y$, calculated with PLACET with resistive walls.

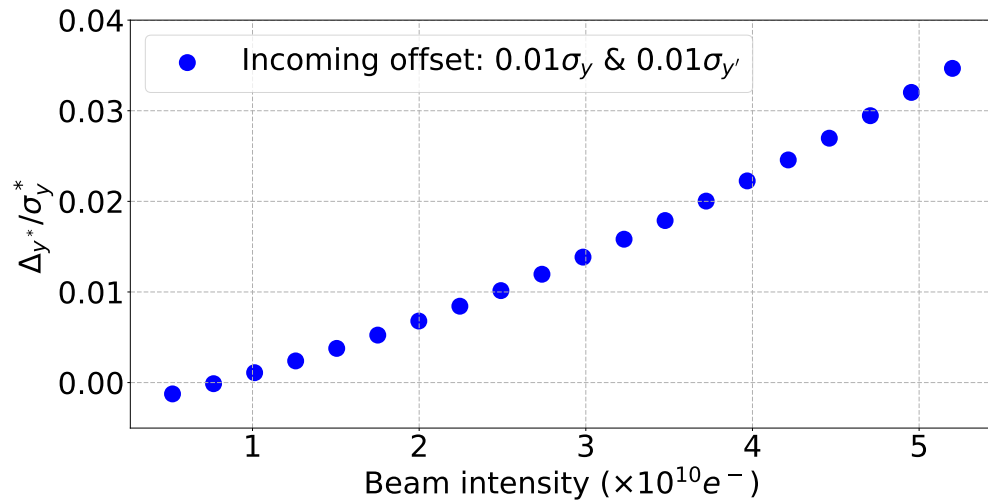


Figure 6.13: Vertical orbit deflection at the IP between the first and last bunch of a train normalised by the IP vertical beam size ($\Delta y^*/\sigma_y^*$) vs. beam intensity for a train with incoming constant horizontal position and angle offsets of respectively $0.01\sigma_x$ and $0.01\sigma_{x'}$ and vertical incoming position and angle offsets of respectively $0.01\sigma_y$ and $0.01\sigma_{y'}$ in the 380 GeV BDS, calculated with PLACET with resistive walls.

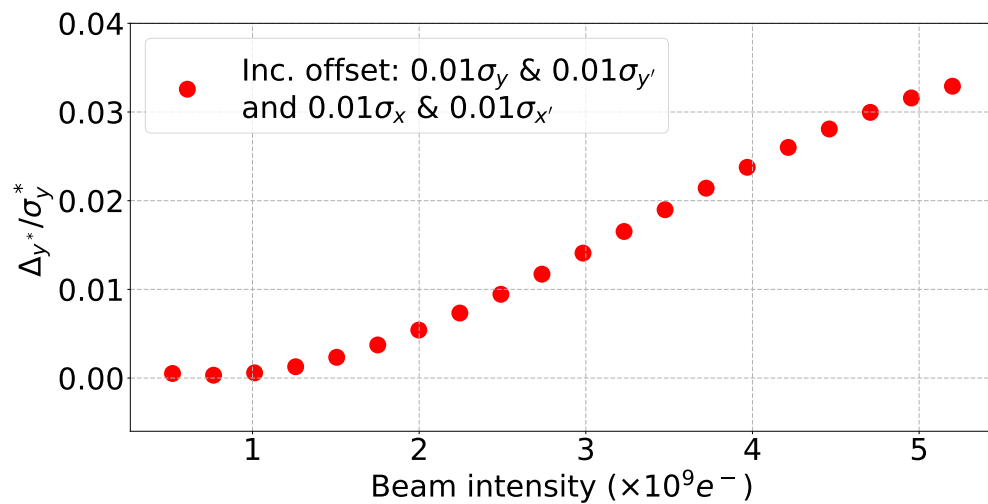


Figure 6.14: Vertical orbit deflection at the IP between the first and last bunch of a train normalised by the IP vertical beam size ($\Delta y^*/\sigma_y^*$) vs. beam intensity for a train with incoming constant horizontal position and angle offsets of respectively $0.01\sigma_x$ and $0.01\sigma_{x'}$ and vertical incoming position and angle offsets of respectively $0.01\sigma_y$ and $0.01\sigma_{y'}$ in the 380 GeV CLIC BDS, calculated with PLACET with resistive walls.

6.1.2.2 Impact of long-range wakefields for a train with random incoming offset

As in the ILC BDS, in order to study the impact of a train with random jitter, the incoming consecutive 352 bunches are injected with normally distributed position and angle offsets between -5% and 5% with an average of zero. The distribution of the incoming offsets is shown in Fig. 5.13. The resulting vertical orbit deflection between the first and last bunch is shown in Fig. 6.15. The effects of random incoming offsets lead to kicks compensating each other inside the CLIC BDS, resulting in a small orbit deflection at the IP. The last bunch of a train is deflected by $0.005 \sigma_y^*$, or 0.015 nm, which is negligible compared to the beam size of 2.9 nm.

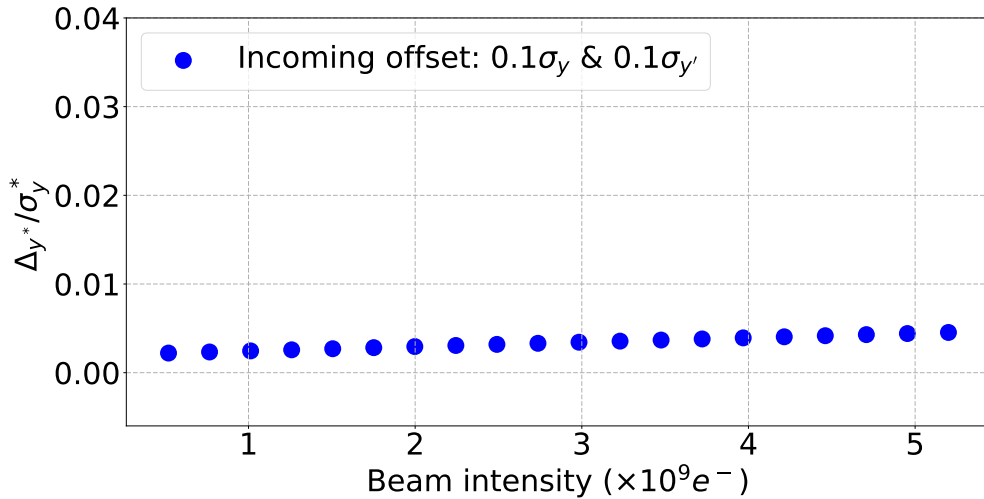


Figure 6.15: Vertical orbit deflection at the IP between the first and last bunch of a train normalised by the IP vertical beam size ($\Delta y^*/\sigma_y^*$) vs. beam intensity for a train with a random and around zero incoming vertical and horizontal position and angle offsets of between -0.05 and 0.05 σ in the 380 GeV CLIC BDS, calculated with PLACET with resistive walls.

6.1.2.3 Impact of long-range wakefields on the luminosity

As in the ILC BDS, the previously studied electron beam was collided with a perfectly centered positron beam coming from the positron BDS. The resulted luminosity degradation versus the relative offset of the colliding beams is shown in Fig. 6.16, where L is the calculated luminosity and $L_0 = 1.5 \times 10^{34} \text{ cm}^{-2} \text{ s}^{-1}$ [23]. The results of the impact of incoming dynamic errors in the 380 GeV CLIC BDS on the luminosity are summarized in Table 6.4. At low beam intensity ($0.52 \times 10^9 e^-$) the impact of an

incoming position or angle offset has a negligible impact on the luminosity. However, at high beam intensity ($5.2 \times 10^9 e^-$), an incoming position offset of $0.1\sigma_y$ leads to a luminosity loss of 16% and an incoming angle offset of $0.1\sigma_{y'}$ leads to a luminosity loss of 9%. For a train injected with both position and angle offsets of $0.1\sigma_y$ and $0.1\sigma_{y'}$ respectively, the luminosity loss is negligible. A train injected with a position and angle offsets in both planes of 0.1σ leads as well to a negligible luminosity loss. In the CLIC 380 GeV BDS, the impact of incoming random offsets around zero is also negligible due to consecutive bunches kicking in opposite directions, making the sum of all those kicks close to zero. Thus, the deflection of one bunch in the train between the entrance of the BDS and the IP is rather small, 0.015 nm in this case. The resulting luminosity loss is then negligible. Those results were obtained if no correction is applied. As in the ILC, such a position drift at the IP could be compensated with an intra-train feedback, diminishing its effects on the luminosity [79, 80].

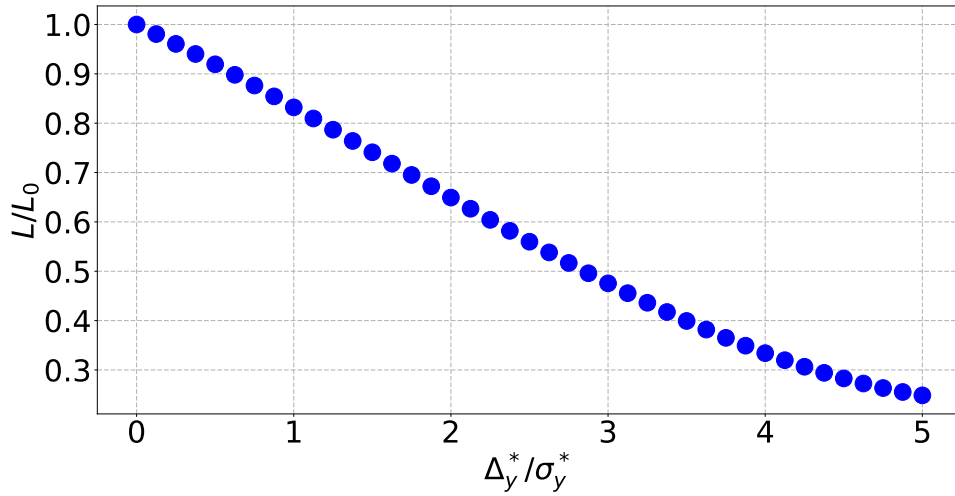


Figure 6.16: CLIC 380 GeV BDS luminosity degradation vs. relative vertical offset of the colliding beams.

Table 6.4: Impact of different incoming vertical position and angle offsets on the relative vertical offset Δ_y^* at the IP and the luminosity for low and high beam intensities in the CLIC 380 GeV BDS.

Case	Δ_y^* [nm]	Δ_y^*/σ_y^*	\mathbf{L}/\mathbf{L}_0
Inc. position offset $0.1\sigma_y$			
$0.52 \times 10^9 e^-$	0.006	0.002	~ 1.0
$5.2 \times 10^9 e^-$	2.79	0.96	0.84
Inc. angle offset $0.1\sigma_{y'}$			
$0.52 \times 10^9 e^-$	0.002	0.001	~ 1.0
$5.2 \times 10^9 e^-$	1.71	0.59	0.91
Inc. offsets $0.01\sigma_y$ & $0.01\sigma_{y'}$			
$0.52 \times 10^9 e^-$	0.003	0.001	~ 1.0
$5.2 \times 10^9 e^-$	0.087	0.03	~ 1.0
Inc. offsets $0.01\sigma_y$ & $0.01\sigma_{y'}$ and $0.01\sigma_x$ & $0.01\sigma_{x'}$			
$0.52 \times 10^9 e^-$	0.003	0.001	~ 1.0
$5.2 \times 10^9 e^-$	0.087	0.03	~ 1.0
Inc. random offsets around zero			
$0.52 \times 10^9 e^-$	0.006	0.002	~ 1.0
$5.2 \times 10^9 e^-$	0.015	0.005	~ 1.0

In conclusion, the intensity-dependent effects due to short-range wakefields are rather small in the CLIC 380 GeV BDS but not negligible. The calculated intensity-dependent parameter is around $0.39 \text{ nm}/10^9 e^-$, representing an increase on the vertical beam size at the IP of 0.47 nm when increasing the intensity from $0.52 \times 10^9 e^-$ to $5.2 \times 10^9 e^-$, 16% of the nominal vertical beam size. The intensity-dependent effects due to long-range wakefields have a significant impact on the luminosity. Indeed, at $5.2 \times 10^9 e^-$, an incoming position offset of $0.1\sigma_y$ leads to a luminosity loss of 16% and an incoming angle offset of $0.1\sigma_{y'}$ leads to a luminosity loss of 9%. However, as in the ILC, the bunch-to-bunch position and angle offsets caused by dynamics effects can be corrected with intra-train IP position and angle feedback corrections. They are applied using a stripline kicker located near the IP. It has been shown that it can recover up to 50% of the luminosity [80].

Conclusions

Summary

The next ideal large particle collider for studying the Higgs, so called Higgs factory, would be a linear electron-positron collider. The efforts have been put on two main projects, the ILC and CLIC. They are based on the same Final Focus System with a local chromatic correction in order to obtain nanometer-scale beams at the IP. In order to obtain a beam which satisfies the requirements, the impact of static and dynamic imperfections has to be taken into account. In ATF2, the test facility which studies the feasibility of the FFS, these static and dynamic imperfections coupled with the wakefield effects deteriorate the beam quality and increase the beam size at the IP.

In order to compensate for those imperfections, correction techniques are used. Considering static imperfections, the impacts of One-to-One, DFS, and WFS corrections and sextupole knobs showed that they can decrease the beam size by a factor 224 for ATF2, 7360 for the ILC 250 GeV, 5545 for the ILC 500 GeV and 147 for the CLIC 380 GeV. Those corrections are necessary in order to correct the beam size growth due to wakefields.

In ATF2, the extraction kicker injects the beam into the extraction line with incoming position and angle jitters. The incoming position jitter has a significant impact on the vertical beam size at the IP, making the ATF2 goal 1, achieving a small vertical beam size at the IP of 37 nm, hard to achieve. The impact of static and dynamic errors with wakefields were simulated in ATF2. The intensity-dependent parameter w , measuring the impact of an increase of the beam intensity on the vertical beam size at the IP, defined as $w = \sqrt{\frac{\sigma_y^{*2} - \sigma_{0y}^{*2}}{Q^2}}$, was equal to 13.78 ± 0.34 nm/ $10^9 e^-$. Measurements in ATF2 lead to an intensity-dependent parameter w of 13.76 ± 1.59 nm/ $10^9 e^-$ with a tuned machine at 174 ° mode. This shows that the wakefield effects were localised, computed and understood well in ATF2 with the tracking code developed at CERN, PLACET.

To correct the intensity-dependent effects in ATF2, a few corrections were tested. The DFS and WFS corrections lead to a decrease of w from $22.39 \pm 1.18 \text{ nm}/10^9 e^-$ to $15.04 \pm 2.02 \text{ nm}/10^9 e^-$ at 30° mode. It has to be noted that the amplitude of intensity-dependent parameter w before applying corrections depends on the conditions of the machine and varies from 20 to $28 \text{ nm}/10^9 e^-$.

The new wakefield knobs system was also tested. This comprised two wakefield sources on movers, localised at 2.5π phase advance before the IP, at a high beta region. This system decreases the intensity-dependent parameter from $27.1 \text{ nm}/10^9 e^-$ to $14.5 \text{ nm}/10^9 e^-$. DFS and WFS corrections and wakefield knobs are necessary steps in the ATF2 tuning procedure in order to achieve goal 1.

The impacts of static and dynamic imperfections coupled with wakefields were also studied in the ILC 250 GeV and 500 GeV BDS. Thanks to the One-to-One, DFS, and WFS corrections and sextupole knobs, the achieved average vertical beam size at the IP, at the nominal beam intensity of $2.0 \times 10^{10} e^-$, was 9.43 nm, close to the design value of the perfect machine in the 250 GeV, 7.7 nm. For the 500 GeV BDS, the vertical beam size at the IP was 6.06 nm, compared to 5.9 nm for the perfect machine.

The short-range wakefield effects are negligible for both 250 and 500 GeV lattices. The calculated intensity-dependent parameter was $0.04 \text{ nm}/10^9 e^-$, which represents an increase of 0.03 nm between $0.2 \times 10^{10} e^-$ and $2.0 \times 10^{10} e^-$ for the 250 GeV BDS and of 0.04 nm for the 500 GeV BDS. One-to-One, DFS, and WFS corrections and sextupole knobs are imperative corrections in order to obtain small beam sizes that satisfy the machine requirements.

However, the long-range wakefield effects are significant. Indeed, at $2.0 \times 10^{10} e^-$, the impact of incoming vertical and horizontal position offsets of $0.01\sigma_y$ and $0.01\sigma_x$, respectively, and incoming vertical and horizontal angle offsets of $0.01\sigma_{y'}$, $0.01\sigma_{x'}$, respectively leads to a luminosity loss of 64% in the 250 GeV BDS and of 41% in the 500 GeV BDS.

However, the bunch separation is large in the ILC, thus the bunch-to-bunch position and angle offsets caused by dynamics effects can be corrected with intra-train IP position and angle feedback corrections. They are applied using a stripline kicker located near the IP. This would be a crucial correction in order to have a luminosity loss smaller than 10%.

Thanks to the One-to-One, DFS, and WFS corrections and sextupole knobs, the achieved average vertical beam size in the CLIC 380 GeV stage at the IP, at the nominal beam intensity of $5.2 \times 10^9 e^-$, was 4.8 nm, close to the design value of the

perfect machine, 2.9 nm. The calculated intensity-dependent parameter was $0.39 \text{ nm}/10^9 e^-$, which represents an increase of 0.47 nm between $0.52 \times 10^9 e^-$ and $5.2 \times 10^9 e^-$, 16% of the beam size at the IP. In CLIC also, One-to-One, DFS, and WFS corrections and sextupole knobs are indispensable corrections in order to obtain small beam sizes that satisfy the machine requirements.

The long-range wakefield effects are not that significant in the CLIC 380 GeV BDS. Indeed, at $5.2 \times 10^9 e^-$, the impact of incoming vertical and horizontal position offsets of $0.01\sigma_y$ and $0.01\sigma_x$, respectively, and incoming vertical and horizontal angle offsets of $0.01\sigma_{y'}$, $0.01\sigma_{x'}$, leads to a luminosity loss of less than 0.5%.

Suggestions for further work

In order to reduce the intensity-dependent effects in ATF2, the implemented DFS and WFS could be optimised by making them automatic and part of the tuning procedure after the BPM calibration.

The ATF2 wakefield knobs could also be improved by making the 2D scan of the movers and thus the positions that lead to a minimum vertical beam size at the IP automatic. Different wakefield sources could also be employed in order to make this correction more efficient.

The measured impacts of the previously cited corrections was only done at 30° mode. It would be interesting to apply these corrections with a tuned and stable machine at 174° mode.

Due to some PLACET code limitations, the long-range wakefield studies were done with one macro-particle per bunch in the BDS. An interesting study would be look at multi-bunch and multi-particle long-range wakefield simulations from the RTML to the IP.

The final suggestion would consist of studying the impact of the wakefield knobs in CLIC and ILC.

Appendix A

Wakefield sources in ATF2

Table A.1: Positions and names of ATF2 C-BPMs.

Type	Element number	Name	Position in ATF2: s (m)
Cavity BPM	1	MQD10X	27.743
	2	MQF11X	29.193
	3	MQD12X	30.643
	4	MQD16X	34.781
	5	MQF17X	36.231
	6	MQD18X	38.614
	7	MQF19X	40.058
	8	MQD20X	43.824
	9	MQF21X	47.816
	10	MQM16FF	51.582
	11	MQM15FF	53.316
	12	MQM14FF	54.816
	13	MQM13FF	56.316
	14	MQM12FF	57.816
	15	MQM11FF	59.416
	16	MQD10AFF	61.816
	17	MQF9AFF	64.236
	18	MQD8FF	66.036
	19	MQF7FF	67.936
	20	MQF5BFF	71.636
	21	MQD4BFF	74.056
	22	MQF3FF	77.976
	23	MQD2BFF	79.676
	24	MQD2AFF	81.376

Table A.2: Positions and names of ATF2 unmasked bellows and flanges.

Type	Element number	Name	Position in ATF2: s (m)
Unmasked bellows	1	L201A	52.561
	2	L201C	53.099
	3-4	L202B1	54.599
	5	L212B	67.719
Flanges	1-5	L201A	52.561
	6-7	L201C	53.099
	8-12	L202B	54.599
	13-15	L203B	55.375
	16-17	L203C	55.397
	18-20	L204B	57.599
	21-23	L205B	58.533
	24-25	L205C	59.199
	26	L206BB	60.699
	27-29	L207B	61.395
	30-31	L207C	61.599
	32	L208B	62.107
	33	L210B	64.019
	34	L211B	64.504
	35-36	L211C	65.819
	37-39	L212B	67.719
	40	L213B	68.362
	41	L215C	71.420
	42	L216B	72.029
	43	L218B	72.981
	44	L219B	74.449
	45-47	L222	77.760
	48-50	L223B	78.403
	51	L224A	79.256
	52-53	L224B	79.460
	54-55	L225B	80.032
56-57	L225C	80.170	
58	L225E	81.160	

Appendix B

Wakefield sources in the ILC

Table B.1: Positions of ILC BDS C-BPMs.

BPM #	s (m)	BPM #	s (m)	BPM #	s (m)	BPM #	s (m)
1	0.5	27	671.2	53	1247.1	79	1731.2
2	16.0	28	674.4	54	1261.1	80	1731.7
3	31.5	29	704.3	55	1265.1	81	1733.0
4	47.0	30	760.4	56	1279.1	82	1778.8
5	58.1	31	766.7	57	1429.0	83	1805.7
6	69.1	32	769.8	58	1468.2	84	1832.6
7	80.0	33	773.0	59	1481.0	85	1878.4
8	91.1	34	779.3	60	1495.0	86	1880.2
9	106.6	35	835.4	61	1509.0	87	1880.7
10	122.1	36	865.3	62	1510.7	88	1882.0
11	137.6	37	868.5	63	1537.9	89	1892.2
12	157.3	38	871.6	64	1565.1	90	1894.1
13	160.6	39	901.5	65	1566.7	91	1895.9
14	172.8	40	957.6	66	1580.7	92	1896.4
15	190.0	41	963.9	67	1594.7	93	1897.7
16	191.0	42	967.1	68	1607.9	94	2034.8
17	207.2	43	970.2	69	1614.9	95	2061.7
18	224.4	44	976.5	70	1654.4	96	2088.6
19	225.4	45	1013.8	71	1659.4	97	2242.8
20	241.6	46	1054.0	72	1697.6	98	2243.3
21	258.8	47	1058.0	73	1713.7	99	2243.4
22	259.8	48	1097.2	74	1715.5	100	2244.7
23	323.0	49	1135.4	75	1717.3	101	2247.4
24	326.5	50	1160.0	76	1719.2	102	2247.7
25	367.2	51	1184.6	77	1719.2	103	2247.7
26	466.5	52	1209.2	78	1729.4	104	2248.9

Appendix C

Wakefield sources in CLIC

Table C.1: Positions of CLIC 380 GeV BDS C-BPMs.

#	s (m)	#	s (m)	#	s (m)	#	s (m)	#	s (m)
1	0.0	28	158.9	55	868.4	82	971.4	109	1131.2
2	5.5	29	159.4	56	868.9	83	979.8	110	1131.7
3	11.0	30	178.1	57	869.5	84	980.3	111	1140.1
4	16.5	31	178.6	58	870.0	85	998.4	112	1147.0
5	17.0	32	197.2	59	870.6	86	998.9	113	1159.5
6	26.4	33	202.0	60	871.1	87	999.8	114	1172.0
7	36.3	34	205.0	61	871.8	88	1000.3	115	1184.3
8	36.8	35	211.0	62	872.3	89	1018.4	116	1193.0
9	40.3	36	212.3	63	884.4	90	1018.9	117	1205.9
10	40.8	37	363.5	64	884.9	91	1027.3	118	1218.8
11	44.4	38	364.8	65	885.5	92	1027.8	119	1231.2
12	44.9	39	376.0	66	886.0	93	1036.2	120	1246.8
13	48.5	40	377.3	67	886.9	94	1036.7	121	1279.9
14	49.0	41	528.5	68	887.4	95	1054.8	122	1333.9
15	52.5	42	529.8	69	905.5	96	1055.3	123	1337.1
16	53.0	43	541.0	70	906.0	97	1056.2	124	1391.0
17	62.4	44	542.3	71	914.4	98	1056.7	125	1394.2
18	62.9	45	693.5	72	914.9	99	1074.8	126	1460.6
19	72.3	46	694.8	73	923.3	100	1075.3	127	1463.8
20	72.8	47	706.0	74	923.8	101	1083.7	128	1483.6
21	82.2	48	707.3	75	941.9	102	1084.2	129	1488.6
22	101.3	49	858.5	76	942.4	103	1092.6	130	1658.2
23	101.8	50	859.8	77	943.4	104	1093.1	131	1687.4
24	120.5	51	866.1	78	943.9	105	1111.2	132	1716.7
25	121.0	52	866.6	79	961.9	106	1111.7	133	1925.7
26	139.7	53	867.3	80	962.4	107	1112.6	134	1938.4
27	140.2	54	867.8	81	970.9	108	1113.1		

Bibliography

- [1] I. GDE, “What is the Linear Collider Collaboration?” 2013. [Online]. Available: <http://linearcollider.org/about> (Cited on pages v and 6.)
- [2] CERN, “Accelerator Overview.” [Online]. Available: <https://clic.cern/accelerator-overview> (Cited on pages v and 7.)
- [3] ATF2, “ATF2.” [Online]. Available: <https://ilc.kek.jp/ATF2/> (Cited on pages v and 13.)
- [4] J. Yan, Y. Yamaguchi, Y. Kamiya *et al.*, “Measurement of nanometer electron beam sizes with laser interference using Shintake Monitor,” *Nuclear Instruments and Methods in Physics Research, Section A: Accelerators, Spectrometers, Detectors and Associated Equipment*, 2014. [Online]. Available: <https://www.sciencedirect.com/science/article/pii/S0168900213015805> (Cited on pages v, 16 and 17.)
- [5] M. Herrero, “The Standard Model,” in *Techniques and Concepts of High Energy Physics X*, T. Ferbel, Ed. Dordrecht: Springer Netherlands, 1999, pp. 1–59. [Online]. Available: https://doi.org/10.1007/978-94-011-4689-0_1http://link.springer.com/10.1007/978-94-011-4689-0_1 (Cited on page 1.)
- [6] D. H. Perkins, *Introduction to High Energy Physics*. Cambridge University Press, 4 2000. [Online]. Available: <https://www.cambridge.org/core/product/identifier/9780511809040/type/book> (Cited on page 1.)
- [7] D. Griffiths, *Introduction to Elementary Particles*. Wiley, 12 1987. [Online]. Available: <https://onlinelibrary.wiley.com/doi/book/10.1002/9783527618460> (Cited on page 1.)
- [8] R. J. Blin-Stoyle, *Nuclear and Particle Physics*. Dordrecht: Springer Netherlands, 1991. [Online]. Available: <http://link.springer.com/10.1007/978-94-010-9561-7> (Cited on page 1.)

- [9] P. W. Higgs, “Broken symmetries and the masses of gauge bosons,” *Physical Review Letters*, vol. 13, no. 16, pp. 508–509, 10 1964. [Online]. Available: <https://link.aps.org/doi/10.1103/PhysRevLett.13.508> (Cited on page 1.)
- [10] The CMS Collaboration, “Observation of a new boson at a mass of 125 GeV with the CMS experiment at the LHC,” *Physics Letters, Section B: Nuclear, Elementary Particle and High-Energy Physics*, vol. 716, no. 1, pp. 30–61, 7 2012. [Online]. Available: <http://arxiv.org/abs/1207.7235><http://dx.doi.org/10.1016/j.physletb.2012.08.021> (Cited on page 1.)
- [11] The ATLAS Collaboration, “Observation of a new particle in the search for the Standard Model Higgs boson with the ATLAS detector at the LHC,” *Physics Letters, Section B: Nuclear, Elementary Particle and High-Energy Physics*, vol. 716, no. 1, pp. 1–29, 7 2012. [Online]. Available: <http://arxiv.org/abs/1207.7214><http://dx.doi.org/10.1016/j.physletb.2012.08.020> (Cited on page 1.)
- [12] J. D. Cockcroft and E. T. S. Walton, “Experiments with high velocity positive ions.(I) Further developments in the method of obtaining high velocity positive ions,” *Proceedings of the Royal Society of London. Series A, Containing Papers of a Mathematical and Physical Character*, vol. 136, no. 830, pp. 619–630, 6 1932. [Online]. Available: <https://royalsocietypublishing.org/doi/10.1098/rspa.1932.0107> (Cited on page 2.)
- [13] K. Aamodt, N. Abel, U. Abeysekara *et al.*, “First proton-proton collisions at the LHC as observed with the ALICE detector: measurement of the charged-particle pseudorapidity density at $\sqrt{s} = 900$ GeV,” *The European Physical Journal C*, vol. 65, no. 1-2, pp. 111–125, 1 2010. [Online]. Available: <http://arxiv.org/abs/0911.5430><http://link.springer.com/10.1140/epjc/s10052-009-1227-4> (Cited on page 2.)
- [14] ATLAS Collaboration, “Electron and photon energy calibration with the ATLAS detector using 2015-2016 LHC proton-proton collision data,” *Journal of Instrumentation*, vol. 14, no. 3, pp. P03017–P03017, 12 2018. [Online]. Available: <http://arxiv.org/abs/1812.03848><http://dx.doi.org/10.1088/1748-0221/14/03/P03017> (Cited on page 2.)
- [15] P. D. Johnson, “Synchrotron Radiation,” in *Experimental Methods in the Physical Sciences*. Academic Press, 1997, vol. 29, pp. 23–43. [Online]. Available: <https://linkinghub.elsevier.com/retrieve/pii/S0076695X08606110> (Cited on page 3.)

- [16] M. Tanabashi, K. Hagiwara, K. Hikasa *et al.*, “Review of Particle Physics,” *Physical Review D*, vol. 98, no. 3, p. 030001, 8 2018. [Online]. Available: <https://link.aps.org/doi/10.1103/PhysRevD.98.030001> (Cited on page 3.)
- [17] W. Kilian, M. Krämer, and P. Zerwas, “Higgs-strahlung and WW fusion in e+e collisions,” *Physics Letters B*, vol. 373, no. 1-3, pp. 135–140, 4 1996. [Online]. Available: <https://linkinghub.elsevier.com/retrieve/pii/0370269396001001> (Cited on page 4.)
- [18] C. Adolphsen, M. Barone, B. Barish *et al.*, “The International Linear Collider Technical Design Report - Baseline Design,” *arXiv:1306.6353 [physics]*, vol. 3, 2013. [Online]. Available: <http://arxiv.org/abs/1306.6353> (Cited on pages 4, 77 and 90.)
- [19] P. Raimondi and A. Seryi, “Novel Final Focus Design for Future Linear Colliders,” *Physical Review Letters*, vol. 86, no. 17, pp. 3779–3782, 4 2001. [Online]. Available: <https://link.aps.org/doi/10.1103/PhysRevLett.86.3779> (Cited on pages 5 and 14.)
- [20] H. Zha and A. Grudiev, “Design and optimization of Compact Linear Collider main linac accelerating structure,” *Physical Review Accelerators and Beams*, vol. 19, no. 11, p. 111003, 11 2016. [Online]. Available: <https://link.aps.org/doi/10.1103/PhysRevAccelBeams.19.111003> (Cited on pages 5 and 52.)
- [21] F. Tecker, R. Corsini, S. Döbert *et al.*, “CTF3 combiner ring commissioning,” in *2007 IEEE Particle Accelerator Conference (PAC)*. IEEE, 6 2007, pp. 2850–2852. [Online]. Available: <https://ieeexplore.ieee.org/document/4440597/> (Cited on page 5.)
- [22] R. Corsini, S. Döbert, F. Tecker *et al.*, “Commissioning status of the CTF3 delay loop,” in *EPAC 2006 - Contributions to the Proceedings*, 2006, pp. 771–773. [Online]. Available: <http://cds.cern.ch/record/971857/files/ab-2006-041.pdf> (Cited on page 5.)
- [23] M. Aicheler, P. N. Burrows, N. Catalan *et al.*, “The Compact Linear Collider (CLIC) - Project Implementation Plan,” CERN, Tech. Rep., 3 2019. [Online]. Available: <http://arxiv.org/abs/1903.08655><http://arxiv.org/abs/1903.08655><http://dx.doi.org/10.23731/CYRM-2018-004> (Cited on pages 5 and 111.)

- [24] J. Rossbach and P. Schmüser, “Basic course on accelerator optics,” 1993. [Online]. Available: <https://cds.cern.ch/record/247501/files/p17.pdf> (Cited on page 9.)
- [25] F. Hinode, S. . Kawabata, H. Matsumoto *et al.*, “ATF Accelerator Test Facility : design and study report,” KEK, Tech. Rep., 1995. [Online]. Available: <https://ilc.kek.jp/ATF/Pub/KEK-I-95-4.pdf> (Cited on page 11.)
- [26] K. Kubo, M. Akemoto, S. Anderson *et al.*, “Extremely Low Vertical-Emittance Beam in the Accelerator Test Facility at KEK,” *Physical Review Letters*, vol. 88, no. 19, p. 194801, 4 2002. [Online]. Available: <https://link.aps.org/doi/10.1103/PhysRevLett.88.194801> (Cited on page 11.)
- [27] Y. Honda, K. Kubo, S. Anderson *et al.*, “Achievement of Ultralow Emittance Beam in the Accelerator Test Facility Damping Ring,” *Physical Review Letters*, vol. 92, no. 5, p. 054802, 2 2004. [Online]. Available: <https://link.aps.org/doi/10.1103/PhysRevLett.92.054802> (Cited on pages 11 and 53.)
- [28] B. I. Grishanov, P. Logachev, F. Podgorny *et al.*, “ATF2 Proposal, Vol. 2,” KEK, Tech. Rep., 2005. [Online]. Available: <https://arxiv.org/pdf/physics/0606194.pdf> (Cited on page 11.)
- [29] M. Bergamaschi, A. Aryshev, P. Karataev *et al.*, “Noninvasive Micrometer-Scale Particle-Beam Size Measurement Using Optical Diffraction Radiation in the Ultraviolet Wavelength Range,” *Physical Review Applied*, 2020. [Online]. Available: <https://journals.aps.org/prapplied/pdf/10.1103/PhysRevApplied.13.014041> (Cited on page 11.)
- [30] M. Patecki, “Optimisation analysis and improvement of the effective beam sizes in Accelerator Test Facility 2,” Ph.D. dissertation, Warsaw University of Technology, 2016. [Online]. Available: https://cds.cern.ch/record/2265996/files/CERN-THESIS-2016-304_2.pdf (Cited on page 11.)
- [31] A. Collaboration, “Aiming for nanobeams.” [Online]. Available: <http://www-atf.kek.jp/atf/files/ATF-E1227.pdf> (Cited on page 11.)
- [32] J. Urakawa, “ATF results and ATF-II plans,” in *2007 IEEE Particle Accelerator Conference (PAC)*. IEEE, 2007, pp. 1950–1954. [Online]. Available: <http://ieeexplore.ieee.org/document/4441318/> (Cited on page 11.)

- [33] A. Faus-Golfe, J. Alabau-Gonzalvo, C. Gutierrez *et al.*, “Upgrade and systematic measurement campaign of the ATF2 multi-OTR system,” in *IPAC 2013: Proceedings of the 4th International Particle Accelerator Conference*, 2013. [Online]. Available: <https://accelconf.web.cern.ch/IPAC2013/papers/mopwo023.pdf> (Cited on page 12.)
- [34] T. Okugi, “Achievement of small beam size at ATF2 beamline,” *Proceedings of LINAC 2016*, 2016. [Online]. Available: <https://accelconf.web.cern.ch/linac2016/papers/mo3a02.pdf> (Cited on page 14.)
- [35] T. Shintake, “Proposal of a nanometer beam size monitor for e+e linear colliders,” *Nuclear Instruments and Methods in Physics Research Section A: Accelerators, Spectrometers, Detectors and Associated Equipment*, vol. 311, no. 3, pp. 453–464, 1 1992. [Online]. Available: <https://linkinghub.elsevier.com/retrieve/pii/016890029290641G> (Cited on page 16.)
- [36] V. Balakin, V. A. Alexandrov, A. Mikhailichenko *et al.*, “Focusing of Submicron Beams for TeV-Scale e+e Linear Colliders,” *Physical Review Letters*, vol. 74, no. 13, pp. 2479–2482, 3 1995. [Online]. Available: <https://link.aps.org/doi/10.1103/PhysRevLett.74.2479> (Cited on page 16.)
- [37] Y. Yamaguchi, S. Komamiya, M. Orouku *et al.*, “Evaluation of expected performance of Shintake beam size monitor for ATF2,” in *IPAC 2010: Proceedings of the 1st International Particle Accelerator Conference*, Kyoto, Japan, 2010, pp. 1014–1016. [Online]. Available: <https://accelconf.web.cern.ch/accelconf/IPAC10/papers/mope023.pdf> (Cited on page 16.)
- [38] J. Yan, M. Orouku, Y. Yamaguchi *et al.*, “Shintake Monitor Nanometer Beam Size Measurement and Beam Tuning,” *Physics Procedia*, vol. 37, pp. 1989–1996, 2012. [Online]. Available: <https://linkinghub.elsevier.com/retrieve/pii/S1875389212019177> (Cited on pages 16 and 69.)
- [39] P. Forck, P. Kowina, and D. Liakin, “Beam position monitors,” GSI, Tech. Rep., 2008. [Online]. Available: <https://cas.web.cern.ch/sites/cas.web.cern.ch/files/lectures/dourdan-2008/forck-part2.pdf> (Cited on pages 18 and 19.)
- [40] R. Apsimon, D. Bett, P. Burrows *et al.*, “The FONT5 Bunch-by-Bunch Position and Angle Feedback System at ATF2,” *Physics Procedia*, vol. 37, pp. 2063–2071, 2012. [Online]. Available: <https://linkinghub.elsevier.com/retrieve/pii/S1875389212019244> (Cited on page 20.)

- [41] R. J. Apsimon, D. R. Bett, N. Blaskovic Kraljevic *et al.*, “Design and performance of a high resolution, low latency stripline beam position monitor system,” *Physical Review Special Topics - Accelerators and Beams*, vol. 18, no. 3, p. 032803, 3 2015. [Online]. Available: <https://link.aps.org/doi/10.1103/PhysRevSTAB.18.032803> (Cited on page 20.)
- [42] N. B. Kraljevic, D. Bett, R. Bodenstein *et al.*, “Optimisation of a High-Resolution, Low-Latency Stripline Beam Position Monitor System for Use in Intra-Train Feedback,” in *IPAC 2017: Proceedings of the 8th International Particle Accelerator Conference*, 2017. [Online]. Available: <https://cds.cern.ch/record/2289157/files/tupik110.pdf> (Cited on pages 20 and 57.)
- [43] R. J. Apsimon, D. R. Bett, N. Blaskovic Kraljevic *et al.*, “Design and operation of a prototype interaction point beam collision feedback system for the International Linear Collider,” *Physical Review Accelerators and Beams*, vol. 21, no. 12, p. 122802, 12 2018. [Online]. Available: <https://link.aps.org/doi/10.1103/PhysRevAccelBeams.21.122802> (Cited on pages 20 and 100.)
- [44] T. Bromwich, S. Araki, A. Aryshev *et al.*, “Performance of Nanometre-Level Resolution Cavity Beam Position Monitors at ATF2,” in *IPAC 2018: Proceedings of the 9th International Particle Accelerator Conference*, 2018. [Online]. Available: <https://accelconf.web.cern.ch/ipac2018/papers/tuzgbd5.pdf> (Cited on page 20.)
- [45] P. B. Wilson, “Introduction to wakefields and wake potentials,” in *AIP Conference Proceedings*, vol. 184. AIP, 1989, pp. 525–564. [Online]. Available: <http://aip.scitation.org/doi/abs/10.1063/1.38045> (Cited on page 22.)
- [46] W. Bruns, “GdfidL: a finite difference program with reduced memory and CPU usage,” in *Proceedings of the 1997 Particle Accelerator Conference (Cat. No.97CH36167)*, vol. 2. IEEE, 1998, pp. 2651–2653. [Online]. Available: <http://ieeexplore.ieee.org/document/751304/> (Cited on pages 22 and 26.)
- [47] G. R. White, R. Ainsworth, T. Akagi *et al.*, “Experimental Validation of a Novel Compact Focusing Scheme for Future Energy-Frontier Linear Lepton Colliders,” *Physical Review Letters*, vol. 112, no. 3, p. 034802, 1 2014. [Online]. Available: <https://link.aps.org/doi/10.1103/PhysRevLett.112.034802> (Cited on page 26.)

- [48] A. Latina, E. Adli, H. Burkhardt *et al.*, “Recent improvements in the tracking code placet,” *EPAC 2008 - Contributions to the Proceedings*, pp. 1750–1752, 2008. [Online]. Available: <https://accelconf.web.cern.ch/e08/papers/tupp094.pdf> (Cited on page 26.)
- [49] J. Snuverink, R. Ainsworth, S. T. Boogert *et al.*, “Measurements and simulations of wakefields at the Accelerator Test Facility 2,” *Physical Review Accelerators and Beams*, vol. 19, no. 9, p. 091002, 9 2016. [Online]. Available: <https://link.aps.org/doi/10.1103/PhysRevAccelBeams.19.091002> (Cited on page 26.)
- [50] M. G. Minty and F. Zimmermann, “Correction to: Measurement and Control of Charged Particle Beams,” in *Correction to: Measurement and Control of Charged Particle Beams*. Springer, 2019, pp. C1–C1. [Online]. Available: http://link.springer.com/10.1007/978-3-662-08581-3_13 (Cited on page 32.)
- [51] T. Raubenheimer and R. Ruth, “A dispersion-free trajectory correction technique for linear colliders,” *Nuclear Instruments and Methods in Physics Research Section A: Accelerators, Spectrometers, Detectors and Associated Equipment*, vol. 302, no. 2, pp. 191–208, 4 1991. [Online]. Available: <https://linkinghub.elsevier.com/retrieve/pii/016890029190403D> (Cited on page 33.)
- [52] T. Raubenheimer, “A new technique of correcting emittance dilutions in linear colliders,” *Nuclear Instruments and Methods in Physics Research Section A: Accelerators, Spectrometers, Detectors and Associated Equipment*, vol. 306, no. 1-2, pp. 61–64, 8 1991. [Online]. Available: <https://linkinghub.elsevier.com/retrieve/pii/0168900291903027> (Cited on page 33.)
- [53] Y. Nosochkov, P. Raimondi, T. Raubenheimer *et al.*, “Tuning knobs for the NLC final focus,” in *Proceedings of EPAC 2002*, 2002. [Online]. Available: <http://accelconf.web.cern.ch/e02/PAPERS/MOPRI047.pdf> (Cited on page 34.)
- [54] F. Plassard, “Optics optimization of longer L* Beam Delivery System designs for CLIC and tuning of the ATF2 final focus system at ultra-low β^* using octupoles,” Ph.D. dissertation, Université Paris-Sud, 2018. [Online]. Available: <https://cds.cern.ch/record/2646086/files/CERN-THESIS-2018-223.pdf> (Cited on page 34.)
- [55] T. Okugi, S. Araki, P. Bambade *et al.*, “Linear and second order optics corrections for the KEK Accelerator Test Facility final focus beam line,” *Physical*

- Review Special Topics - Accelerators and Beams*, vol. 17, no. 2, p. 023501, 2 2014. [Online]. Available: <https://link.aps.org/doi/10.1103/PhysRevSTAB.17.023501> (Cited on page 34.)
- [56] B. I. Grishanov, P. Logachev, F. Podgorny *et al.*, “ATF2 Proposal,” Stanford Linear Accelerator Center (SLAC), Menlo Park, CA, Tech. Rep., 8 2005. [Online]. Available: <http://www.osti.gov/servlets/purl/878752-ENcHlD/> (Cited on page 39.)
- [57] K. Bane, T. Naito, T. Okugi *et al.*, “Impedance analysis of bunch length measurements at the ATF damping ring,” *International Journal of Applied Electromagnetics and Mechanics*, vol. 14, no. 1-4, pp. 197–202, 12 2002. [Online]. Available: <https://www.medra.org/servlet/aliasResolver?alias=iospress&doi=10.3233/JAE-2002-389> (Cited on page 52.)
- [58] K. Kubo and K. Oide, “Intrabeam scattering in electron storage rings,” *Physical Review Special Topics - Accelerators and Beams*, vol. 4, no. 12, pp. 78–84, 12 2001. [Online]. Available: <https://link.aps.org/doi/10.1103/PhysRevSTAB.4.124401> (Cited on page 53.)
- [59] D. R. Bett, P. N. Burrows, C. Perry *et al.*, “Design, operation and performance of a sub-microsecond latency intra-bunch-train dual-phase beam-orbit feedback system,” *Manuscript submitted for publication*, 2020. (Cited on page 57.)
- [60] J. Irwin, C. X. Wang, Y. T. Yan *et al.*, “Model-Independent Beam Dynamics Analysis,” *Physical Review Letters*, vol. 82, no. 8, pp. 1684–1687, 2 1999. [Online]. Available: <https://link.aps.org/doi/10.1103/PhysRevLett.82.1684> (Cited on pages 59, 60 and 62.)
- [61] Y. I. Kim, R. Ainsworth, A. Aryshev *et al.*, “Cavity beam position monitor system for the Accelerator Test Facility 2,” *Physical Review Special Topics - Accelerators and Beams*, vol. 15, no. 4, p. 042801, 4 2012. [Online]. Available: <https://link.aps.org/doi/10.1103/PhysRevSTAB.15.042801> (Cited on page 60.)
- [62] E. Isaacson, “Numerical Recipes in C: The Art of Scientific Computing (William H. Press, Brian P. Flannery, Saul A. Teukolsky, and William T. Vetterling); Numerical Recipes: Example Book (C) (William T. Vetterling, Saul A. Teukolsky, William H. Press, and Brian P. Flannery),” *SIAM Review*, vol. 31, no. 1, pp. 142–142, 3 1989. [Online]. Available: <http://epubs.siam.org/doi/10.1137/1031025> (Cited on page 62.)

- [63] R. Bodenstein, “A Procedure for Beamline Characterization and Tuning in Open-Ended Beamlines,” Ph.D. dissertation, University of Virginia, Charlottesville, VA, 12 2012. [Online]. Available: https://casa.jlab.org/publications/CASA_PhDs/Bodenstein_Dissertation.pdfhttps://libraetd.lib.virginia.edu/public_view/5425k992v (Cited on page 62.)
- [64] G. White, “ILC Lattices,” 2016. [Online]. Available: <https://bitbucket.org/whitegr/ilc-lattices/src/master/> (Cited on page 77.)
- [65] T. Okugi, “Simulation of Intensity dependence for ILC250 IP beam size,” KEK, LCWS2018 , Arlington, Tech. Rep., 2018. [Online]. Available: https://agenda.linearcollider.org/event/7889/contributions/42474/attachments/33752/51792/ILCBDS_okugi_20181023.pdf (Cited on page 79.)
- [66] A. W. Chao and M. Tigner, *Handbook of Accelerator Physics and Engineering*. WORLD SCIENTIFIC, 3 1999. [Online]. Available: <https://www.worldscientific.com/worldscibooks/10.1142/3818> (Cited on page 82.)
- [67] R. Mutzner, G. Rumolo, T. Pieloni *et al.*, “Multi-Bunch effect of resistive wall in the beam delivery system of the Compact Linear Collider,” Ph.D. dissertation, EPFL, 2010. [Online]. Available: <http://cdsweb.cern.ch/record/1266868/files/CERN-THESIS-2010-073.pdf> (Cited on page 82.)
- [68] R. Apsimon, A. Latina, D. Schulte *et al.*, “Design of the clic pre-main linac collimation system,” in *IPAC 2013: Proceedings of the 4th International Particle Accelerator Conference*, 2013. [Online]. Available: <https://accelconf.web.cern.ch/IPAC2013/papers/mopwo024.pdf> (Cited on page 84.)
- [69] R. Apsimon, A. Latina, D. Schulte *et al.*, “Feed forward orbit correction in the CLIC ring to main LINAC transfer lines,” in *IPAC 2014: Proceedings of the 5th International Particle Accelerator Conference*, 2014. [Online]. Available: <https://accelconf.web.cern.ch/IPAC2014/papers/mopro029.pdf> (Cited on page 84.)
- [70] K. Kubo, “ILC Beam Dynamics - Main Linac and Bunch Compressor,” KEK, Tech. Rep., 2006. [Online]. Available: http://accwww2.kek.jp/oho/oho06/OHO06_Kubo_lecture.pdf (Cited on page 87.)

- [71] D. Schulte, “Multi-Bunch calculations in the CLIC Main LINAC,” CERN, Tech. Rep., 2009. [Online]. Available: <https://cds.cern.ch/record/1227215> (Cited on pages 87 and 98.)
- [72] D. Schulte, “Study of Electromagnetic and Hadronic Background in the Interaction Region of the TESLA Collider,” Ph.D. dissertation, Universität Hamburg, 1996. [Online]. Available: https://flash.desy.de/sites2009/site_vuvfel/content/e403/e1644/e1314/e1316/infoboxContent1932/tesla1997-08.pdf (Cited on page 89.)
- [73] J. Resta-López, P. N. Burrows, T. Hartin *et al.*, “Placet based start-to-end simulations of the ILC with intra-train fast feedback system,” in *EPAC 2008 - Contributions to the Proceedings*, 2008, pp. 604–606. [Online]. Available: <https://accelconf.web.cern.ch/e08/papers/mopp027.pdf> (Cited on page 100.)
- [74] H. Schmickler, L. Soby, A. Lunin *et al.*, “Submicron multi-bunch BPM for CLIC,” in *IPAC 2010: Proceedings of the 1st International Particle Accelerator Conference*, 2010, pp. 1185–1187. [Online]. Available: <https://accelconf.web.cern.ch/IPAC10/papers/mope087.pdf> (Cited on page 102.)
- [75] E. Marin, A. Latina, R. Tomás *et al.*, “Final focus system tuning studies towards Compact Linear Collider feasibility,” *Physical Review Accelerators and Beams*, vol. 21, no. 1, p. 011003, 1 2018. [Online]. Available: <https://link.aps.org/doi/10.1103/PhysRevAccelBeams.21.011003> (Cited on page 103.)
- [76] “Private communications with Andrea Latina.” (Cited on pages 103 and 108.)
- [77] J. Ögren, A. Latina, R. Tomás *et al.*, “Tuning of the CLIC 380 GeV Final-Focus System with Static Imperfections,” CERN, Tech. Rep. CLIC-Note-1141, 2018. [Online]. Available: <https://cds.cern.ch/record/2651111/files/CERN-ACC-2018-0055.pdf> (Cited on page 103.)
- [78] D. Arominski, “Beam-induced Backgrounds at the Compact Linear Collider,” Ph.D. dissertation, Warsaw University of Technology, 2020. (Cited on page 107.)
- [79] J. Resta-López, P. N. Burrows, and G. Christian, “Luminosity performance studies of the compact linear collider with intra-train feedback system at the interaction point,” *Journal of Instrumentation*, vol. 5, no. 09, pp. P09007–P09007, 9 2010. [Online]. Available: <https://iopscience.iop.org/article/10.1088/1748-0221/5/09/P09007> (Cited on page 112.)

-
- [80] J. Resta-López and P. N. Burrows, “The beam-based intra-train feedback system of CLIC,” in *IPAC 2010: Proceedings of the 1st International Particle Accelerator Conference*, 2010, pp. 2791–2793. [Online]. Available: <https://accelconf.web.cern.ch/IPAC10/papers/wepeb045.pdf> (Cited on pages 112 and 113.)